Information

46

Growth and characterization of crystalline thin oxide fims

Anna Barbara Schäfer

Member of the Helmholtz Association

Information
Band / Volume 46
ISBN 978-3-95806-111-8

JÜLICH
FORSCHUNGSZENTRUM

Growth and characterization of crystalline rare-earth based thin oxide films for the application as gate dielectric in nanotechnology

Anna Barbara Schäfer

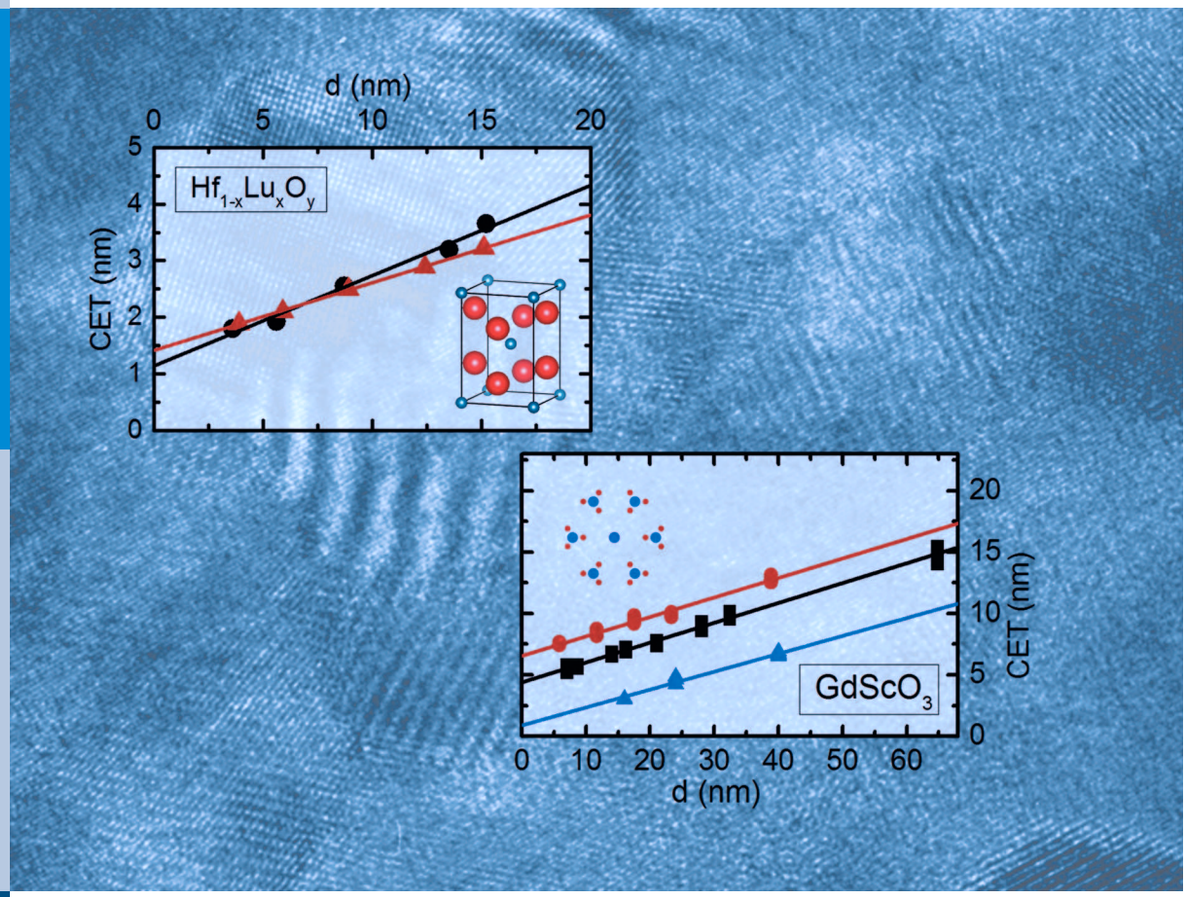

Information
Band / Volume 46
ISBN 978-3-95806-111-8

JÜLICH
FORSCHUNGSZENTRUM

Schriften des Forschungszentrums Jülich
Reihe Information / Information Band / Volume 46

Forschungszentrum Jülich GmbH
Peter Grünberg Institute
Semiconductor Nanoelectronics (PGI-9)

Growth and characterization of crystalline rare-earth based thin oxide films for the application as gate dielectric in nanotechnology

Anna Barbara Schäfer

Schriften des Forschungszentrums Jülich
Reihe Information / Information — Band / Volume 46

ISSN 1866-1777 — ISBN 978-3-95806-111-8

Bibliographic information published by the Deutsche Nationalbibliothek.
The Deutsche Nationalbibliothek lists this publication in the Deutsche
Nationalbibliografie; detailed bibliographic data are available in the
Internet at http://dnb.d-nb.de.

Publisher and Distributor: Forschungszentrum Jülich GmbH
Zentralbibliothek
52425 Jülich
Tel: +49 2461 61-5368
Fax: +49 2461 61-6103
Email: zb-publikation@fz-juelich.de
www.fz-juelich.de/zb

Cover Design: Grafische Medien, Forschungszentrum Jülich GmbH

Printer: Grafische Medien, Forschungszentrum Jülich GmbH

Schriften des Forschungszentrums Jülich
Reihe Information / Information, Band / Volume 46

D 82 (Diss. RWTH Aachen University, 2015)

ISSN 1866-1777
ISBN 978-3-95806-111-8

The complete volume is freely available on the Internet on the Jülicher Open Access Server (JuSER)
at www.fz-juelich.de/zb/openaccess.

Abstract

For standard metal oxides semiconductor (MOS) field effect transistors (FETs), but also for any other MOS based device appropriate gate dielectrics are needed. Such dielectrics, usually oxides, need to exhibit good layer quality and stability, good insulating properties and typically high permittivities. The aim of this work is to develop new oxides for the use in standard Si transistors on the one hand and for GaN based devices such as high electron mobility transistors on the other hand.

For Si MOSFETs a standard atomic layer deposition (ALD) HfO_2 process is extended to dope HfO_2 with Al and Lu. After process optimization $Hf_{0.89}Al_{0.11}O_{2-\Delta}$ and $Hf_{0.8}Lu_{0.2}O_{2-\Delta}$ transform into a polycrystalline layer with large fractions of a high κ phase of HfO_2, most probably the cubic one, and exhibit permittivities of 30 and 33, respectively.

All layers are smooth, the density of interface traps hardly changes due to doping and leakage current densities for $Hf_{0.8}Lu_{0.2}O_{2-\Delta}$ are as low as $10^{-8}\,A/cm^2$ for an equivalent oxide thickness of 1.5 nm.

For the application on GaN, crystalline $GdScO_3$ and $LaLuO_3$ are investigated. Calculations on $GdScO_3$ reveal that the orthorhombic and cubic form of $GdScO_3$ have almost equal energies of formation while a hexagonal crystal has a 500 eV per formula unit enhanced energy.

Even though the energy of formation is fairly high, the novel hexagonal forms of $GdScO_3$ and $LaLuO_3$ could be stabilized by pulsed laser deposition on GaN and on Y_2O_3 on Si (111) which is used as alternative growth template with hexagonal geometry. Thus the nature of the substrate (polar/ non-polar) apparently determines the structure of the oxide formed. Further analysis shows that the two growth templates can promote the hexagonal or the cubic forms of $GdScO_3$ and $LaLuO_3$ depending on growth temperature and Y_2O_3 layer thickness.

Relative permittivities of approximately 26 are extracted for both hexagonal $GdScO_3$ and hexagonal $LaLuO_3$. All known phases of the two oxides have band gaps above 5 eV which is important for the use as gate dielectric, e.g. to minimize tunneling currents. Current voltage measurements reveal leakage current densities of $1.2 \times 10^{-8}\,Acm^{-2}$ at 1 V for $EOT = 3\,nm$ and a dielectric breakdown above $2\,MVcm^{-1}$ for hexagonal $GdScO_3$ on GaN.

Kurzfassung

Für Metall-Oxid-Halbleiter (MOS) Feldeffekt-Transistoren (FETs), aber auch für diverse andere MOS-basierte Bauteile werden geeignete Gatedielektrika benötigt. Solche Dielektrika, üblicherweise Oxide, müssen eine hohe Schichtqualität, gute Isolationseigenschaften und typischerweise hohe dielektrische Permittivitäten κ aufweisen. Das Ziel dieser Arbeit ist die Entwicklung neuer Oxide für den Einsatz in Silizium basierten Transistoren auf der einen Seite und für Galliumnitrid (GaN) basierte Bauteile, wie z.B. Transistoren mit hoher Elektronenbeweglichkeit (HEMTs), auf der anderen Seite.

Für Si MOSFETs wird ein typischer Prozess der Atomlagenabscheidung (ALD) zur Abscheidung von Hafniumdioxid erweitert, um HfO_2 mit Al oder Lu zu dotieren und somit κ zu erhöhen. Nach einer Optimierung des Depositionsprozesses weisen $Hf_{0,89}Al_{0,11}O_{2-\Delta}$ und $Hf_{0,8}Lu_{0,2}O_{2-\Delta}$ große Anteile einer Phase von HfO_2 mit hohem κ auf, höchstwahrscheinlich der kubischen Struktur, und zeigen relative Permittivitäten von jeweils 30 und 33 auf.

Alle Oxidschichten sind glatt, die Dichte der Grenzschichtdefekte D_{it} ändert sich kaum durch die Dotierung und die Leckstromdichten für $Hf_{0,8}Lu_{0,2}O_{2-\Delta}$ sind bis zu $10^{-8}\,A/cm^2$ klein für eine äquivalente Oxidschichtdicke (EOT) von 1,5 nm.

Für die Anwendung auf GaN werden kristallines $GdScO_3$ und $LaLuO_3$ untersucht. Berechnungen zu $GdScO_3$ zeigen, dass die Formierungsenergien von orthorhombischem und kubischem $GdScO_3$ nahezu identisch sind, während hexagonales $GdScO_3$ eine um ca. 500 eV erhöhte Formierungsenergie hat.

Trotz der hohen Bildungsenergie können die neuen hexagonalen Formen von $GdScO_3$ und $LaLuO_3$ mittels Laserstrahlverdampfens abgeschieden werden. Als Substrate dienen hierbei GaN und $Y_2O_3/Si\,(111)$, das als alternatives Substrat mit hexagonaler Geometrie entlang der Oberfläche genutzt wird. Somit ist offensichtlich die Beschaffenheit des Substrats, wie z.B. die Polarität des Galliumnitrids, entscheidend für die Kristallstruktur, die sich bildet. Weitere Untersuchungen zeigen, dass $GdScO_3$ und $LaLuO_3$ je nach Temperatur während des Wachstums und je nach Schichtdicke des Yttriumoxids in hexagonaler und in kubischer Form abgeschieden werden können.

Sowohl für hexagonales $GdScO_3$ als auch für hexagonales $LaLuO_3$ werden relative Permittivitäten von 26 ermittelt. Alle Modifikationen von $GdScO_3$ und $LaLuO_3$ haben Bandlücken von über 5 eV. Dies ist wichtig für den Einsatz als Gatedielektrikum, um z.B. Tunnelströme zu minimieren. Für hexagonales $GdScO_3$ werden Leckstromdichten von $1.2\times10^{-8}\,Acm^{-2}$ bei 1 V angelegter Spannung und einem EOT von 3 nm gemessen. Durchbruchfeldstärken von hexagonalem $GdScO_3$ auf GaN liegen über $2\,MVcm^{-1}$.

Contents

List of Figures

List of Tables

1 Introduction

Transistors are the most common and manifold devices used in electronics today. They are employed as single transistors or in millions on integrated circuits for chip technology and are implemented for various tasks in calculators, digital cameras, computers, smart phones and huge data processing centers.

For chip technology metal oxide semiconductor field effect transistors (MOSFETs) are the essential elements. In the last decades a lot of efforts have been undertaken to make them ever smaller, faster and more energy efficient. For a long time the scaling of the device size was the main tuning parameter to achieve these goals. Approaching the physical limits of scaling also other parameters were adjusted, such as the geometry of the device and the implemented materials. E.g. FinFETs were introduced to increase the gate area with respect to the channel volume and SiO_2 was replaced by HfO_2 as gate dielectric to maintain a high capacitance without an increase in leakage currents through the gate.

The characteristics of a MOS stack are essential for the functionality of the respective MOSFET. In this work the focus is put on the O - the oxide - of MOS stacks.

The oxide electrically isolates the gate electrode from the channel, thus a good insulator is needed. Further, for appropriate switching behavior the gate capacitance has to be maximized and the density of traps, especially of interface traps, has to be kept low. Besides geometry considerations a high capacitance can be achieved by choosing an oxide with high relative permittivity κ.

There is a tendency for oxides that the band gap decreases as the permittivity increases, compare Fig. 1.1. Thus there is not one material with the largest band gap and the highest permittivity at the same time. Nevertheless, some materials stand out, i.e. $GdScO_3$ and $LaLuO_3$, demonstrating a high permittivity and a sufficient band gap above 5 eV [1]. These materials need to be identified to optimize future transistors.

Oxides with a high permittivity and good insulating behavior are not only important for standard Si based MOSFETs, but also for other devices such as dynamic access memories or high electron mobility transistors (HEMTs) based on III-nitrides. For such devices the scalability to nanometer sizes is not the main focus. Instead it is essential that the oxide films can withstand high voltages and high temperatures without degradation or even breaking of the oxide. Apart from the difference in voltage and power regime that is required, in all MOS based devices a stable insulator with high permittivity is needed.

In this work oxides are developed with the aim to find higher κ oxides with good dielectric properties for standard silicon based MOSFETs on the one hand and for other transistor types such as HEMTs based on GaN on the other hand. For the application at hand smooth and stable layers are a prerequisite besides the dielectric properties.

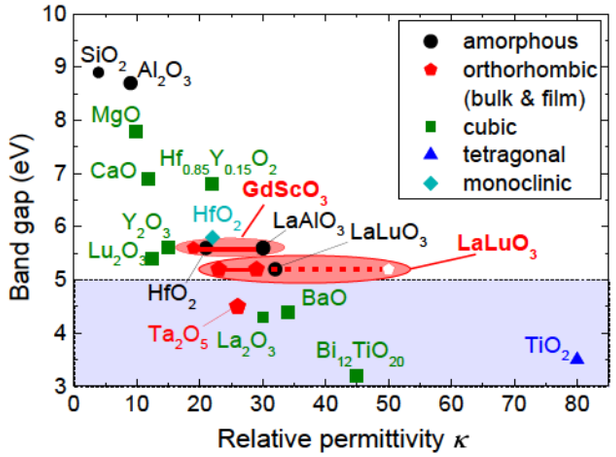

Figure 1.1: Permittivity κ versus band gap E_g for various oxides. Band gaps of gate dielectrics are supposed to be larger than 5 eV [1]. Thus oxides in the blue marked region are not suitable as gate dielectric. Data taken from [2] for SiO_2, Al_2O_3, La_2O_3, TiO_2, Ta_2O_5, Y_2O_3, [3] for MgO, Lu_2O_3, CaO, BaO, $Bi_{12}TiO_{20}$, m-HfO_2, [4] for $LaAlO_3$, [5–8] for a-HfO_2, $GdScO_3$, bulk $LaLuO_3$, [9] for a-$LaLuO_3$, [10] for film o-$LaLuO_3$, [11, 12] for $Hf_{0.85}Y_{0.15}O_2$

After this introduction, Chapter 2 will give the theoretical background useful to follow the discussion on crystal structure and on MOS characteristics in the main chapters of this work. Chapter 3 presents the experimental processes and equipment used to fabricate test devices and to characterize them both structurally and electrically.

Chapter 4 deals with the doping of HfO_2. The aim of doping is a phase transformation of the HfO_2 films to enhance the permittivity. After the stoichiometry, thickness and smoothness of the films are ascertained, the oxide layers are optimized with respect to their permittivity. This is done by analysis of capacitance voltage (CV) curves for different oxide thicknesses. Furthermore band gap, leakage currents and density of interfacial traps are determined in order to assure the suitability as a gate dielectric. Later on the origin of the permittivity of the different oxides is correlated to the crystal structure.

In Chapter 5 epitaxial oxides - $GdScO_3$ and $LaLuO_3$ - deposited on GaN are investigated because both oxides are promising dielectric candidates (cf. Fig. 1.1). Unexpectedly, a hexagonal phase of both oxides forms on GaN and thus the structure and crystallinity of these phases are investigated in detail. Additionally, the cubic forms and other growth templates are considered to gain further information on the phases and phase stability. In the second part permittivity, band gap and leakage currents are determined to judge the dielectric behavior of the new oxides.

In Chapter 6 density functional theory calculations on the crystal structure and energy of formation of crystalline $GdScO_3$ are presented. These results are compared to the experimentally stabilized polymorphs with the aim to gain further insights on why a certain phase is favored and how stable it is.

The last chapter, Chapter 7, summarizes the results collected in Chapters 4 to 6.

2 Theoretical background

The following chapter tries to cover the physical basics needed for analysis and discussion of the acquired data. It will start with some fundamentals about crystal structures and will then switch to the electrical properties of oxide insulators with a focus on the relative permittivity and the technique to extract it from capacitance voltage measurements on metal oxide semiconductor capacitors (MOSCaps).

2.1 Crystallography

A significant part of this work treats the determination of the crystal structure of epitaxial or polycrystalline oxide films. A crystal can be described as a basis (composed of the smallest set of atoms that can be repeated to form the whole crystal) and a point lattice type which describes the translational characteristic of the basis in the crystal. The direct lattice sites can be described by the vector $\mathbf{R} = m\mathbf{a} + n\mathbf{b} + p\mathbf{c}$ with $\mathbf{a}$, $\mathbf{b}$, $\mathbf{c}$ the lattice vectors and m, n and p integers. There are seven possible crystal systems that are used to describe all crystal systems which differ in their degree of symmetry, compare Tab. 2.1.

a, b, c and α, β and γ describe the lengths of the lattice vectors (lattice constants) and the angles between the lattice vectors for a unit cell, which contains the basis and is repeated along the three axis defined by a, b and c [13].

A crystal lattice can also be described in reciprocal space. The reciprocal lattice basis

Lattice constant	Angle	Crystal system
$a \neq b \neq c$	$\alpha \neq \beta \neq \gamma \neq 90°$	triclinic
$a \neq b \neq c$	$\alpha = \gamma = 90°, \beta \neq 90°$	monoclinic
$a \neq b \neq c$	$\alpha = \beta = \gamma = 90°$	orthorhombic
$a = b \neq c$	$\alpha = \beta = \gamma = 90°$	tetragonal
$a = b \neq c$	$\alpha = \beta = 90°, \gamma = 120°$	hexagonal
$a = b = c$	$\alpha = \beta = \gamma \neq 90°$	rhombohedral
$a = b = c$	$\alpha = \beta = \gamma = 90°$	cubic

Table 2.1: The seven crystal systems defined by the relation between their lattice constants and angles [13].

vectors $\mathbf{a}^*$, $\mathbf{b}^*$ and $\mathbf{c}^*$ are defined by the ones of the direct lattice:

$$\mathbf{a}^* = 2\pi\frac{\mathbf{b}\times\mathbf{c}}{\mathbf{a}\cdot\mathbf{b}\times\mathbf{c}} \quad \mathbf{b}^* = 2\pi\frac{\mathbf{c}\times\mathbf{a}}{\mathbf{a}\cdot\mathbf{b}\times\mathbf{c}} \quad \mathbf{c}^* = 2\pi\frac{\mathbf{a}\times\mathbf{b}}{\mathbf{a}\cdot\mathbf{b}\times\mathbf{c}} \tag{2.1}$$

Like $\mathbf{R}$ describes the different lattice points in direct space, a general reciprocal lattice vector can be defined by $\mathbf{G} = h\mathbf{a}^* + k\mathbf{b}^* + l\mathbf{c}^*$ for the reciprocal space covering all lattice points of the reciprocal lattice. The integers h, k, l are called Miller indices and are used to describe lattice planes of a crystal. The (hkl) plane is the plane that has intercepts with the x-, y- and z-axis at $1/h$, $1/k$ and $1/l$, respectively [13].

For hexagonal lattices also the notation in the *Miller Bravais Indexing* is used. In this case three instead of two axis are used in plane with an angle of 60° between each of them. In this notation the planes are described with four indexes $(hkil)$ with $i = -(h+k)$ [14, 15].

2.1.1 Epitaxy

Epitaxy or epitaxial growth is the growth of a crystalline layer on a bulk crystal substrate. If the substrate and the growth material have the same in plane lattice constants, lattice matched growth occurs, see Fig. 2.1 (a). If the two crystals have different lattice constants, initially the epitaxial layer forms a strained layer (Fig. 2.1 (b)), until the strain becomes too big and the layer relaxes, compare Fig. 2.1 (c). In this case misfit defects or misfit dislocations form at the interface. Such dislocations are typically unwanted at interfaces that are important for electrical characteristics, for example at the interface between oxide and semiconductor in a MOS structure (compare Section 2.7) because they give rise to electrical defects like charges at the interface.

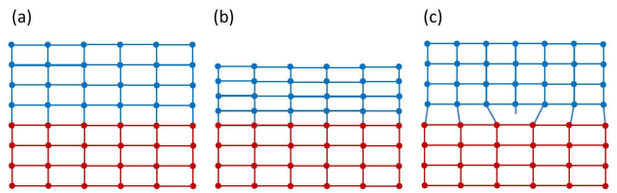

Figure 2.1: Schematic of epitaxy of (a) lattice matched, (b) strained and (c) relaxed layers.

The lattice mismatch ϵ is an indicator for the extent of the mismatch

$$\epsilon = \frac{a_e - a_s}{a_s} \tag{2.2}$$

with a_e and a_s the in plane lattice constants of the epitaxial layer and the substrate, respectively [16].

The so-called critical thickness t_c describes the thickness, when the strained, epitaxial layers relax. It roughly obeys the following empirical formula:

$$t_c = \frac{a_e^2}{2\,|a_e - a_s|}. \tag{2.3}$$

More details on when and how relaxation occurs can be found in the works of Matthews and Blakeslee [17–19].

2.2 Gate dielectric requirements

When trying to find the optimum gate dielectric for the application in Si or III-V MOS devices, various requirements have to be fulfilled [6, 11]:

- For good switching behavior of a transistor, both the transconductance g_m and the drain conductance g_D are supposed to be large and both depend linearly on the gate capacitance C in inversion:

$$g_m = \frac{\partial I_D}{\partial V_{GS}}|_{V_{DS}=constant} \propto C \tag{2.4a}$$

$$g_D = \frac{\partial I_D}{\partial V_{DS}}|_{V_{GS}=constant} \propto C \tag{2.4b}$$

  where I_D the drain current, V_{DS} the drain source voltage and V_{GS} the gate source voltage [20].

  Hence, for a good gate control, the oxide capacitance should be maximized. It depends on the area of the capacitor A, the oxide thickness d, the vacuum permittivity ϵ_0 and the relative permittivity of the oxide κ [21]:

$$C = \frac{\epsilon_0 \kappa A}{d}. \tag{2.5}$$

  Apart from geometry considerations, the only parameter that can influence C is the relative permittivity κ which is a material property, see also Section 2.4. In this work it is one of the major goals to find high κ oxides.

- Secondly a good insulation between gate and semiconducting channel has to be ensured. Leakage currents should be avoided to keep the energy consumption as low as possible. A necessity for good insulating properties is a high band gap E_g above 5 eV [6]. For sufficiency the band offsets for both, the valence bands and the conduction bands between oxide and semiconductor, have to be above 1 eV, better even above 1.5 eV. This way hole and electron based leakage is kept small. Unfortunately its more complex to determine the band offsets compared to the band gap itself. Furthermore, to keep leakage low, the effective electron mass has to be as high as possible (see Section 2.8) and defects that can promote current transport have to be avoided.

- The oxides have to be thermodynamically stable in contact with the substrate.
- Film morphology and microstructure need to be sufficiently good, the interface should be atomically smooth.
- The density of interface traps has to be kept low.
- The oxide must be compatible with the gate electrode.
- The reliability of the MOS devices over time has to be secured.
- The fabrication costs should be as low as possible.
- Scalability needs to be tested. Thin films change their characteristics compared to bulk materials. Hence a high band gap and a high permittivity of bulk oxides do not necessarily guarantee good performance in scaled devices with oxide thicknesses of 5 nm and less.

The specific demands for a certain application can differ and an oxide that is not optimal for standard Si MOSFETs might still be suitable for high power devices based on III-V semiconductors. Especially for standard Si MOSFETs it is important that the devices can be scaled down and that no diffusion or chemical reaction occurs during high temperature anneals because such anneals are needed for dopant activation in source and drain. On the other hand for special, alternative substrates like Ge with a small fraction of Sn it is necessary that the whole production process can be executed at low temperatures for otherwise the Sn would diffuse out [22]. For such substrates the oxide deposition temperature has to be kept low. For high power applications on III-V semiconductors like GaN the scalability is not the main issue, but rather high electrical strength, i.e. high breakdown electric fields.

Not all aspects can be investigated in this work, but the two main ones - permittivity and band gap - will be discussed in detail and also other aspects will be addressed. Hence, the next sections will give a basic understanding of these terms and how they can be evaluated.

2.3 Band gap

The simplest way to distinguish between metals, semiconductors and insulators is to look at their band gap which is the difference between the highest occupied energy level and the lowest unoccupied energy level, compare Fig. 2.2. In equilibrium all energy states are filled up with electrons up to the so called Fermi energy E_F. In metals the energy bands are so dense around the Fermi level, that there is effectively no gap at all. The band is half filled and the electrons are free to move and can contribute to charge conduction. Insulators have a large band gap and hence a high energy is needed to excite electrons from the valence band E_V to the conduction band E_C. If this energy is not given, the valence band stays completely filled and the conduction band completely unoccupied and no charge transport is possible. Amorphous HfO_2, a widely used insulator in MOS devices,

has a band gap of 6 eV [23]. Also semiconductors show a band gap but it is much smaller than for insulators and the thermal energy, for example at room temperature, is enough to excite individual electrons to the conduction band. These electrons and the emerging holes can contribute to conduction [13]. Si and GaN, the two semiconductors used in this work, show band gaps of 1.12 eV and 3.44 eV at room temperature, respectively [16].

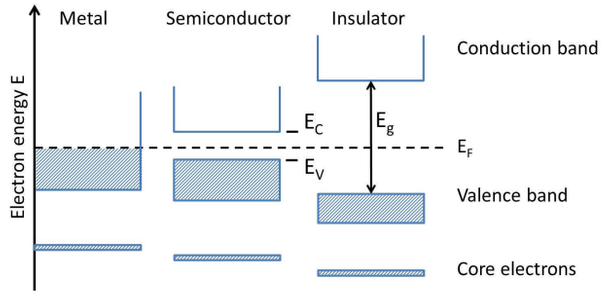

Figure 2.2: Schematic of the energy bands of metals, semiconductors and insulators, adapted from [13], with valence band E_V, conduction band E_C, energy band gap E_g and Fermi energy E_F.

Of course the schematic in Fig. 2.2 is a simplified picture of the band gap. The energy levels depend on the reciprocal wave vector k and their courses can be quite complex.

In this work the band gaps of $GdScO_3$, $LaLuO_3$ and Lu doped HfO_2 are determined to judge their insulating properties.

2.4 Relative permittivity κ

In MOSFET devices good gate control is one of the major demands and, as described above, gate control can be impacted by the capacitance. One way to enhance the capacitance is to increase the area A and to decrease the oxide thickness d. However A is wanted to be decreased to reduce structure sizes and this rather contributes to a decrease of the capacitance than an increase. The oxide thickness can be reduced, but at a certain thickness leakage currents start to increase dramatically with decreasing thickness (compare Section 2.8). Though, the thickness decrease is limited. The last possible parameter that can be changed is the relative permittivity which is a material constant for a given frequency.

The relative permittivity κ, or the electric susceptibility $\chi = \kappa - 1$, describe the proportionality factor between the dielectric polarization density P in a material induced by the electric field E:

$$P = \epsilon_0(\kappa - 1)E = \epsilon_0 \chi E. \tag{2.6}$$

The polarization can originate from electrons that are displaced respective their nucleus because the centers of the negative and positive charges are moved apart from each other

(electronic polarization) and from displaced positive ions respective the negative ions (ion polarization). Further there can be contributions to the polarization from free charges in the material or at the surface and from oriented polar molecules [24]. Due to the different masses of the particles that contribute to the polarization, they start to affect κ at different frequencies. Larger masses cannot follow high frequencies and though do not contribute to κ any more, compare Fig. 2.3. For frequencies used for modern CMOS technology only ionic and electronic contributions determine the relative permittivity.

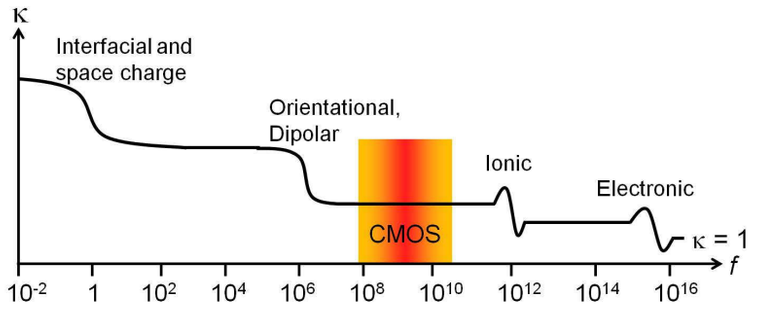

Figure 2.3: Schematic of the frequency dependence of the relative permittivity κ, adapted from [2]. The regions, where the different polarization mechanisms start, are marked.

The permittivity presented so far is just the real part of the complex dielectric function $\epsilon = \epsilon_1 + i\epsilon_2$ which is related to the complex refractive index $\tilde{n} = n + ik$ [25]:

$$\epsilon = \tilde{n}^2 \quad \Longleftrightarrow \quad \epsilon_1 = n^2 - k^2 \qquad \epsilon_2 = 2nk \tag{2.7}$$

From the imaginary part of the refractive index k, the absorption coefficient α is given by $\alpha = 4\pi k/\lambda$ where λ is the wave length. This relation will be used to determine the band gap of Lu doped HfO_2 from ellipsometric measurements in Section 4.5.1.

2.4.1 Clausius-Mossotti equation

Rudolf Clausius and Ottaviano Fabrizio Mossotti derived a formula for the relative permittivity as a function of the molecular polarizability α and the molecular volume V_m, compare [11, 26]. The Clausius Mossotti equation is described by:

$$\kappa = \frac{3V_m + 8\pi\alpha}{3V_m - 4\pi\alpha}. \tag{2.8}$$

Even though the assumption of a symmetric crystal was used, the Clausius-Mossotti equation 2.8 offers the possibility to roughly estimate the permittivity of a material or at least see a tendency in κ for a change of composition or phase. The molar volume V_m can

Ion	O^{2-}	Al^{3+}	Si^{4+}	Sc^{3+}	La^{3+}	Gd^{3+}	Er^{3+}	Lu^{3+}	Hf^{4+}
α_{ion} (Å^3)	2.01	0.79	0.87	2.81	6.07	4.37	3.81	3.64	3.25

Table 2.2: Important ion polarizabilities [11, 27]

be derived from the density or from the lattice parameters of the unit cell and the number of formula units Z.

The polarizability follows the additivity rule stating that α is the sum of the polarizabilities of the components of the material. This rule is also true for ion polarizabilities even though they cannot be measured directly. Shannon for example fixed the polarizability of O^{2-} to 2.01 Å^3 and determined the polarizabilities for various metal ions from the total polarizability of their oxides which can be measured [27].

For a perovskite of the form ABO_3 the polarizability yields to the sum of the ion polarizabilities:

$$\alpha(ABO_3) = \alpha(A^{3+}) + \alpha(B^{3+}) + 3 \cdot \alpha(O^{2-}). \tag{2.9}$$

In all the cases where α is estimated using the additivity rule in this work, the ion polarizabilities were taken from Tab. 2.2.

From the Clausius-Mossotti equation one can see how the permittivity can be enhanced: either the molar volume is reduced which is related to a change in phase, or ions are exchanged by ions with a higher polarizability.

2.5 Band gap against dielectric constant

As described in Section 2.2, both, low leakage currents, which are related to large band gaps, and a high permittivity are required for adequate dielectric materials. Unfortunately, typical dielectric candidates have the tendency to have lower band gaps with increasing dielectric constant, see Fig. 1.1 [1, 4, 6]. This tendency correlates with the atomic number of the elements: the band gap of metal oxides tends to decrease with increasing atomic number in a particular group of the periodic table, while the permittivity increases due to increasing polarizability [11, 27]. This behavior can partly be explained by the orbitals forming the band gap. In SiO_2 all s and p electrons are filled and the band gap is defined by the oxygen electron lone pair energy level (valence band maximum) and the σ^* antibonding orbital energy level (conduction band minimum), which is rather high. Transition metal oxides have additional available energy states due to partially filled d orbitals, which lie within the gap defined by the σ and σ^* orbitals and reduce the band gap [11].

Nevertheless, this is just a trend and especially the ternary oxides show higher permittivity compared to the corresponding binary oxides without a reduction of the band gap. In Fig. 1.1 this becomes clear for the example of La_2O_3, Lu_2O_3 and $LaLuO_3$. Thus it is worth to test the various ternary oxides individually.

2.6 Capacitance equivalent thickness

Capacitance voltage (CV) measurements are used to determine the permittivity of a material experimentally. The capacitance is measured for several oxide thicknesses and the oxide capacitance C, the maximum capacitance in accumulation (compare Section 2.7) is used to determine the so called capacitance equivalent thickness (CET). The CET equals the thickness that a pure SiO_2 layer would have with the same capacitance per area as the one measured and on the same semiconducting substrate:

$$CET = \frac{\epsilon_0 \kappa_{SiO_2} A}{C}. \tag{2.10}$$

Typically the total capacitance adds up out of several single capacitances. For examples for Si based MOSCaps (metal oxide semiconductor capacitors) normally a SiO_2 interface is present and hence, the total capacitance and CET have two contributions. Also other 'interfacial' layers are possible: e.g. in the case of epitaxial growth on Si (111) an auxiliary Y_2O_3 layer is used which also adds up to the CET. In the typical experiments presented here the interfacial CET can be seen as a constant, while the CET caused by the high-κ oxide changes with thickness. Hence, the total measured CET can be expressed by a linear equation

$$CET = \frac{\kappa_{SiO_2}}{\kappa_{high-\kappa}} \cdot d_{high-\kappa} + CET_{IL} \tag{2.11}$$

with CET_{IL} the y-axis intercept and $\kappa_{SiO_2}/\kappa_{high-\kappa}$ the slope. Thus, the permittivity of the high-κ oxide can be deduced from the slope of a linear regression performed on the measured CET as a function of oxide thickness. In addition, interfacial layer thicknesses can be estimated from the y-axis intercept. κ_{SiO_2} is set as 3.9 for the entire work, following [28].

Besides CET, many works refer to the equivalent oxide thickness (EOT). In a MOSCap not only the oxide layers contribute to the total capacitance, but also the semiconductor itself. Applying quantum mechanics, the wave functions of the carriers in the semiconductor are near zero at the interface to the oxide due to the high barrier. Hence, the maximum number of carriers is located approximately 10 Å away from the interface for Si [16]. Si has a relative permittivity of 11.9 [16] which gives an additional contribution to the CET of 4 Å, which is called the quantum mechanical contribution to the CET. The EOT only considers the oxide contribution to the total capacitance and thus the EOT can be derived from the CET by subtracting the quantum mechanical contribution [28]:

$$EOT = CET - 4\,\mathring{A} \tag{2.12}$$

2.7 MOS capacitor

MOSCaps represent the key devices used here to characterize the deposited oxide films electrically. A MOSFET, a widely used device used in integrated circuits (ICs), can be regarded as a MOSCap with p-n junctions (a junction between p- and n-type region in

a semiconductor) at two ends, compare Fig. 2.4. Hence, many of the characteristics of a MOSFET important for performance can be analyzed investigating the much simpler MOSCap. This is especially true for the oxide between gate electrode and substrate.

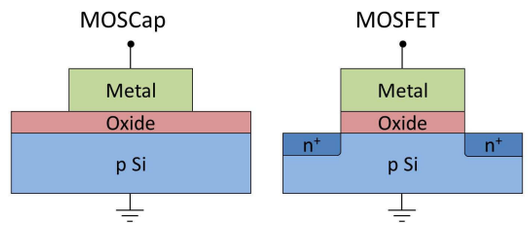

Figure 2.4: Schematic of a MOSCap and a MOSFET with the metal in green, the oxide in red and the semiconductor in blue. The MOSFET can be regarded as a MOSCap with p-n junctions at two ends.

In order to comprehend the behavior of the capacitance as a function of voltage in a MOSCap one can start with the energy band diagram of a MOS structure. Fig. 2.5 represents the band diagram of an ideal MOS or MIS (metal insulator semiconductor) structure for a p-type Si substrate. For simplicity the following explanations will all refer to the p-type Si case which is commonly present in this work. The n-type case (GaN substrates are typically n-type in this work) follows the same rules and results simply in a change of sign in the course of the CV.

Ideal MOSCap means that there are no trap charges present and that there is no carrier transport through the oxide. Furthermore it is assumed that the metal is chosen in that way that the difference between the work functions of the metal and the semiconductor are zero. The work function is the minimum energy necessary for an electron to leave the Fermi level into vacuum. Hence, for the ideal MOSCap assumed here and for zero applied voltage the energy bands of the semiconductor are not bended, compare Fig. 2.5. This is called flat-band condition [16].

When a negative voltage, also called bias, is applied to the metal side, the conduction and valence band of the semiconductor bend upward, the valence band gets close to the Fermi level and holes (the majority charge carriers in a p-type semiconductor) accumulate close to the oxide interface, compare Fig. 2.6 (a). This state is called accumulation. During accumulation the capacitance is at its maximum and is solely impacted by the oxide capacitance, see Fig. 2.7. This is the capacitance value used in a *CET*-plot, compare Section 2.6.

In the case of positive applied voltage the energy bands of the semiconductor bend downward and both the conduction band and the valence band in the interface region are far away from the Fermi level, see Fig. 2.6 (b). No charges can accumulate and hence this state is called depletion. This depletion region contributes to the total capacitance and thus

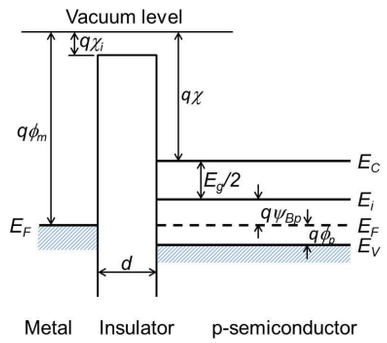

Figure 2.5: Band diagram of an ideal MOS structure with E_F the Fermi level, q the charge of a hole/electron, ϕ_m the metal work function, χ_i the oxide electron affinity, d the oxide thickness, χ the semiconductor electron affinity, E_g the band gap of the semiconductor, E_C and E_V the conduction and valence band of the semiconductor, E_i the mid gap energy of the semiconductor, ψ_{Bp} the energy difference between E_F and E_i and ϕ_p the energy difference between E_F and E_V, after [16].

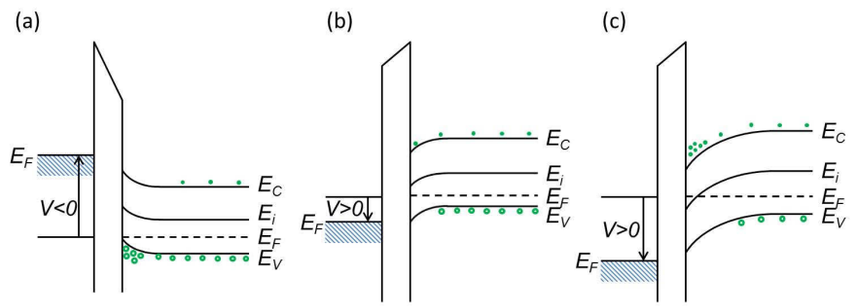

Figure 2.6: Band diagram of a MOS structure with a p-type semiconductor for different applied voltages V, after [16].

the total capacitance is smaller than the one of the sole oxide measured in accumulation, compare Fig. 2.7.

When an even higher positive bias is applied to the metal the energy bands of the semiconductor bend even more and the conduction band gets close to the Fermi level. Now electrons (the minority charge carriers) can accumulate close to the oxide interface, cf. Fig. 2.6 (c). This is called inversion and the total capacitance rises again. This can only by measured when the used AC frequency is low enough. Otherwise (at high frequencies) the thermal generation rate for the minority carriers is too low and the total capacitance stays low [16], compare Fig. 2.7. This is the case for the MOSCaps investigated in this work for measuring frequencies of 100 kHz.

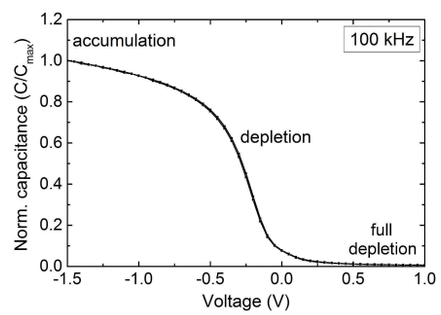

Figure 2.7: Example of a CV curve: a voltage is applied between the p-type semiconductor and the metal gate with a high frequency AC signal (100 kHz).

As mentioned above these considerations are based on the assumption that the MOS structure is at flat band condition when no bias is applied. This is typically not given in real structures: the metal work function (some examples for metal work functions are listed in Fig. 2.8) and the semiconductor work function (≈ 4.8 eV for Si [16]) can differ and thus the energy bands are bended without an applied voltage. To restore the flat band condition a voltage has to be applied that equals the difference in work function. The voltage is called flat band voltage V_{fb}. Hence, the CV curve follows the same course as the ideal one, but it is shifted along the voltage axis by V_{fb}.

Further traps have an impact on the course of measured CV curves. Charged traps are present in any oxide and thus also shift the CV curve and the flat band voltage. For this reason additionally to the vacuum work function also effective work functions found for SiO_2 and HfO_2 devices are incorporated in Fig. 2.8.

The flat band voltage can be determined from different methods. In this work the method proposed by Hillard et al. was applied: The position of the maximum of the second derivative of $(1/C(V)^2)$ was defined as the flat band voltage [33]. In case of high interface trap densities errors may occur, but for similar interface trap densities the shift

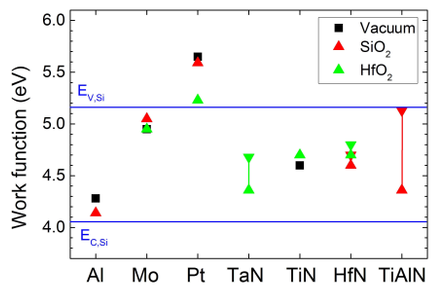

Figure 2.8: Vacuum work function and effective work functions on HfO_2 or SiO_2 for different pure metals and nitrides [29–32]. Additionally the conduction and valence bands of Si ($E_{C,Si}$ and $E_{V,Si}$) are marked.

should be the same for different samples. Thus, this method was chosen due to its simplicity and practicability respective the measured data and because differences in flat band voltage compared to other oxides are most interesting rather than the absolute values. (For a more precise flat band voltage determination additional data sets would be needed [34].)

2.7.1 Traps

There are different kinds of traps that influence the CV behavior, compare Fig. 2.9. Interface traps are located at the semiconductor oxide interface and have energy levels within the band gap of the semiconductor. They can act as donors or acceptors and thus can be charged. If the amount of interfacial trapped charges Q_{it} is high enough, they can shift the flat band voltage and stretch out the CV curve. Further they degrade the channel mobility due to scattering. The main type of interfacial trap is the so-called P_b center. Because the periodic lattice structure is interrupted at the transition from the Si crystal to the amorphous or polycrystalline oxide, Si atoms exist, where three of the four valence electrons are bonded to the Si crystal, while the last one does not build up a bond and is called dangling bond. By releasing this electron or adding another electron the P_b center gets charged. A typical method to reduce the number of P_b centers and hence the number of interface charges is to add hydrogen which can passivate the dangling bond such as in the following reaction [16, 35]:

$$Si_3 \equiv Si\bullet + H_2 \rightarrow Si_3 \equiv SiH + H. \tag{2.13}$$

Fixed oxide charges Q_f are also located near the interface, but their energy levels don't fall into the energy band gap of the semiconductor and thus do not interact with carriers having energies in the semiconductor band gap. They are immobile and also shift the flat band voltage [35].

Mobile ionic charges Q_m are charged traps that can move depending on the applied bias. The origin can be hydrogen or sodium and potassium ions originating from the process

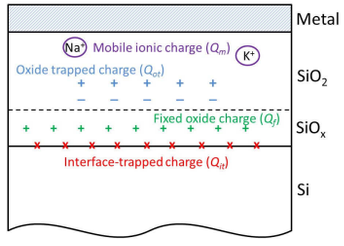

Figure 2.9: Schematic of oxide traps in a MOS stack having influence on the CV behavior of a MOSCap, adapted from [16].

environment. The mobile charges cause shifts of the CV curve between trace and retrace measurements. The difference in trace and retrace is called hysteresis. Hysteresis effects should be avoided to ensure that on and off switching of a device occur at the same voltage [16, 35].

The last kind of traps are oxide trapped charges Q_{ot} originating from imperfections in the oxide atomic structure, namely oxygen vacancies. In HfO_2 the oxygen is normally bonded to four Hf atoms. A missing oxygen atom forms an electron trap which can capture up to four electrons and thus exists in the charge states (+2), (+1), (0), (-1) (-2) [35]. The vacancies which are initially neutral can be charged by currents passing the oxide, by hot-carrier injection or by photo excitation and can also attribute to shifts of the CV course [16].

2.7.2 Conductance method

As mentioned above, also the interface traps contribute to the characteristics of the CV course: the additional charges form an additional capacitance C_{it} and losses due to capture and emission of carriers can be regarded as a resistance R_{it} [21].

Nicollian and Goetzberger developed a method to determine the density of interface traps analyzing the conductance measured during CV [36].

The components contributing to the total capacitance and conductance during CV measurements are plotted in the equivalent circuit in Fig. 2.10 (a).

The representation of the equivalent circuit can be simplified, compare Fig. 2.10 (b). The newly defined parameters C_P and G_P are given by

$$C_P = C_S + \frac{C_{it}}{1 + (\omega\tau_{it})^2} \tag{2.14}$$

$$\frac{G_P}{\omega} = \frac{q\omega\tau_{it}D_{it}}{1 + (\omega\tau_{it})^2} \tag{2.15}$$

where $\omega = 2\pi f$ with f the measurement frequency, $D_{it} = C_{it}/q^2$ the density of interfacial traps with q the carrier charge and $\tau_{it} = R_{it}C_{it}$ the interface trap time constant [21].

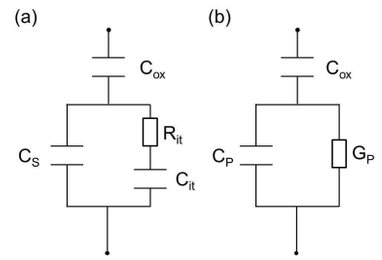

Figure 2.10: Equivalent circuit model for conductance measurements for (a) a real MOSCap and (b) a simplified circuit. Sketches adapted from [21].

The capture and emission rate τ_{it} is described by the Shockley-Read-Hall statistics [21, 37]:

$$\tau_{it} = \frac{1}{\sqrt{(3k_BT/m^*)}\,\sigma N_A} \cdot e^{q\phi_s/k_BT} \tag{2.16}$$

where k_B the Boltzman constant, T the temperature, m^* the effective mass, σ the conductivity, N_A the doping concentration and ϕ_s the surface potential.

Mostly the traps near the Fermi level contribute to the capture and emission processes and thus G_p/ω can be approximated by [21]:

$$\frac{G_p}{\omega} = \frac{qD_{it}}{2\omega\tau_{it}} ln[1 + (\omega\tau_{it})^2]. \tag{2.17}$$

This function has its maximum at $\omega = 2/\tau_{it}$ and there the D_{it} can be reduced to [21]:

$$D_{it} = 2.5\,\frac{G_p}{q\omega}. \tag{2.18}$$

This approximation is used to determine the density of interfacial traps in this work.

2.8 Charge carrier transport in insulators

When describing the dependence of the capacitance on the applied voltage above, for simplicity, it was assumed, that no charges can pass the insulating oxide. In real devices carrier transport through the oxide is present to some degree.

The critical parameters determining the degree of leakage are insulator thickness, valence band and conduction band offsets between semiconductor and oxide, effective mass of the charge carrier passing through the oxide film, trap distribution in the oxide and temperature.

When substituting SiO_2 by high κ oxides, a thicker oxide film can be chosen to reach the same capacitance. Unfortunately, this thickness increase does not guarantee lower leakage

because the band offsets are typically lower for high κ materials (compare also Fig. 1.1) and the effective masses of high κ oxides are typically 50 % lower than for SiO_2 [35].

The lowest possible leakage current is governed by direct tunneling. In quantum mechanics the electron wave function can penetrate into a potential barrier, even though the electron energy is lower than the potential height, due to the Heisenberg uncertainty relation [35]. For finite barrier height and width there is a certain probability P that an electron can even pass through the barrier $U(x)$. This process is called tunneling.

G. Wentzel, H. A. Kramer and L. Brillouin derived the so-called WKB approximation to deduce a general formula for the tunneling probability P. Instead of using Bloch waves, they used a complex plane wave to describe the wave function Ψ of the electron headed towards the potential barrier $U(x)$, which is higher than the electron energy E between $x = 0$ and $x = x_0$:

$$\Psi(x) = exp[iK(x)x], \tag{2.19}$$

where i the imaginary number and $K(x)$ the wave number [35].

The corresponding stationary Schrödinger equation is given by

$$\left[-\frac{\hbar^2}{2m^*}\frac{d^2}{dx^2} + U(x)\right]\Psi(x) = E\Psi(x), \tag{2.20}$$

where m^* is the effective mass.

For $0 < x < x_0$ $K(x)$ becomes imaginary and $\Psi(x)$ follows a decreasing exponential function. The Schrödinger equation can be solved using some simplification of the second derivative of $\Psi(x)$ and reveals the electron tunneling probability in the WKB approximation [35]:

$$P(x_0) = |\Psi(x_0)|^2 = exp\left[-2\frac{(2m^*)^{1/2}}{\hbar}\int_0^{x_0}(U(x) - E)^{1/2}dx\right]. \tag{2.21}$$

The integral in the WKB approximation can be solved for the direct tunneling probability P_t through an oxide potential barrier:

$$P_t = exp\left[-\frac{8\pi}{3}\frac{(2m^*)^{1/2}}{h}\frac{d}{qV_{ox}}\left(\Delta E_C^{3/2} - (\Delta E_C - qV_{ox})^{3/2}\right)\right] \tag{2.22}$$

where d the oxide thickness, q the charge of the carrier, V_{ox} the oxide potential andΔE_C the conduction band offset [35, 38]. This form of the WKB demonstrates that the tunneling currents depend on the oxide thickness, the effective mass, the positions of valence and conduction band with respect to the semiconductor ones and the electric field.

In case that the effective mass changes with x ($m^* = m^*(x)$), e.g. the electron has to penetrate two different oxides such as an interfacial SiO_2 and a high κ oxide, $m^*(x)$ cannot be pulled out of the integral as it was done in Eq. 2.21 for a homogeneous insulator. As mentioned above, high κ oxides typically have lower effective masses compared to SiO_2 and thus the tunneling probability increases.

Besides direct tunneling where the electron has to tunnel along the complete oxide thickness (Fig. 2.11 (a)), in case of a high enough applied voltage the electron only has to overcome a part of the oxide barrier by tunneling, compare Fig. 2.11 (b). This tunneling process is called Fowler-Nordheim tunneling [35].

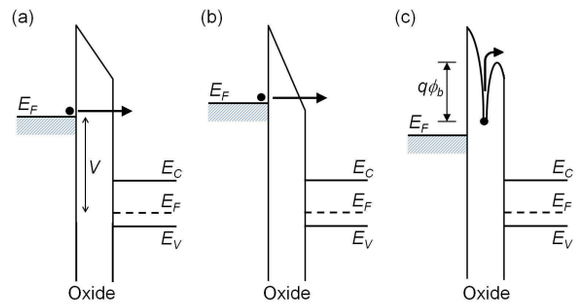

Figure 2.11: Schematic of conduction mechanisms in insulators: (a) direct tunneling, (b) Fowler-Nordheim tunneling, (c) Poole-Frenkel emission, adapted from [16].

Traps in the oxide offer additional leakage paths and increase the total leakage current. In case of traps with lower energy than the electron energy, the potential $U(x)$ is lowered and therefore the tunneling probability rises [35].

For the case that the trap state and the electron are positioned on the same energy level, a two step tunneling process via the trap state is possible. The probability that the electron transmits through the barrier equals $P_{t1}P_{t2}/(P_{t1} + P_{t2})$ where P_{t1} and P_{t2} denote the probabilities to tunnel from the metal to the trap state and from the trap state to the semiconductor conduction band, respectively. The probability of this trap assisted tunneling can be much larger than the probability for direct tunneling [35].

Also thermal excitation plays a role for carrier transport through the oxide. The probability that an electron overcomes the oxide barrier just by thermal excitation is negligible, but it is possible that electrons tunnel to a trap state and then overcome the remaining part of the barrier by thermal excitation which is called Poole-Frenkel emission [35], compare Fig. 2.11 (c).

The dominating mechanism for trap based conduction depends not only on temperature but also on the position of the trap in the barrier [35].

2.8.1 Dielectric breakdown

One concern for MOS devices is their reliability. As described above, in real devices small currents flow through the oxide barrier. The crossing charge carriers induce defects in the film and for a high density of defects, after very high currents or a long load period, breakdown occurs, i.e. leakage currents increase drastically [16].

In percolation theory breakdown is expected to occur when the defect density becomes that high, that a continuous chain of random defects forms a conduction path between the semiconductor and the metal through the oxide, compare Fig. 2.12.

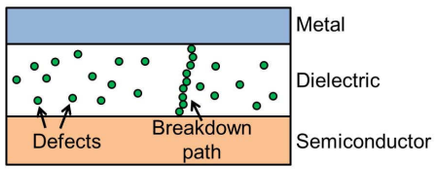

Figure 2.12: Schematic of percolation theory: Breakdown starts when the defect density is that high, that a conductive chain of defects is formed, after [16].

3 Experimental

The following chapter covers the preparation of the samples on the one hand and the methods for characterization on the other hand. Sample preparation was not the same for all experiments. Hence first a typical process is introduced, then deviations from this process for certain experiments are explained. The characterization methods mainly divide into two parts: the structural characterization and the dielectric characterization.

3.1 Sample preparation

Before the key step in the sample preparation, the oxide deposition, the substrates had to be diced into smaller pieces and they had to be cleaned properly. Depending on the purpose, different substrates were used:

- Si (001) substrates were used for the deposition of HfO_2 based oxides. The Si was p-type with a Boron doping concentration of 10^{15} atoms per cm^3. This doping level corresponds to a resistivity of 8 - 25 Ωcm.
- For the epitaxial growth of $GdScO_3$ and $LaLuO_3$, GaN (1.5 μm - 9 μm thickness) on Al_2O_3 (0001) were used as substrate material. The GaN was either intrinsic or n-type ($\approx 10^{18}$ Si atoms per cm^3)
- Thin, cubic Y_2O_3 layers deposited by molecular beam epitaxy on Si (111) (compare Tarnawaska et al. [39]) were employed as alternative growth templates for $GdScO_3$ and $LaLuO_3$ epitaxy. The Si doping level was the same as for the Si (001) substrates described above.

The original wafers had diameters between 50 mm and 200 mm. For processing they were diced into squares. The substrate sizes ranged from 5 mm $\times$ 5 mm up to 20 mm $\times$ 20 mm depending on the availability of the material and the equipment involved in the process. After dicing the substrates needed to be cleaned, as described in Section 3.1.1.

In Chapter 4 results on doped HfO_2 layers grown by atomic layer deposition (ALD) on Si (001) are presented. The material system is closely related to industrial HfO_2 based MOS technology and therefore the process used here was adopted from a standard HfO_2 MOSCap process. This included the cleaning procedures, the use of TiN as metal gate and a forming gas anneal.

A typical production cycle for the HfO_2 based MOSCaps with an ALD HfO_2 and a TiN/Al metal contact on a Si substrate is presented in Fig. 3.1: (a) before processing a

natural SiO_2 layer was present on the surface; (b) it was etched away and eventually a chemical SiO_2 was built up, then HfO_2 or other high-κ oxides and TiN were deposited by ALD and AVD®, respectively; (c) Al contacts were deposited by electron beam evaporation via shadow masks and (d) subsequently the TiN in between the contacts was removed by reactive ion etching (RIE) (d). Finally the samples were annealed in forming gas.

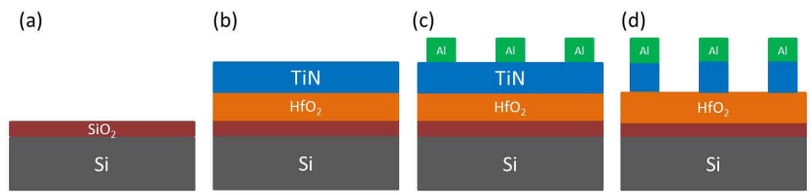

Figure 3.1: Schematic production process of a Si-based MOSCap device. (a) Before processing a natural SiO_2 layer was present on the Si surface. (b) For cleaning the native SiO_2 needed to be etched away and eventually a chemical oxide was formed. Thin layers of HfO_2 by ALD and TiN as metal gate by AVD® were deposited directly after cleaning. (c) Al-contacts were deposited by electron beam evaporation via shadow masks. (d) TiN between the contacts was etched away by RIE.

Some samples are unloaded after ALD deposition in order to conduct post oxide deposition annealing (PDA) before further processing.

In Chapter 5 novel epitaxial oxides are presented. In this case it had to be taken care that the substrates were suitable for epitaxy. The focus is put on GaN. The research on these epitaxial oxides is rather fundamental and the cleaning and MOSCap processes were kept as simple as possible to reduce the number of interfering parameters. Hence, the cleaning procedure was kept simple, no TiN was used and therefore no reactive ion etching was needed and annealing processes were not carried out for the GaN based devices.

In the case of epitaxial $LaLuO_3$ grown on GaN also Hall measurements were carried out. For this purpose Al was deposited on the four corners of the samples on top of the $LaLuO_3$ and then the samples were alloyed at 580°C for 30 s up to 800 s to diffuse the Al into the oxide layer and to build a conductive path to the underlying GaN, see Fig. 3.2.

The different process steps and deposition methods are discussed in more detail in the following Subsections 3.1.1 to 3.1.5.

3.1.1 Surface cleaning and preparation

After dicing and removing a protective resist with acetone and isopropanol further cleaning steps were carried out to improve device performance.

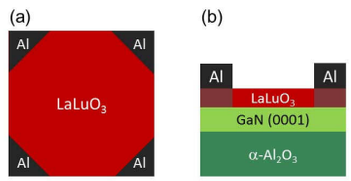

Figure 3.2: Schematic of Hall samples as (a) top view and (b) side view.

In the current work two types of cleaning procedures for Si were used. Using short names they are referred to as RCA cleaning and Semitool/MegsPD cleaning.

RCA stands for a wet-chemical cleaning procedure developed by Kern and Puotinen commissioned by the Radio Corporation of America [40]. In the slightly modified version used in this work the Si substrates are dipped manually into three different cleaning solutions for 10 minutes at 60°C. These solutions are persulfuric acid consisting of sulfuric acid (H_2SO_4) and hydrogen peroxide (H_2O_2) at a ratio of 2 to 1, SC1 (NH_3OH, H_2O_2 and deionized water (DI water) at a ratio of 1 to 4 to 20) to remove organic contamination and SC2 (HCl, H_2O_2 and DI water at a ratio of 1 to 1 to 20) to remove ionic contamination. During these cleaning steps a chemical SiO_2 forms which is removed by a subsequent dip in diluted hydrogen fluoride (1 %HF in DI water) for about 30 seconds. After each of these cleaning steps the samples are rinsed in DI water for 5 to 10 minutes. After SC2 typically no further HF dip is done because it is beneficial to have a chemical oxide at the interface. Though the chemical oxide can also be removed in a final HF dip. This case is called HF last and samples should be put quickly into an oxygen free ambient to prevent a natural SiO_2 formation on the surface.

When referred to as Semitool or MegsPD cleaned, an automatic process in the single wafer cleaning instrument *Raider SP 206* built by the company *Semitool* is used. The tool is designed for the cleaning of 200 mm and 300 mm wafers, but using adapters and adhesive tape also smaller pieces can be employed. For Si cleaning processes for which a SiO_2 layer is favored at the end a recipe shortly called MegsPD is used. The MegsPD process starts with dipping the wafer into a mixture of diluted HF and diluted HCl to remove the native SiO_2 and herewith also contamination on the wafer surface. After rinsing steps in a mixture of HCl and DI water and in pure DI water a chemical SiO_2 is build up with ozone which is dissolved in DI water. This process is self limited and leads to a homogeneous SiO_2 layer with a thickness of ca. 1.2 nm. To achieve an equivalent cleaning to the RCA HF last explained above, the first etching step in diluted HF/ diluted HCl can be repeated after the oxidation step.

The surface characteristics differ for HF last processes and the ones with a SiO_2 layer. In the first case the surface is hydrogen (H) terminated and hydrophobic, while the oxide surface is OH terminated and hygroscopic. For optimal ALD precursor reactions (see also Subsection 3.1.2) an hydroxyl (OH) terminated surface is wanted [41].

GaN cleaning was kept simpler in this work compared to Si cleaning. On GaN no natural amorphous oxide layer forms and therefore there were no concerns about oxide removal. To eliminate surface contamination the GaN was cleaned in H_2SO_4 and subsequently rinsed with DI water.

3.1.2 CVD techniques

Chemical vapor deposition (CVD) in the broadest sense is a generic term for multiple deposition techniques based on chemical reactions of vapor-phase precursors. These reactions can take place either in the gas phase or on the surface. In classical thermal CVD the reactions are stimulated by heating, while in plasma enhanced CVD the required energy is supplied by a plasma. Many abbreviations for CVD techniques include the acronym MO which simply means that metal organic precursors were used [42]. In this work three different CVD techniques are used: ALD, atomic vapor deposition (AVD®) and metal organic vapor phase epitaxy (MOVPE). One way to distinguish between the three is to compare the precursor opening times during the deposition processes, as illustrated in Fig. 3.3. During ALD the two precursors flow into the chamber as alternate pulses while in MOVPE or classical CVD all precursors run into the chamber continuously. AVD® can be seen as a mixture of the two: the metal organic precursor is pulsed, the second precursor flows continuously.

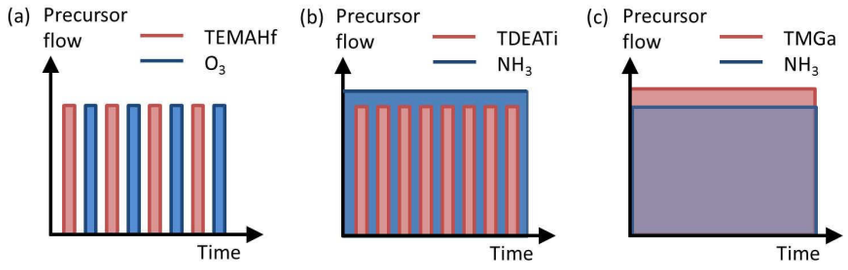

Figure 3.3: Schematics of precursor flow versus time for (a) ALD, (b) AVD® and (c) CVD.

For the presented CVD methods there were two ways to transport the precursor from the tank to the deposition chamber, here called injection mode and bubbler mode, see Fig. 3.4.

For injection mode the precursors (e.g. TEMAHf in Fig. 3.4 (a)) used were diluted in octane (C_8H_{18}) and were introduced into the evaporator by liquid injection. This means that the precursor was delivered in its liquid form up to the injector. The amount of precursor introduced per growth cycle was regulated by the opening time of the injector. Typical injection times used here were in the range of 10 ms. The injected precursor entered the evaporator, which was kept at lower pressure and higher temperature, and instantly

vaporized. This vapor was purged through the showerhead into the chamber to the sample surface.

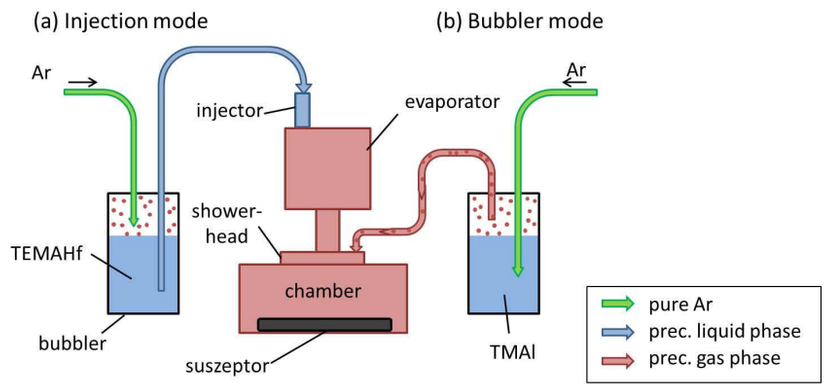

Figure 3.4: Schematic of (a) injection mode and (b) bubbler mode to deliver the precursor to the deposition chamber. In injection mode the precursor stays liquid until it is injected via an injector into the evaporator. In bubbler mode the precursor is directly evaporated in the tank. The precursor transport through the lines is facilitated by Ar purging.

Other precursors (e.g. TMAl in Fig. 3.4 (b)) were transported to the chamber via the bubbler mode. In this case part of the precursor evaporated already in its tank, called bubbler. The amount of gaseous precursor could be controlled by heating the bubbler because the logarithm of the vapor pressure p of the precursor depends on certain material constants a and b and the inverse of the temperature T [43]:

$$log(p) = a - b/T. \tag{3.1}$$

The gaseous precursor was transported to the showerhead and growth chamber by purging Ar through the bubbler. Besides the temperature, the amount of precursor is regulated by the valve opening time just before entering the showerhead.

After this rough overview, the following subsections give more details to the respective CVD processes relevant for this work.

MOVPE

GaN was used here as growth template for epitaxial high-κ oxides and as semiconducting III-V substrate for MOS devices. GaN was deposited on α-Al_2O_3 by MOVPE (also called

MOCVD). As the name suggests the precursors used belong to the metal organic type – $(CH_3)_3Ga$ was used – and one specialty of MOVPE is the epitaxial growth. Typical reactions present in MOVPE are presented in Fig. 3.5. The precursors can already react in the gas phase and they partially decompose close to the substrate due to elevated temperatures. On the substrate surface, where the temperature is typically the highest, the precursor completely decomposes and carbon is removed so that a pure III-V layer can form [42].

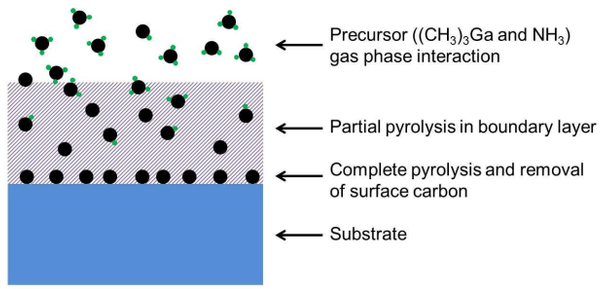

Figure 3.5: Schematic of chemical reactions in MOVPE, adopted from [42].

The GaN used in the presented work was deposited in a horizontal MOVPE reactor (*AIX 200/4 RF S* of *AIXTRON SE*) at temperatures between 500°C and 1100°C. For more details about the growth process see Hardtdegen et al. [44].

ALD

ALD differs from classical CVD not only because the precursor flow is pulsed. While in CVD all precursors decompose and react either in the gas phase or on the substrate, ALD stands out due to self-limiting surface reactions obtained by alternate precursor pulses at low deposition temperatures [45].

ALD growth proceeds in cycles, each cycle consisting of separate pulses of a metal organic and an oxygen precursor, see Fig. 3.6. Each cycle consists of four steps. The cycle starts with the exposition of the sample surface to the metal organic precursor. The precursor molecules react with the OH terminated surface by ligand exchange, Fig. 3.6 (a). These reactions continue until all sites are saturated or until no more reactions can take place due to steric hindering caused by the large size of the precursor molecules [46]. In the next step residual precursor and byproducts are purged out with Ar to prevent reaction with the oxygen precursor, Fig. 3.6 (b). When ozone is purged into the chamber it reacts with the remaining ligands of the Hf precursor at the surface and again a OH terminated surface is created, see Fig. 3.6 (c). Also the ozone pulse lasts until all surface reactions have saturated. Excessive ozone and byproducts are purged out with Ar in the final step of the growth cycle (cf. Fig. 3.6 (d)). To ensure self-limiting growth, which is a basic feature

of ALD, it is important that the surface reactions saturate, thus that the precursor pulse is long enough. That way ALD offers very good control of layer thicknesses. In the ALD processes used here, typically 10 growth cycles are needed to grow 1 nm of oxide. Hence, due to steric hindrance, less than a monolayer of oxide is deposited in one cycle.

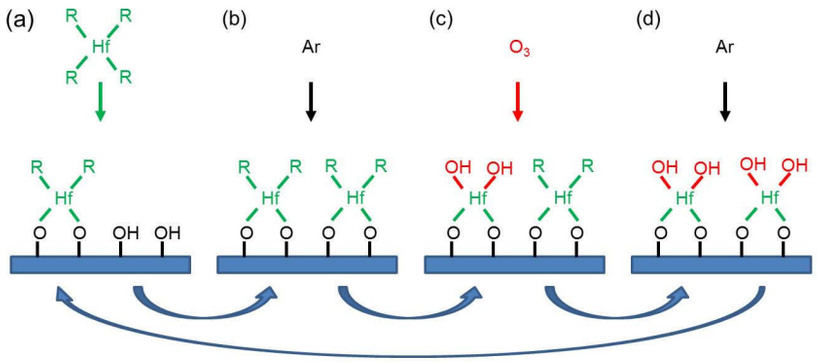

Figure 3.6: Scheme of an ALD growth cycle: (a) TEMAHf and the OH on the surface react by ligand exchange; (b) Residual precursor and byproducts are purged out with Ar; (c) O_3 reacts with the ligands on the surface; (d) a second Ar purge removes byproducts and leaves a OH terminated surface suitable for another growth cycle.

In addition, ALD offers the possibility to deposit conformally even on surfaces with high aspect ratios because of the self-limiting surface reactions. Compared to other CVD growth techniques, the substrate temperature during deposition is rather low [45], in the here presented cases it is always kept at 300°C.

Disadvantages in ALD are the very low growth rate and that even in optimized processes always small amounts of impurities from precursor molecules like carbon are incorporated [45].

The ALD depositions were done in a *Tricent Oxide-ALD* of the company *AIXTRON SE* with a 300 mm recess in a perpendicular-flow reactor with a showerhead design, compare Fig. 3.7. In order to be able to process also samples of the size 20 mm × 20 mm, so-called pocket wafers - 300 mm diameter Si wafers with pockets - were used. These pockets in the size of the samples were realized using mechanical grinding.

Ozone (O_3) dissolved in oxygen was used as oxygen precursor in all ALD processes. To be able to deposit HfO_2 and the various forms of doped HfO_2 the following metal organic precursors were chosen:

- Hf TEMAHf (Tetrakis[Ethyl-Methyl-Amino]-Hafnium) - $Hf[N(CH_3)(CH_2CH_3)]_4$

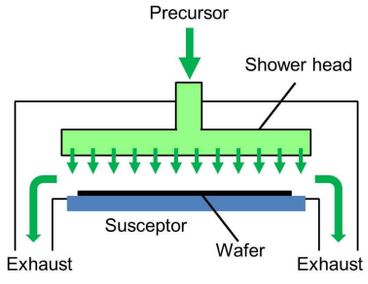

Figure 3.7: Schematic of a perpendicular-flow reactor with a shower-head design, adapted from [45].

- Al TMAl (Trimethyl-Aluminum) - $Al(CH_3)_3$
- La $(iPrCp)_3La$ (Tris[Isopropyl-Cyclopentadienyl]-Lanthanum) - $((C_3H_7)(C_5H_4))_3La$
- Lu famd-Lu (Formamidinate-Lutetium) - $Lu[(NR)_2)CH]_4$ (R = alkyl group)
- Er famd-Er (Formamidinate-Erbium) - $Er[(NR)_2)CH]_4$ (R = alkyl group)

The precursors used for Hf and La were both diluted in octane (C_8H_{18}) and were introduced into the *TriJet*® evaporator by liquid injection. For the metal precursors of Al, Lu and Er the bubbler mode was chosen.

Before the development of the ternary oxide ALD processes it is convenient to first investigate binary oxide processes with the different metal precursors needed. The deposition processes for pure HfO_2 and pure Al_2O_3 were already elaborated. For liquid injection of TEMAHf 10 ms opening time are sufficient for ALD, for evaporation of TMAl at room temperature 1 s opening time is sufficient because TMAl has a high vapor pressure.

Famd-Lu has a rather low vapor pressure and thus the bubbler was heated and the opening times were chosen longer than for TMAl. Deposition rates for test processes of Lu_2O_3 at bubbler temperatures up to 100°C showed zero or negligible amounts of Lu in the film. The amount of Lu determined by RBS (see Subsection 3.2.1) in Lu_2O_3 films deposited at a bubbler temperature of 120°C as a function of precursor opening time is presented in Fig. 3.8 (a). Even for opening times up to 150 s the growth per cycle did not saturate, but increased linearly as a function of opening time, and for an ideal ALD process probably even higher opening times would be needed. Since the purpose of the Lu introduction here was doping, where only small amounts of Lu were necessary, the presented range was considered sufficient for the mixed ALD process presented below keeping in mind that the amount of Lu can be regulated by the opening time for bubbler temperatures of 120°C. For Er_2O_3 deposition the same type of precursor was used and thus similar growth conditions

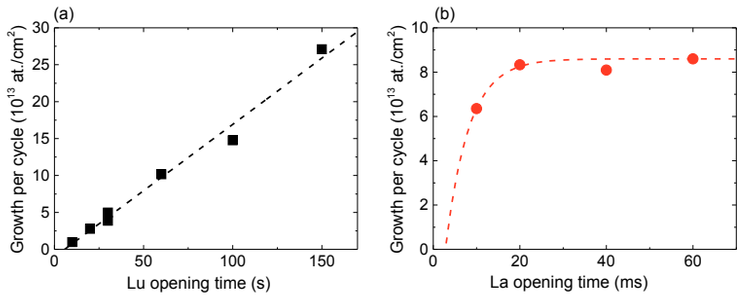

Figure 3.8: Amounts of (a) Lu and (b) La atoms per ALD growth cycle as a function of precursor opening time for Lu_2O_3 and La_2O_3 processes, respectively. Dashed lines are added as guide to the eye.

were expected. Investigations reveal that a slightly higher bubbler temperature of 135°C was needed to reach sufficient deposition rates.

Since the La precursor is injected into the chamber by liquid injection similar opening times are expected as for HfO_2. Different opening times between 10 ms and 60 ms are tested to explore the La_2O_3 deposition. Since La_2O_3 is hygroscopic it is capped in situ with a thin Al_2O_3 layer to be able to take it out of the chamber for RBS investigations. The results are shown in Fig. 3.8 (b). Saturation already sets in for opening times of 20 ms. For lower opening times the amount of La per cycle can be reduced which is beneficial for mixed cycles where small amounts of La are wanted.

In order to dope HfO_2 different approaches were used to extend the ALD process of HfO_2 described above. In the case of Al doping a so-called supercycle process was chosen. A supercycle consisted of n standard HfO_2 cycles and one mixed cycle with successive introduction of TEMAHf, TMAl and O_3. By variation of n the amount of Al could be controlled, while thickness variations were done by changing the total number of supercycles performed in a row. Of course the variation of Al amount and the thickness variation is quantized in this process.

In the case of La doped HfO_2 mixed cycles were used. The Hf precursor injections lasted 10 ms and the La precursor injections started 5 ms deferred and lasted 5 ms. By the differences in start time and opening time the Hf to La ratio could be varied.

As mentioned above, the Er and Lu precursors have low evaporation rates. Hence, again a mixed cycle process was chosen to introduce Lu/Er into HfO_2, but the cycle started with the opening of the Er/Lu precursor line and after 15 s up to 25 s TMAHf was injected on top of it and saturated the remaining substrate surface. The ratio between Lu/Er and Hf was controlled by the opening time of the Lu or Er precursor line.

One has to keep in mind that the here presented mixed cycles deviate from an ideal ALD growth because in ideal ALD the good control of stoichiometry is achieved due to the saturation of the sample surface after precursor injection. When interrupting the Lu

pulse by Hf injection the surface is not yet completely saturated (see Fig. 3.8) and though the precision of this process is degraded compared to the standard HfO_2 process. A big advantage of this approach is that it is tunable in thickness and metal to metal ratio. In comparison, the supercycle approach introduced for Al doped HfO_2 is less flexible. For example changing the ratio n of pure Hf cycles to Al cycles from 2 to 3 changes the Al content from roughly 33% to 25%. Values in between are not possible in this approach, but they are possible in the mixed cycle approach used for La, Lu and Er doping.

AVD®

TiN is a widely used gate metal which proved to be beneficial in MOS devices based on Si and HfO_2 [28]. Also for the case of doped HfO_2 MOSCaps presented here TiN was used as metal gate and was deposited by AVD®. As described above, in AVD® the metal organic precursor is pulsed like in ALD depositions but the nitrogen precursor is purged into the growth chamber continuously. Hence, AVD® properties lie in between typical ALD and CVD properties: AVD® is faster than ALD processes and shows better conformity than classical CVD [47].

The depositions were done in a *Tricent Nitride-AVD®* of the company *AIXTRON SE* with a showerhead reactor and the Ti precursor (TDEATi (Tetrakis (Diethylamido) Titanium) - $[N(C_2H_5)_2]_4Ti$ diluted in octane) was injected via liquid injection into a *TriJet®* evaporator. Other gases present during growth, which served as nitrogen source and carrier gas, were NH_3, H_2 and N_2. The susceptor, onto which the samples were placed, was kept at 420°C. Again pocket wafers were introduced to be able to process smaller samples.

3.1.3 PVD techniques

In the case of epitaxial oxides and for contacts, physical vapor deposition (PVD) techniques were used, namely pulsed laser deposition (PLD) and electron beam evaporation (EBE).

PLD

Pulsed laser deposition was used to deposit $GdScO_3$ and $LaLuO_3$ epitaxially. In a vacuum chamber a pulsed, highly energetic laser is focused on a rotating target and for a sufficient laser energy density the target material is heated until it evaporates. For even higher energies the target material ionizes and forms a plasma. These ions are adsorbed on the sample surface building up a thin film [48], compare Fig. 3.9.

Epitaxial growth is enabled by heating the sample with a SiC heater.

In the presented work a KrF excimer laser with a wave length of 248 nm, a pulse width of 20 ns and a fluence of ca. 5 J/cm^2 at a repetition rate of 10 Hz was used. The $LaLuO_3$ and $GdScO_3$ targets were produced of powders of 99.99 % La_2O_3, Lu_2O_3, Gd_2O_3 and Sc_2O_3. The powders were mixed, ball milled in isopropanol for 24 h, calcined at 1300°C for 24 h, pressed into 25 mm diameter targets and finally sintered at 1500°C for 12 h. The oxide depositions were done in an oxygen ambient with an oxygen partial pressure $\geq 10^{-3}$ mbar.

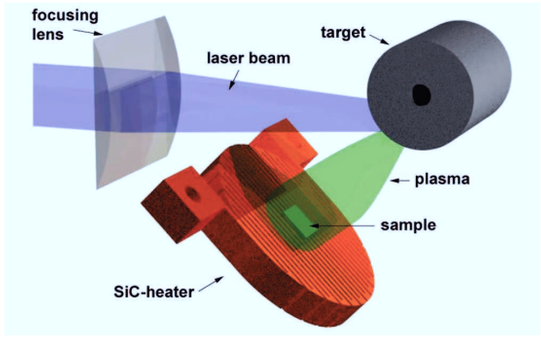

Figure 3.9: Schematic of pulsed laser deposition: A laser beam heats up the rotating target which evaporates, ionizes and forms a plasma. The plasma hits the sample which is positioned on a SiC heater and the target material is adsorbed on the sample surface and forms a thin film. After [48].

Substrate temperatures ranged between room temperature and 900°C. The temperatures were controlled by the heating current which was calibrated for Si substrates. Due to variation in sample size and substrate material slight deviations in temperature might have occurred and hence the temperature values given here should be regarded as approximate values.

Electron beam evaporation

Al contacts were deposited via shadow masks using electron beam evaporation. The electron beam was created in a thermionic-emitting filament at voltages around 10 kV and at currents of 50 mA up to 150 mA and was then directed onto the Al target by a magnetic field [49]. The Al heated up and vaporized and part of the evaporated atoms were adsorbed at the surface of the samples forming the Al layer. The crucible holding the Al target was water cooled. The evaporation was performed in vacuum.

The evaporator used here was a *Leybold Univex 450*. The layer thickness was controlled using an *Inficon* quartz crystal microbalance.

3.1.4 Reactive ion etching

After the deposition of Al contacts via shadow masks, in the case of Hf based MOSCaps the TiN in between the contacts has to be etched to isolate the contacts electrically from each other, compare Fig. 3.1 (d). RIE is chosen here because compared to chemical etching it can etch rather anisotropically and results in steep edges. In a reactive ion etcher the samples are placed on a cathode which is capacitively coupled to an rf (radio frequency) generator while the anode is grounded. Free electrons which are accelerated in the electric field collide with gas molecules, ionize them and initiate a plasma. Ions and reactive neutral

radicals bombard the surface almost normally and etch the TiN [20].

Etching is done in an *Oxford Plasmalab 100* using SF_6 and Ar (with a ratio of 3:1) at a pressure of 10^{-3} mbar and at around 80 W for 30 - 180 seconds or alternatively in an *Oxford AMDR Dual* RIE chamber.

3.1.5 Rapid thermal annealing

Annealing processes with short heating and cooling times - called rapid thermal annealing (RTA) or rapid thermal process (RTP) - were used at different steps of the doped HfO_2 MOSCaps process to improve the CV characteristics.

All HfO_2 based MOSCaps underwent a forming gas annealing (FGA), a special kind of RTP, at 400°C for 10 minutes. The gas atmosphere during the FGA consisted of 4 % H_2 and 96 % N_2. During FGA the hydrogen diffuses into the gate stack and saturates dangling bonds at the interface between Si and the high-κ oxide, compare Section 2.7.1. This includes the saturation of mobile charges or interfacial traps and CV characteristic are hereby improved.

Some of the investigated doped oxides were also treated by an RTP process directly after oxide deposition referred to as post deposition anneal (PDA) in order to encourage the transition from an amorphous to a polycrystalline phase. The PDA was done in an Ar atmosphere for 30 seconds at temperatures between 600°C and 1000°C. Even though the term PDA can be used rather widely, for convenience, in the present work the term PDA is only employed for annealing processes in Ar directly after oxide deposition.

Both types of annealing processes (FGA and PDA) were done in a *Mattson Helios*® double chamber system for 300 mm wafers using pocket wafers.

To alloy Al or In contacts on top of the oxides on GaN used for Hall measurements, the samples were annealed in an N_2 ambient at 580°C for at least 170 s or at 400°C for at least 120 s, respectively. The annealing was employed in an *ADDAX RM V4/24*.

3.2 Characterization methods

The characterization includes the structural determination of the thickness, stoichiometry, crystal order and crystallinity and the electrical characterization (permittivity, band gap, leakage currents, breakdown electric fields) of the deposited oxides and in one single case the mobility of the substrate. Methods used to do such characterization are presented in the following sections.

3.2.1 Structural characterization

Rutherford backscattering spectrometry

Stoichiometry, thickness and crystal order of the deposited oxide layers were determined by Rutherford backscattering spectrometry (RBS).

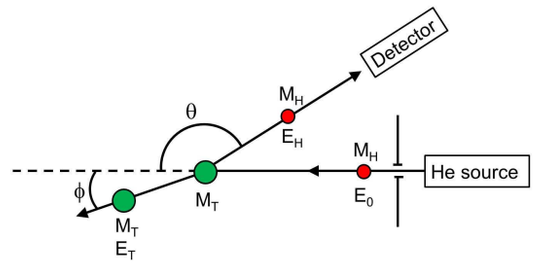

Figure 3.10: Schematic of beam geometry during RBS. The incident He ion with mass M_1 is scattered at the target atom with mass M_2 and is then detected at the scattering angle θ while the target atom moves in the direction defined by the recoil angle ϕ [50].

During RBS He^+ ions are scattered in a material to determine its elemental composition and distribution. Incident He^+ ions collide with target atoms in the sample and transfer energy to them due to Coulomb scattering. In these elastic collisions the principles of conservation of energy and impulse are valid and the energy of the scattered He^+ ion E_H is completely determined by the masses of the He^+ M_H, the mass of the target atom M_T, the scattering angle θ and the energy of the incident He^+ E_0 (see Fig. 3.10) [50]:

$$E_H = E_0 \times \left[\frac{(M_T^2 - M_H^2 sin^2\theta)^{1/2} + M_H cos\theta}{M_T + M_H} \right]^2 . \tag{3.2}$$

The higher the mass of the target atom M_T is, the higher is the measured energy of the scattered He^+ ion E_H for a fixed scattering angle θ and thus different atomic elements can be differentiated in the RBS spectra.

If the incident He^+ ion penetrates deeper into the target material it does not only loose energy due to Coulomb scattering with a certain target atom but also smaller energy amounts due to small-angle scattering [50]. Hence, target atoms positioned deeper in the material result in lower energy in the measured spectrum than target atoms of the same element at the surface. This characteristic offers the possibility to determine the thickness of a certain layer by RBS.

Typically the scattering angle θ is fixed at 170° and the sample is rotated around its normal during measurement. This is called random mode. Additionally measurements in the so called channeling mode are possible. During channeling the lattice planes of a crystal are oriented in that way, that the incident beam is almost parallel to the crystal planes. In this case small-angle scattering dominates, the He^+ ions penetrate deep into the sample and the detected intensities are drastically reduced [50]. However, defects and interfaces interrupt this channeling effect, induce Coulomb scattering and enhance the measured signal. That is why the ratio of the channeling signal to the random signal gives insight into the crystal order of the target material. Lower minimum yield (the minimum ratio

between channeling and random signal) means higher crystallinity for a given material system.

The incident He^+ ions used had an energy of 1.4 MeV. The detector was a surface-barrier solid-state nuclear-particle detector which detects the number of electron-hole pairs created in the depletion region of a reversed-biased Schottky barrier diode due to the scattered He^+ ions [50].

The measured data were analyzed deploying the software *RUMP* [51].

Secondary ion mass spectrometry

Besides RBS, also time of flight (TOF) - secondary ion mass spectrometry (SIMS) was used to determine the atomic ratios of elements in the oxide layers. SIMS is an analytical technique where the surface is bombarded with primary ions and where the charge and mass of secondary ions which are ejected from the surface due to the bombardment are detected [52].

When the primary ions with energies in the keV range hit the sample surface a cascade of collisions is generated within the sample. Only some of the ions involved in this cascade leave the sample and are detected either as single ions or as molecular ions. The energies of the secondary ions is rather low in the range of tens of eV. Most of the incident energy is lost due to collisions [52].

TOF refers to the type of mass spectrometer analyzer used for the SIMS setup. In TOF-SIMS the primary ions are pulsed and the secondary ions are accelerated by an electric field. The acceleration depends on the ion mass (lighter ions reach the detector first) and therefore the ion mass can be deduced from the flight time of the ion from the sample to the detector [52].

In depth information can be achieved ablating the material stepwise by sputtering and repeating the SIMS profiling after each step.

The measurements presented in this work were performed with a TOF-SIMS of *ION-TOF* using Bi_3^+ as primary ion source at an energy of 25 keV and sputtering the material for depth profiling was done with Cs^+ ions at 1 keV.

Atomic Force Microscopy

Atomic Force Microscopy (AFM) was used to scan the surface of samples and to derive an image of the surface morphology. This way the smoothness of the surface could be judged.

During AFM an oscillating cantilever with a very narrow tip screens at very low distance over the surface (see Fig. 3.11) and the force between the tip and the surface deforming the cantilever is typically measured by the displacement of the reflection of a laser beam focused on the cantilever. If the tip gets closer to the sample surface, the oscillations behavior changes due to increased van-der Waals forces. Typically a feedback loop is used to maintain free oscillations and therefore to keep the tip at a constant distance to the surface. The movement of the tip can be regulated by piezo elements [53]. The height

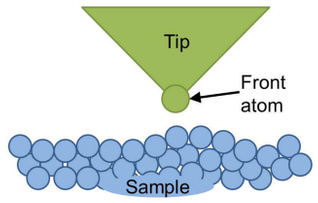

Figure 3.11: Schematic of on AFM tip scanning over a sample surface, after [53]. The tip is kept at constant height by a piezoelectric drive.

positions of the cantilever are used to build the AFM image and hence a height profile of the surface. Averaging over such a height profile yields the surface roughness.

The AFM measurements presented in this work were conducted with a commercial *Digital Instruments Nanoscope IIIa AFM* in tapping mode.

X-ray diffraction and reflectivity

Elastically scattered x-rays can be used to characterize crystals, polycrystalline films or even amorphous films. The incident monochromatic x-rays scatter at different lattice planes or even at surfaces and interfaces and in cases of constructive interference a high intensity is measured at the detector. X-ray diffraction (XRD) is used to characterize crystals respective lattice constants, lattice type and crystallinity. Glancing incidence XRD (GIXRD) is a special form of XRD used to investigate polycrystalline films or powders. X-ray reflectivity (XRR) is used to determine film thicknesses and roughnesses.

The angular intensity distribution in XRD and XRR is based on Bragg's law for constructive interference:

$$2\ d\ sin\theta = n\ \lambda \tag{3.3}$$

with d the spacing between lattice planes or interfaces, θ the angle of the incident and reflected beam respective these planes, n an integer and λ the wave length of the monochromatic x-ray [50, 52].

In crystals different lattice plane spacings $d = d_{hkl}$ are detectable depending on the lattice type and orientation of the crystal. They can be uniquely described by the Miller indexes (hkl), compare Section 2.1.

The intensity of a reflection, when the Bragg condition is fulfilled, depends on the so called structure factor F_{hkl} which means it depends on the elements present in the crystal and their respective positions in the lattice [50]. In some cases the intensity may equal zero and hence no reflection is visible. The positions and intensities of the reflections can be regarded as the fingerprint of a certain polymorphic phase of a material and so both are used to identify structures by XRD.

Fig. 3.12 explains the different angles used in XRD: ω is the angle of the incident beam relative to the sample surface, 2θ is the angle of the reflected beam relative to the direction

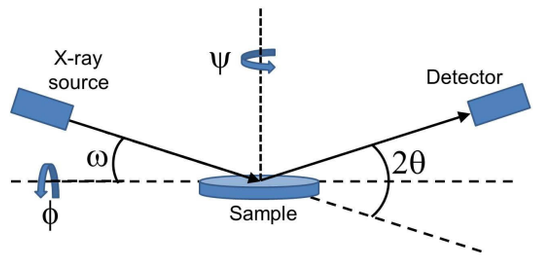

Figure 3.12: .Schematic of the angles in XRD using a four-circle diffractometer: ω is the incident angle of the incident beam relative to the sample surface, 2θ describes the angle of the reflected beam hitting the detector relative to the incident beam direction, ψ defines the rotation around the normal of the sample surface and ϕ specifies the tilt of the sample.

of the incident beam, ψ is the rotational angle around the sample surface normal and ϕ describes the tilting of the sample surface.

XRD

X-ray diffraction was used here to analyze the structure of epitaxial films. The key type of measurement was the θ-2θ scan in the out of plane direction. ω and 2θ are varied in that way, that the condition $\omega = 2\theta$ is always fulfilled. The measured intensity is plotted against 2θ and the detected reflections (following Bragg's law) reveal lattice distances of planes parallel to the surface [52]. The sample can also be tilted in that way that the Bragg condition is true for other lattice planes not parallel to the surface and the $\theta - 2\theta$ scan can be repeated to find the respective lattice plane spacings.

If two or more reflections were found in a $\theta - 2\theta$ scan, a method introduced by Nelson and Riley [54] was used to determine the lattice plane distance. Thus errors occurring due to slight misalignment of the set up could be eliminated.

After identifying such reflections from lattice planes not parallel to the surface, ω and 2θ can be fixed to the positions of such a reflection and a ψ scan, i.e. rotation around the surface normal [52], gives information about symmetry conditions in the crystal. E.g. a threefold symmetry (reflections with the same intensity every 120°) is an evidence of a cubic structure or a sixfold symmetry can either be caused by a hexagonal structure or by twinned cubic structures. (In the second case the same intensity for all six reflections is only true if both twins are equally common).

Rocking curve scans were used to estimate the crystallinity of the epitaxial films. In this case ω was varied, but 2θ was kept constant. The variation of ω was done 1°-3° around the position of one of the measured reflections in the θ-2θ scan. For a perfect crystal there is one sharp peak at $\omega = 2\theta$, the minimum width of this peak is limited by the resolution

of the setup. For a polycrystalline film without texture the intensity would be constant. In typical epitaxial films broadened peaks are observed due to imperfections in the crystal such as misfit dislocations or strain effects at the interface. Hence, the full width half maximum ($FWHM$) of the peak is used as a degree of crystallinity.

In one case the Si substrate and oxide peak could not be distinguished using a standard XRD θ-2θ scan in the out of plane direction (compare Section 5.4.2) because the out of plane lattice spacings were the same. In that case it was made use of the assumption that the oxide film has lower crystallinity than the quasi perfect Si underneath. First an XRD θ-2θ scan was carried out with the Si lattice planes aligned. The Si reflection dominated the diffraction pattern. Than the sample was tilted around ω by 0.3° and the θ-2θ scan was repeated. Under this condition the Si reflection was not visible any more since the rocking curve width is below 0.3°. Yet the oxide peak was visible because its crystallinity was degraded compared to Si. Hence, by a slight tilt an oxide reflection at the same angle as the substrate peak could be made visible.

GIXRD

Grazing incidence XRD (GIXRD), also called glancing incidence XRD, was used to characterize polycrystalline films. In GIXRD the incident beam angle ω is fixed at a low angle (0.2°-3°) to cover a big area of the sample but only a shallow depth and only 2θ is varied. This measurement type resembles the $\theta - 2\theta$ scans used for epitaxial films, but probes various crystallographic directions of the crystallites since these are oriented randomly in the film. The intensity of the measured peaks is much lower compared to the ones known from $\theta - 2\theta$ scans on a crystal because only a fraction of the irradiated volume contributes to the reflection, but therefore all different lattice plane spacings can be detected in one single scan and high intensity substrate peaks are omitted [52].

Intensity and width of the diffraction peaks depend on the grain size, as described by the Scherrer equation [55]:

$$FWHM = 2\sqrt{\frac{ln2}{\pi}} \cdot \frac{\lambda}{d} \cdot \frac{1}{cos\theta} \tag{3.4}$$

where $FWHM$ the full width half maximum of the measured peak, λ the wavelength of the x-ray and d the diameter of the grain.

XRR

X-ray reflectivity (XRR), also called x-ray reflectometry, can be used to determine thickness, density and roughness of thin films. Experimentally a $\theta - 2\theta$ scan at very low angles (0.1° - 10°) in the out of plane direction is executed. But other than in XRD, where the scattering of atoms in an ordered crystalline film is measured, the scattering at the surface and at interfaces is employed. Also for distances between surfaces and interfaces the Bragg condition is valid. But the Bragg condition is fulfilled at much lower angles θ in this case because the layer thicknesses are considerably larger than the interatomic distances in a crystal. The positions of the intensity maxima in an XRR scan are hence given by the

film thickness. The amplitude of the reflections is impacted by the difference between the density of the film in relation to the density of the substrate. The roughness of the film determines the steepness of the first decay in the XRR curve [52]. For XRR thickness evaluations the intensity is typically plotted as a function of scattering vector q:

$$q = \frac{4\pi}{\lambda} sin\theta \tag{3.5}$$

where λ the x-ray wavelength [52].

XRD and XRR measurements executed during this work were conducted on a *Philips X'Pert* four-circle diffractometer with a copper K_α x-ray tube. Cu K_α has a wavelength of 0.15418 nm which is smaller than the lattice plane distances which is a requirement for diffraction [50]. For GIXRD typically an incidence angle ω of 2° was chosen.

Peak positions in XRD scans were analyzed using the programs *XRDC* [56] and *PowderCell* [57]; XRR measurements were analyzed employing the software *plot.py* [58].

Transmission electron microscopy

Transmission electron microscopy offers an effective tool to create images of a layered system on the atomic scale. Here it is used to control layer thicknesses and roughnesses and to evaluate the crystal structure of the layers. For TEM imaging an electron beam is focused on a very thin slice (<200 nm) of the sample, called specimen. The electrons can simply transmit through the specimen or can undergo elastic or inelastic scattering. Due to interaction secondary electrons, backscattered electrons, Auger electrons, photons and electron-hole pairs inside the specimen are generated and some of these effects can be used for TEM imaging [52].

Depending on the lenses and apertures used for the incident and diffracted beams either a direct image of the specimen or a diffraction pattern representing the reciprocal space is generated. The direct image can be used to identify layer thickness, surface roughness and defects in the crystalline layers. Further, amongst other parameters, atomic masses and strain have influence on the contrast and therefore also statements on mass distributions and strain can be made. Nevertheless, when interpreting the images one has to be sure that damages occurring due to the specimen preparation and artifacts in the image for example due to a slight defocus are not confused with effects resulting from the sample itself.

The electron diffraction patterns of crystals provide information about lattice symmetry and lattice spacings. The visible spots correlate to the reciprocal lattice of the structure. In the case of polycrystalline films diffraction rings instead of specific spots are visible and their radii correspond to the inverses of the various lattice plane distances found in the crystallites.

The specimen used should be as thin as possible without any damages that would alter the properties of the layers (such as an amorphization of a crystalline zone).

Different preparation techniques were used in this work to prepare appropriate specimens. In the first approach the specimen were cut using a focused ion beam (FIB) of Ga

ions using a *Helios Nanolab DualBeam FIB* and afterwards thinned down in a *NanoMill® TEM specimen preparation system* ion mill. This technique typically induced damage to the specimen.

Hence, mostly the second preparation technique was chosen: grinding with an abrasive paper to prepare wedge shaped specimens using a *MultiPrep™* polishing system from *Applied High Tech*.

The TEM images in this work were accomplished in cooperation with the Ernst-Ruska-Center at the Forschungszentrum Jülich GmbH and more details to TEM preparation, imaging and results can be found in the master thesis of Fabian Wendt [59].

X-ray photoelectron spectroscopy

X-ray photoelectron spectroscopy (XPS) is a method to analyze the surface of a material and in this work XPS is used to determine the band gap of oxides. In XPS a beam of incident photons with energy hν (ν is the photon frequency, h the Planck constant) is absorbed by atoms in the sample and following the photoelectric effect photoelectrons are emitted with kinetic energy E_k. The kinetic energies that can be measured in a spectrometer equal to:

$$E_k = h\nu - E_B - \Phi. \tag{3.6}$$

Here E_B refers to the binding energy of the electron in the sample and Φ describes the work function of the spectrometer, which is a set-up dependent value which has to be calibrated once [52].

Typically the binding energy E_B is plotted as a function of detector counts to be able to correlate the measured energies directly to the core levels from which the photoelectrons originate.

Some of the photoelectrons can loose energy due to scattering generating plasmons and band-to-band excitations [52]. The effect of loosing kinetic energy due to band-to-band excitations is used in the method of Miyazaki to determine the band gap. Therefore the O 1s peak of the epitaxial oxides investigated here was measured with high accuracy and the position of the core-line O 1s peak was compared to the onset of band-to-band excitations. The energy difference equals the band gap of the oxide [60]. The onset of the excitations in the spectrum was defined as the intercept of the background and the linear extrapolation of the band-to-band excitations, compare Fig. 5.38.

XPS measurements presented in this work were executed using a *PHI Versa Probe II* system with a monochromatic Al K_α x-ray source. The electron take off angle was fixed to 45° and the analyzer pass energy was adjusted to 11.75 eV which resulted in an energy resolution of approximately 0.2 eV.

Before the measurements the samples were etched by Ar at 2 kV for two minutes to remove surface contamination like carbon. No impact on the sample characteristics were expected due to sputtering because the signals spectra of the oxides O 1s peak were unchanged after sputtering.

Ellipsometry

Also ellipsometry was used to determine the band gap of oxide thin films. During an ellipsometric measurement monochromatic light with known polarization is directed to a sample surface and a detector measures the change in polarization state of the reflected light [52].

Change in polarization means the ratio ρ between the complex reflection coefficients with polarization parallel R_p and perpendicular R_s to the plane defined by the incident and reflected beams. ρ can be expressed in the two ellipsometric parameters Ψ, the amplitude, and Δ, the phase of ρ, compare [52]:

$$\rho = \frac{R_p}{R_s} = tan\Psi e^{i\Delta}. \tag{3.7}$$

The change in polarization is determined by the complex dielectric function of the oxide. In many cases a direct analytical analysis of the data is not possible, so a model-based regression analysis is used. Therefor a response is calculated based on a model and compared to the measurements.

The model consisted of a layered structure (compare Fig. 3.13) and the thickness and optical constants for each layer were either known from XRR or determined by modeling.

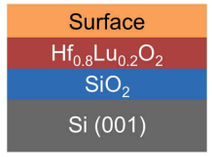

Figure 3.13: Model of stacked layer system for ellipsometry analysis.

The model was optimized so that the calculated response from the model and the measurement fitted best. A measure for the quality of the fitting is given by the Mean Squared Error (MSE): the lower the MSE the better the fit.

$$MSE = \frac{1}{2N-m}\sum_{i=1}^{N}\left[\left(\frac{\Psi_i^{mod}-\Psi_i^{exp}}{\sigma_{\Psi,i}^{exp}}\right)^2+\left(\frac{\Delta_i^{mod}-\Delta_i^{exp}}{\sigma_{\Delta,i}^{exp}}\right)^2\right] \tag{3.8}$$

where N is the number of (Ψ, Δ) pairs, M is the number of variable parameters in the model and σ^{exp} are the standard deviations on the experimental data points [61].

The real and imaginary parts of the refractive index, n and k, were taken from the best fitting model and then used to evaluate the band gap.

The ellipsometry measurements presented here were performed in cooperation with the *Institute of Physical Chemistry "Ilie Murgulesu" of the Romanian Academy*. A *Rotating Analyzer Ellipsometer (RAE)* configuration of *J.A. Woollam Co. Inc. USA* was used

covering a spectral range of 200 nm up to 1000 nm. The incident angle was fixed to 70° and all measurements were performed in air and at room temperature.

The data were analyzed using the software *WVASE32*® [62].

3.2.2 Dielectric characterization

Capacitance voltage measurements

As presented in Section 2.7 capacitance voltage (CV) measurements on MOSCaps were used to determine the relative permittivity of the investigated high-κ oxides. Even though finding the permittivity is the main purpose of CV measurements in this work, many other properties like trap densities, work functions and doping profiles in the substrate can be investigated analyzing CV curves [34].

Two probe needles were used to contact the MOSCaps for CV measurements. The high potential needle touched one of the small area ($< 3 \times 10^{-4}\,\mathrm{cm}^2$) Al pads, the low potential needle built up a connection to a big area ($> 6 \times 10^{-2}\,\mathrm{cm}^2$) contact. The capacitance and resistance of the big area contact can be neglected compared to the ones of the small area contacts, compare Fig. 3.14. The resistance depends reciprocally on the area and resistances in a row are added to evaluate the total resistance, hence the small resistance of the big area capacitor can be neglected; the capacitance is proportional to the contact area and capacitances in a row add up reciprocally, hence the big capacitance of the big area contact can be neglected, too.

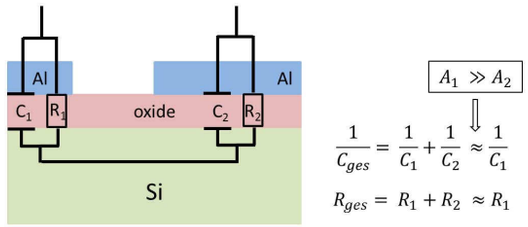

Figure 3.14: Schematic of capacitances and resistances during CV measurements. The approximations are based on the fact that the area A_1 underneath the first contact (R_1, C_1) is much smaller than the area A_2 underneath the second contact (R_2, C_2).

During CV measurements a DC voltage V_g and a small sinusoidal signal V_{ac} (5 mV) with frequency ω (typically 100 kHz) were applied between the needles and the capacitive current I_{cap} was measured. The capacitance C was calculated from the relation $I_{cap}/V_{ac} = \omega C$ [63]. The CV measurements were carried out with an impedance analyzer *HP 4192A LF* from *Agilent Technologies*. The normalized capacitance (capacitance per contact area) was then plotted as a function of DC voltage V_g to analyze the measurement. Additionally, the conductance as a function of V_g was plotted to evaluate the density of interfacial traps

and eventually leakage effects.

The measurements were repeated for different small Al pads and the extracted capacitances per area were averaged over 4 - 8 measured values.

Current voltage measurements

Current voltage measurements were executed to determine leakage currents and breakdown electric fields. A DC voltage was applied either between a big area contact and a small area contact (like for CV) or between two small area contacts and the resulting current was detected. To be able to measure very low current densities a semiconductor characterization system *4200-SCS* from *Keithley Instruments Germany* and a semiconductor parameter analyzer *HP4155* from *Agilent Technologies* were used.

3.2.3 Characterization of GaN influenced by hexagonal $LaLuO_3$ top layer

In an excursus at the end of Chapter 5 the influence of hexagonal $LaLuO_3$ on the underlying GaN is shortly evaluated. Therefore, photoluminescence and Hall measurements were carried out.

Photoluminescence

Photoluminescence describes the emission of light from excited electronic states after absorption of light [64]. If the photon energy of the incoming light is high enough, it can excite electrons from the valence band to the conduction band creating a highly mobile electron in the conduction band and a hole in the valence band. When they recombine the nascent energy can either create phonons or photons or both. The spectra of the emitted light gives information about the different transitions in the material.

In this study $LaLuO_3$ on GaN was investigated. Because the band gap of $LaLuO_3$ was larger than the energy of the incident beam, no interaction with the $LaLuO_3$ was expected. Thus, the measured spectra gave information about the GaN transition energies.

In Micro-photoluminescence (μ-PL) a laser beam with a spot size in the micrometer range is focused on a sample and the emitted PL intensity is detected as a function of wavelength, i.e. photon energy.

Here, micro-photoluminescence measurements were carried out at room temperature to explore the effects of $LaLuO_3$ on GaN. As excitation source a continuous wave He-Cd laser (wave length 325 nm) was provided with a spot size of $\approx 1\,\mu$m. The laser light was focused by a $100\times$ UV objective offering a lateral resolution of $\approx 0.5\,\mu$m. The light emitted from the sample was analyzed using a *RENISHAW* spectrometer.

Hall mobility measurements

The Hall effect was used to determine the mobility μ and the carrier concentration n of a semiconducting material. The set up is shown in Fig. 3.15.

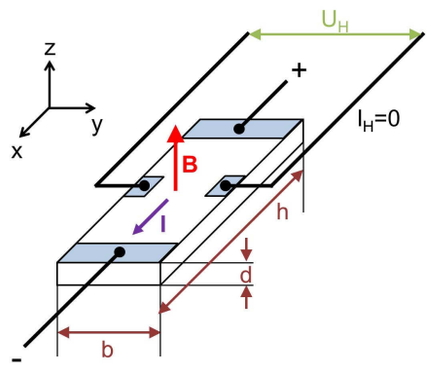

Figure 3.15: Schematic of a Hall effect measurement after [13]. A current I and a magnetic field B are applied along the x- and z-direction, respectively. The Hall voltage U_H along the y-axis is measured [13].

The mobility μ can be extracted from the measured Hall-voltage U_H, the applied voltage U and the applied magnetic field B and from the dimensions of the sample, here in the case of an n-type semiconductor [13]:

$$\mu = \frac{U_H}{UB}\frac{h}{b}. \tag{3.9}$$

Furthermore the Hall constant R_H and the charge carrier density n can be determined when measuring the conductivity σ of the semiconducting films and using the relations $R_H = -1/ne$ and $\sigma = ne\mu$.

Hall measurements were employed to measure the Hall mobility of GaN with a $LaLuO_3$ layer on top and were executed on a *Bio-Rad Hall-System*.

4 Doped HfO_2, a "higher κ oxide" for Si technology

In recent CMOS technology HfO_2 is used as gate dielectric. Amorphous HfO_2 was introduced into industrial chip production in 2008 due to its high relative permittivity κ of about 20, its high band gap above 5 eV and its thermal stability on Si [1]. To continue device scaling in the future, amongst other requirements, even 'higher κ' materials are needed. Doped HfO_2 layers present promising candidates as short-term solutions: on the one hand the introduction of a dopant into the oxide during the ALD growth process should be easy to realize with a suitable precursor. On the other hand various experiments and theoretical calculations have already demonstrated the impact of doping to increase the permittivity without any degradation of the structural or insulating properties [65–74].

In this chapter the doping of HfO_2 with Al, Lu, La and Er is investigated to test the suitability of doped HfO_2 as gate dielectric. The focus is put on the enhancement of the permittivity, but it is also investigated whether the doping has negative impact on other MOS characteristics.

In the first part parameters are discussed that influence the dielectric properties of HfO_2 to motivate the experiments presented later on.

In the following different ALD processes to dope HfO_2 are presented with the aim to maximize the permittivity. Crucial parameters were the doping element, doping content and annealing processes. After optimizing the processes for Al and Lu doped HfO_2, also La and Er were considered as doping elements. Capacitance voltage measurements and CET plots were used to determine the density of interfacial traps and the permittivity.

Leakage current measurements and ellipsometric measurements to estimate the band gap of Lu doped HfO_2 were executed to assure that the insulating properties of the oxides were not deteriorated after doping.

XRD and TEM analysis were employed to explore the roughness of interfaces and surfaces and to identify the structure of the doped oxides.

In the discussion at the end the relation between doping, crystal structure and permittivity is discussed on the basis of the presented measurements.

4.1 Parameters influencing HfO_2 phase

The aim of doping is to enhance the relative permittivity of HfO_2 by promoting a phase transition to a higher κ phase of HfO_2. At room temperature and atmospheric pressure pure bulk HfO_2 is usually either amorphous or monoclinic [79]. The two phases show

Phase	Space group	a	b	c	β (°)
Cubic [75]	$Fm\bar{3}m$ (225)	0.5115			
Tetragonal [76]	$P4_2/nmc$ (137)	0.3578		0.5200	
Monoclinic [77]	$P2_1/c$ (14)	0.5113	0.5172	0.5295	99.18
Orthorhombic [78]	$Pbcm$ (57)	0.5007	0.5228	0.5058	

Table 4.1: Phase, space group and lattice constant of different HfO_2 polymorphs.

permittivities of 12-25 [80–82], see also Tab 4.3. At high temperatures of 1700°C and 2800°C the tetragonal and the cubic phase stabilize, respectively [79]. At high pressures, above 10 GPa, HfO_2 is transformed into an orthorhombic crystal [83]. The unit cells of the four crystalline phases are depicted in Fig. 4.1 and the corresponding lattice constants are summarized in Tab. 4.1. The four phases are related to each other. The cubic phase is, of course, the one with the highest symmetry. It has a fluorite structure (space group $Fm\bar{3}m$), the Hf ions build a face-centered cubic structure and the oxygen ions occupy the tetrahedral interstitial sites [84]. The tetragonal phase (space group $P4_2/nmc$) is a distortion of the cubic structure pushing pairs of oxygen ions alternately up and down along z and by applying tetragonal strain [84]. Also the monoclinic structure can be regarded as a distorted form of the cubic structure [85].

The relative permittivities of the four crystalline phases of HfO_2 were estimated by various groups by first principle calculations or other theoretical calculations, compare Tab. 4.2. They do not only show the medium permittivity, but all diagonal elements of the dielectric tensor. Further no symmetry approximations have to be made as in the Clausius-Mossotti equation (2.8). The calculated values clearly show the anisotropy of the permittivity for asymmetric crystals like tetragonal HfO_2. However, one can also see, that these detailed calculations do not give a clear prediction of the permittivity because in the case of tetragonal HfO_2 different approaches result in quite different κ-values between 24 and 70.

Nevertheless the tendency of cubic and tetragonal HfO_2 having higher κ than monoclinic HfO_2 is always present. Hence, a lot of efforts have been made to transform HfO_2 into these 'higher-κ' phases.

Also the experimentally found values for HfO_2 vary depending on phase and deposition method, compare Tab. 4.3. Most experiments have been done on amorphous or monoclinic HfO_2 because these are the stable bulk phases at ambient pressure and room temperature. Kim et al. report on measurements on a mixed phase of monoclinic and tetragonal HfO_2 deposited by metal organic molecular beam epitaxy [90] and Schlom et al. demonstrated results on cubic HfO_2 though this form was stabilized by Y_2O_3 and thus should rather be classified as doped oxide [11]. In both cases the permittivities reach values of 22 and thus

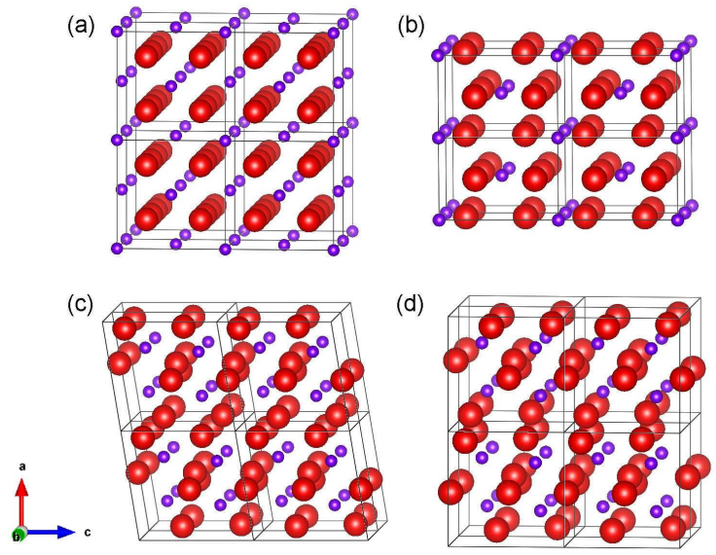

Figure 4.1: Sketch of different HfO_2 polymorphs: 8 unit cells of (a) cubic, (b) tetragonal, (c) monoclinic and (d) orthorhombic HfO_2. Drawings prepared using *VESTA* [86] and with the crystal data from [75–78]

	κ_{xx}	κ_{yy}	κ_{zz}	$\kappa_{avg.}$	Ref.
Monoclinic	18	16	13	16	[80]
	20	18	15	18	[87]
	18	16	12	15	[88]
				18	[89]
Cubic	29	29	29	29	[80]
	28	28	28	28	[88]
				26	[84]
Tetragonal	97	97	16	70	[80]
	41	41	19	34	[89]
	20	20	33	24	[84]
Amorphous				25	[4]

Table 4.2: Diagonal elements $\kappa_{xx/yy/zz}$ and medium values $\kappa_{avg.}$ of HfO_2 permittivity tensors derived from theoretical calculations.

Phase	κ	Deposition technique	Lit.
Amorphous	21	EBE	[8]
Crystalline	19	MOCVD	[91]
Monoclinic	11-14	ALD	[92]
Monoclinic	12-16	ALD	[93]
Monoclinic	22-25	CVD	[94]
Monocl./tetra.	20-22	MOMBE	[90]
Cubic (15% Y_2O_3)	22	single crystal	[11]

Table 4.3: Experimental values for HfO_2 films or bulk crystals. EBE - electron beam evaporation, MOCVD - metal organic chemical vapor deposition, MOMBE - metal organic molecular beam epitaxy.

do not show a great enhancement of κ, yet.

Among the parameters having influence on the stable phase are the material dimensions, e.g. the differences between bulk crystals and thin crystalline films. Due to surface and interface energies thin films and polycrystalline films might by stable in a different polymorph than the bulk form of the same material. Hence a phase change to a higher κ phase can occur in thin and/or polycrystalline films.

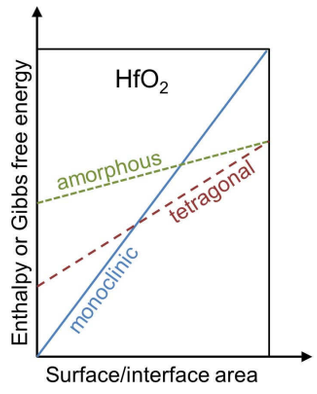

Figure 4.2: Schematic energy map for HfO_2: Gibbs free energy versus surface or interface area for various HfO_2 polymorphs, adapted from [85].

Navrotsky et al. examined the Gibbs free energy as a function of the surface or interface area for different HfO_2 polymorphs, as sketched in Fig. 4.2 [85]. Very thin films rather tend to become tetragonal, thick films (small surface area compared to the volume of the film) tend to be monoclinic. The fact that for devices thin oxide films are needed already promotes the formation of a higher κ phase. On the other hand, thinner films typically

		pure HfO_2	$Hf_{0.8}Lu_{0.2}O_{1.9}$
		$a_m = 7.27$ Å^3	$a_m = 7.31$ Å^3
Phase	V_m (Å^3)	κ	
Amorphous	37.2 [95]	14.5	13.3
Monoclinic	34.6	23.3	20.4
Cubic	33.5	31.4	26.5

Table 4.4: Approximate relative permittivities for amorphous, monoclinic and cubic HfO_2 and $Hf_{0.8}Lu_{0.2}O_{1.9}$ using the Clausius-Mossotti equation 2.8 and assuming that the molar volume does not change upon doping. Ion polarizability for Hf^{4+} taken from [11], all other ion polarizabilities taken from [27].

have higher crystallization temperatures [85], and therefore, higher anneal temperatures might be needed to transform an amorphous film into a crystalline one.

Another way to influence the phase of HfO_2 is doping the oxide with other metals. An increase in permittivity is not expected due to an increase in polarizability but due to a decrease in molar volume. For illustration the relative permittivities of HfO_2 and $Hf_{0.8}Lu_{0.2}O_2$ were calculated using the Clausius-Mossotti equation for the amorphous, monoclinic and cubic phases in Tab. 4.4. Even though the absolute values are probably not reliable (the known experimental values for pure HfO_2 don't fit the ones calculated here), from the tendencies one can see that the phase transformation is the key to enhance κ and the influence of the polarizability of the dopant on κ is rather small.

There are also various first-principle/ ab-initio calculations on doping HfO_2: Substitutions of Hf with ions with small ionic radius like Si or Al shorten the dopant oxygen bonds and induce a distortion of the lattice which results in a tetragonal lattice [72, 74]. On the other hand the cubic phase of HfO_2 does not show any short metal-oxygen bonds and therefore doping with elements with large ionic radius like Gd or Y facilitates the formation of the cubic phase with long dopant-oxygen bonds [72].

Various experimental works have investigated the effects of doping HfO_2 [65–74]. For example Park et al. reached $\kappa = 47$ by adding Al [65], Er introduction resulted in a κ of 28, see Govindarajan et al. [96], and Adelmann et al. found that Dy or Sc doping enhances the relative permittivity to 32 [68]. A small overview over HfO_2 doping experiments is given by Wiemer et al. [97]. Typically the optimum doping content is around 10 % and all the experiments have in common that post deposition annealing processes at 500°C or higher are needed to transform the films into a higher κ phase.

Numerous other parameters have influence on the phase of HfO_2. It depends not only on doping, film thickness and grain sizes, but also on substrate, deposition technique, film stress and impurities [98].

Hence predictions of phase and permittivity become more complicated including these effects and therefore also experiments are needed to test phase and permittivity of doped

HfO_2 in actual devices.

In this chapter the influence on κ of doping HfO_2 using an ozone based ALD process is analyzed. Al and Lu doping are investigated in more detail - for example the dependence on doping concentration, annealing temperature and cleaning on CET and permittivity are tested - while La and Er are covered just briefly to find out if there is a general trend for rare earth doping. Even if similar experiments have been done before, additional experiments are justified because even small process deviations can influence the resulting phase. A striking example was reported by Lamperti et al.: they demonstrated that ALD-ZrO_2 consists of a mixed phase including a monoclinic fraction or a cubic/tetragonal phase with no monoclinic portion depending on whether H_2O or O_3 was used as oxygen precursor [98]. All the HfO_2 processes presented here were based on an ozone type process while most of the processes in literature are water based processes.

4.2 Aluminum doped HfO_2

In a first set of samples the influence of the Al content on the CET was investigated. The optimum composition was expected for rather low fractions of Al because Al_2O_3 has a rather low permittivity compared to HfO_2 and hence only the phase transition effect is supposed to raise κ. For the case of doping with Si, which is rather similar to Al respective the atomic mass, it was shown that small fractions of Si between 4 % and 10 % were enough to reach the tetragonal phase and a higher κ upon annealing whereas greater amounts of Si reduced the permittivity again [66]. Therefore, this work focused on Al contents between 4 % and 40 %. The variation of Al was done by changing the ratio of Al cycles to Hf cycles in a supercycle from 1:2 to 1:20. The growth rates per cycle for pure HfO_2 and Al_2O_3 are similar. Therefore, Al to Hf atomic ratios in the oxide layers were expected to be similar to the cycle ratios.

The absolute Al content was determined by RBS. Since the Al signal in the spectra can be hardly separated from the Si signal due to the similar atomic masses, a Ge buffer of about 140 nm was introduced between the Si substrate and the oxide to shift the Si signal to lower energies and make the proportionally small Al fraction visible. These were additional samples in an oxide deposition only used for RBS. Electrical characterization was done for oxides directly grown on Si as described in Chapter 3.

An example for an RBS measurement is presented in Fig. 4.3. Apart from the O signal the signals of the different components (Si, Al, Ge, Hf) are separated and facilitate a simulation of the layer system. The simulation unfolds 25 atomic % Al in a 4 nm thin HfO_2 film. The measurements were repeated for different samples. The values extracted from RBS should be handled as guide values since Al has a small mass and thus the Al signal of these thin layers is very low as can be seen in the inset of Fig. 4.3 which is a zoom in of the full spectra. The Al signal mixes up with the background noise and hampers an exact determination. Some values for the Al content were extrapolated using the known values and the cycle ratio.

A similar problem arises when determining the oxygen content in the oxide layer. As can

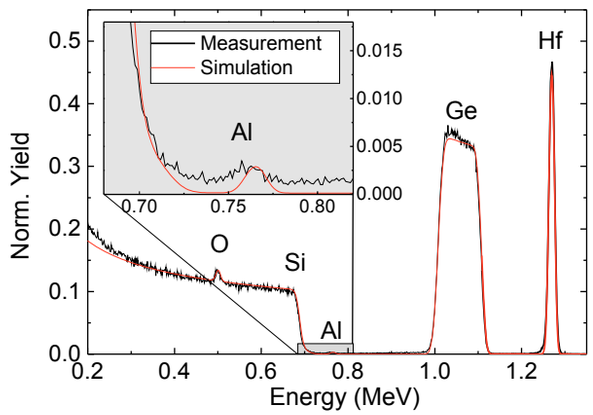

Figure 4.3: Spectra of an RBS measurement of ca. 4 nm Al doped HfO_2 grown on 140 nm Ge on Si. Inset: Zoom into the spectra to illustrate the Al signal. A simulation revealed an Al content of 25 %.

be seen in Fig. 4.3, the O signal overlaps with the Si signal because the atomic mass of O is much smaller than the one of Si. For the doped HfO_2 a lower oxygen content is expected than for pure HfO_2 due to the lower cation valence of 3 for the rare earth metals compared to the one of 4 for Hf. Further defects like oxygen vacancies have influence on the total oxygen content. For convenience throughout this work the oxygen content is described as 1-Δ with Δ a small number greater zero.

Also as an example an XRR measurement (compare Subsection 3.2.1) is presented in Fig. 4.4. Black squares represent the measured values for $Hf_{0.94}Al_{0.06}O_{2-\Delta}$ with an 800°C PDA. Fitting the positions of the maxima and minima (red curve) gives a thickness of 4.5 nm. Further the fit reveals surface and interface roughnesses below 0.5 nm.

To determine the roughness in more detail, AFM measurements were carried out. A scan over an area of (0.8×0.8) μm^2 revealed an *rms* roughness of 0.1 nm. The roughness is the same as for undoped HfO_2 layers deposited by ALD.

CV measurements on MOSCaps with $Hf_{1-x}Al_xO_{2-\Delta}$ of thicknesses between 4 nm and 6 nm and with varying Al content x are presented in Fig. 4.5.

The pure HfO_2 sample without PDA shows low hysteresis and high capacitance per area compared to the other CV curves depicted in Fig. 4.5 (a). The 800°C anneal degrades the pure HfO_2 (Fig. 4.5 (b)): the CV curve stretches out, the increased hysteresis is a sign for additional mobile charges and the capacitance is reduced.

The Al doping results in a small shift towards higher voltages of about 0.05 V for samples without PDA compared to the pure HfO_2. The samples show different maximum capacitances but up to this point no clear conclusion can be made whether this is an effect of

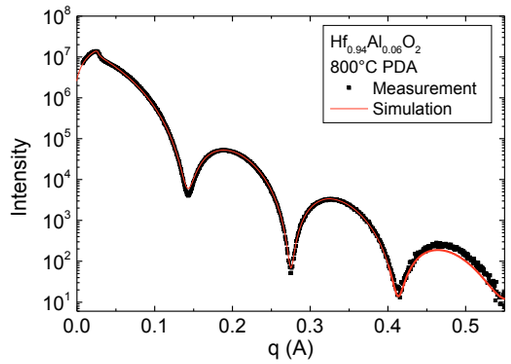

Figure 4.4: XRR measurement (black squares) and fit (red line) of $Hf_{0.94}Al_{0.06}O_{2-\Delta}$ grown on Si after an 800°C PDA. The positions of the minima and maxima reveal an oxide thickness of 4.5 nm.

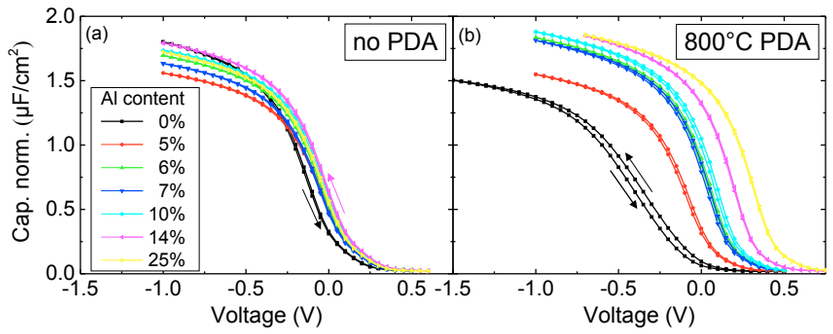

Figure 4.5: CV for $Hf_{1-x}Al_xO_{2-\Delta}$ with different Al contents for MOSCaps without (a) and with (b) an 800°C PDA. Arrows indicate the sweep direction.

the Al content. Due to the different supercycle compositions in the ALD growth process the layers have slightly varying thicknesses. The post deposition annealed $Hf_{1-x}Al_xO_{2-\Delta}$ samples show an increasing flat band voltage shift towards positive voltages with increasing Al-content. This cannot be explained by the presence of Al itself since it has not been seen for the non-annealed samples. Possibly a transformation of the crystal structure induced changes in the bonding configuration between Al and O and thus changes the number of oxygen vacancies. Charged oxygen vacancies shift the flat band voltage.

Most interestingly the capacitances of the 800°C PDA $Hf_{1-x}Al_xO_{2-\Delta}$ samples are typically higher than the ones of the samples without PDA.

Without knowing the thickness of the interfacial SiO_2 layer it is not possible to estimate the exact relative permittivity from a single sample. Nevertheless, assuming an interfacial SiO_2 layer of 1.2 nm (which is reasonable for an RCA or MegsPD cleaned Si wafer) and taking into account the $Hf_{1-x}Al_xO_{2-\Delta}$ layer thickness an effective permittivity κ_{eff} can be extracted using $\kappa_{eff} = \kappa_{SiO_2} \cdot \epsilon_0/(CET - 1.2\text{nm})$. CET is calculated by taking the capacitance at $(V_{fb} - 1\,\text{V})$. Even if the absolute permittivity is different, the effective value is sufficient to compare the different sample sets enabling a judgment of the permittivities without processing a complete set of samples needed for a CET plot for every single case. (After the most promising Al content and PDA temperature are identified a CET plot will be used to evaluate the exact permittivity for the optimized process, see below.)

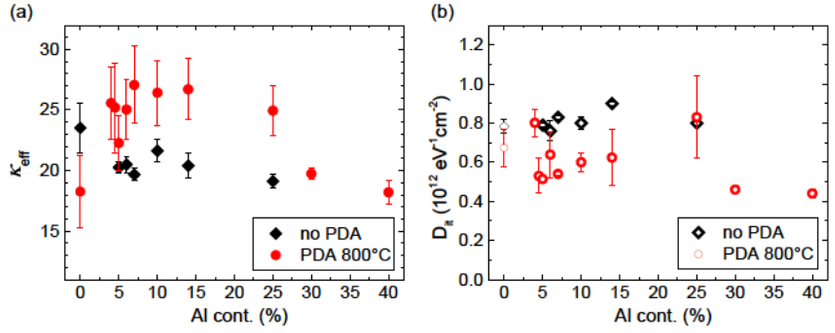

Figure 4.6: (a) Effective permittivity κ_{eff} and (b) density of interfacial traps D_{it} for different Al contents in HfO_2 for samples without (black) and with (red) post deposition annealing at 800°C. Error bars are gained by averaging the measurement results on different contacts.

Fig. 4.6 (a) shows the effective permittivity for $Hf_{1-x}Al_xO_{2-\Delta}$ films for Al contents between 0 and 40 % for samples without and with an 800°C PDA. As was already deduced from CV pure HfO_2 degrades after annealing. While the doped samples without anneal exhibit smaller κ_{eff} than pure HfO_2, the annealing greatly enhances the permittivity to values greater than the ones for pure HfO_2. Only for very high Al ratios of 30 % or 40 % no improvement is observed. The effective permittivity of the annealed samples reaches a

maximum at ≈10 atomic % of Al. Hence, for the successive investigations the Al content was fixed to 10 %. One disadvantage of annealing is the reduced homogeneity of the capacitance values: the increased error bars deduced from averaging over several data points are larger for measurements on annealed samples.

Fig. 4.6 (b) shows the respective values for the density of interfacial traps. Even though the values show some variations - values spread between $4 \times 10^{11}\,\mathrm{eV}^{-1}\mathrm{cm}^{-2}$ and $9 \times 10^{11}\,\mathrm{eV}^{-1}\mathrm{cm}^{-2}$ - by trend the annealed samples show lower D_{it} than the samples with only FGA. Also the Al doped layers show slightly better trap densities than the pure HfO_2 layers. The layers showing the highest κ_{eff} also show low density of interfacial traps mostly between $5 \times 10^{11}\,\mathrm{eV}^{-1}\mathrm{cm}^{-2}$ and $6 \times 10^{11}\,\mathrm{eV}^{-1}\mathrm{cm}^{-2}$.

Since annealing has great influence on the dielectric properties of the films, samples were prepared and annealed at different temperatures. The respective CV curves (not shown here) show slight shifts of the flat band voltage for post deposition annealed samples at 600°C - 1000°C compared to samples with only FGA, but these shifts are both negative and positive and do not exceed 0.1 eV.

In Fig. 4.7 (a) the CET values of the respective samples are summarized. All PDA samples have lower CET than the non annealed samples. Judging simply the CET, post deposition annealing at 600°C, 900°C and 1000°C provide optimum results. However, XRR measurements reveal that the thickness of the oxide layer d changes with PDA temperature and the higher CET for 700°C can be explained by an increased layer thickness. Assuming that the amount of Al and Hf atoms stays constant during annealing probably the density of the $Hf_{0.9}Al_{0.1}O_{2-\Delta}$ changes due to a phase transformation (compare Section 4.6).

The effective permittivity κ_{eff} is calculated in order to enable a more reasonable comparison, see black diamonds in Fig. 4.7 (b). All five annealing processes increase the permittivity compared to the non annealed sample. The best κ_{eff} of ≈ 37 is achieved for a 700°C PDA.

Disregarding the layers annealed at 800°C, the density of interfacial traps, shown in red in Fig. 4.7 (b), drops from $1 \times 10^{12}\,\mathrm{eV}^{-1}\mathrm{cm}^{-2}$ to $5 \times 10^{11}\,\mathrm{eV}^{-1}\mathrm{cm}^{-2}$ for increasing PDA temperature up to 1000°C.

Samples with different thicknesses were prepared to evaluate a precise value of the relative permittivity of $Hf_{0.9}Al_{0.1}O_{2-\Delta}$ annealed at 700°C. The CV measurements of the corresponding MOSCaps are presented in Fig. 4.8.

As expected the capacitance per area decreases with increasing thickness. The small hysteresis reveals mobile charges in the layer. The CV curves are slightly shifted towards positive voltages compared to pure HfO_2, but hardly changes with thickness. Only the thinnest layer has ca. 0.1 V lower flat band voltage than the thicker layers.

While for thicker layers the capacitance still slightly increases with decreasing voltage, the capacitance of the 2.6 nm thin sample starts to decrease at voltages around -1.3 V. This can be explained by a decharge of the capacitance due to small leakage currents that occur for thin layers at a certain voltage.

In a so-called CET plot the CET values derived from the CV curves are plotted as a

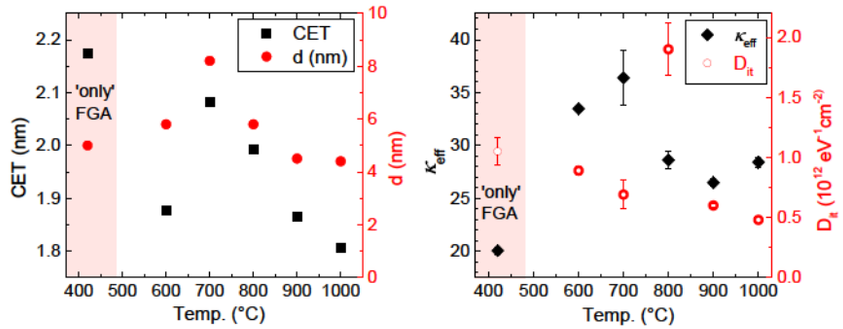

Figure 4.7: CV investigations on $Hf_{0.9}Al_{0.1}O_{2-\Delta}$ for different post deposition annealing temperatures: (a) CET (left axis, black squares) and oxide layer thickness d (right axis, red circles) and (b) Effective permittivity κ_{eff} (black diamonds, left axis) and density of interfacial traps D_{it} (red circles, right axis) as a function of PDA temperature. The data points at 420°C refer to MOSCaps that received a FGA, but no additional PDA right after the oxide deposition. Error bars are gained by averaging the measurement results on different contacts. A maximum permittivity is observed for a 700°C PDA.

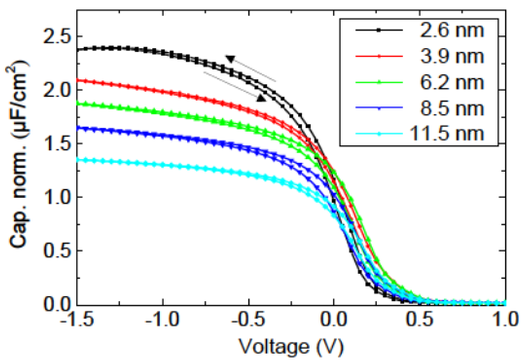

Figure 4.8: CV for $Hf_{0.9}Al_{0.1}O_{2-\Delta}$ with different layer thicknesses annealed at 700°C. Arrows indicate the sweep direction.

function of oxide layer thickness. Assuming that the SiO_2 interfacial layer thickness stays constant one can perform a linear regression and derive the relative permittivity from the inverse of the slope of the linear fit and the CET of the interfacial layer by the intercept of the fitted line with the y-axis following Equation 2.11.

Several CET plots are depicted in Fig. 4.9 (a) to compare non annealed $Hf_{0.9}Al_{0.1}O_{2-\Delta}$ with $Hf_{0.9}Al_{0.1}O_{2-\Delta}$ post deposition annealed at 600°C, 700°C and 800°C. The interfacial layer thickness varies between 1.1 nm and 1.3 nm without any visible tendency with temperature. The absolute relative permittivities confirm the trend already observed in Fig. 4.7 (b) for the effective permittivities. $Hf_{0.9}Al_{0.1}O_{2-\Delta}$ without any post deposition annealing has the lowest κ of 19 which fits well to the relative permittivity of pure HfO_2 of ca. 18 for layers deposited under equal conditions just without Al input. Annealing at 600°C or 800°C enhances κ to 26 and 24, respectively, but the highest relative permittivity is achieved using an intermediate temperature of 700°C resulting in $\kappa = 30$.

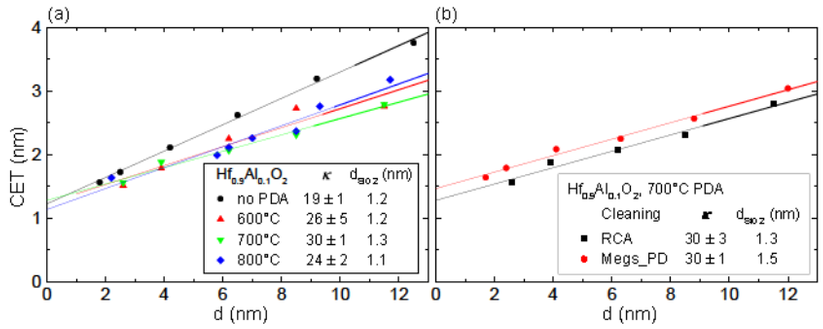

Figure 4.9: CET plot for $Hf_{0.9}Al_{0.1}O_{2-\Delta}$ (a) annealed at different temperatures and (b) annealed at 700°C for different cleaning procedures. Errors are deduced from the linear regression results.

Along with the experiments performed to optimize the relative permittivity, also devices were created to compare the different cleaning methods.

In Fig. 4.9 (b) CET plots for two different batches of $Hf_{0.9}Al_{0.1}O_{2-\Delta}$ post deposition annealed at 700°C are presented. The extracted relative permittivities are the same stating good reproducibility of the dielectric properties.

The intercept with the y-axis which displays the CET of the interfacial layer varies by 0.2 nm. Besides the differences in cleaning, for the first set of samples cleaned by RCA FGA was done directly after TiN deposition and for the second set FGA was executed at the end of the process. None of these changes can be completely excluded as reason for the interfacial layer differences. Nevertheless, cleaning is the most probable origin for the difference in interfacial layer CET. A scavenging process due to the FGA is implausible because it would be expected to decrease the interfacial layer thickness of the second batch with the final FGA because then Al as scavenging element is present. Though the observed

tendency is the opposite.

An estimation of the density of interfacial traps uncovers that the RCA cleaned samples have better interface characteristics: MegsPD cleaned samples show a D_{it} of $(1-2) \times 10^{12}\,\mathrm{eV}^{-1}\mathrm{cm}^{-2}$, RCA cleaned ones of $(5-8) \times 10^{11}\,\mathrm{eV}^{-1}\mathrm{cm}^{-2}$.

Regarding interfacial layer thickness and D_{it}, RCA cleaned Si should be preferred for devices.

The above measurements show that the relative permittivity of $Hf_{1-x}Al_xO_{2-\Delta}$ can be optimized to a value of 30 by adjusting the Al content and the PDA temperature. Further doping and annealing can shift the flat band voltage and result in slightly lower densities of interfacial traps.

Since pure amorphous HfO_2 and Al_2O_3 have lower κ the enhancement of the permittivity is probably caused by a transformation to a higher-κ phase of HfO_2, like the cubic or tetragonal phase. This aspect is studied in detail by XRD and TEM analysis in Section 4.6.

4.3 Lutetium doped HfO_2

As already mentioned in the introduction also rare earth (RE) atoms are used to dope HfO_2 and raise its relative permittivity [71, 72, 96, 99]. Various RE elements have been tested, but no reports on Lu doping are known to the author. Therefore in the following part the effects of Lu doping into HfO_2 are investigated.

The atomic weights of Hf and Lu (178.49 and 174.97, respectively [100]) differ only slightly and thus their RBS signals cannot be separated from each other. Therefore, TOF-SIMS was used to determine the composition of the deposited $Hf_{1-x}Lu_xO_{2-\Delta}$ layers. Only thicker samples were investigated this way because the Lu and Hf signals of thin oxide layers do not form plateaus in the TOF-SIMS spectra. Thus, the Lu content for thin samples is extrapolated knowing the content of the thicker one and assuming reproducible growth which is a typical characteristic of ALD [45].

To calibrate the SIMS profile a reference sample was produced: thick HfO_2 (ca. 50 nm) was deposited by ALD and then Lu was implanted at a fixed dose. Examples of the TOF-SIMS signals of a Lu implanted HfO_2 layer and a $Hf_{1-x}Lu_xO_{2-\Delta}$ layer completely deposited by ALD are depicted in Fig. 4.10.

The measured counts for the Si^- and HfO^- ions were calibrated by the atomic density for Si and HfO_2 and the LuO^- ion counts were calibrated from the implanted signal in comparison to simulated values for the Lu density. For the sample presented in Fig. 4.10 with an opening time of the Lu precursor line during ALD of 25 seconds the Lu content varied between 19 % and 21 %. Hence the medium value is 20 at. % Lu. Equivalently for a sample with 20 seconds opening time during ALD 15 at. % Lu were deduced.

The SIMS investigations further unfolded that in $Hf_{0.8}Lu_{0.2}O_{2-\Delta}$ more carbon was incorporated compared to pure HfO_2 indicating that the precursor molecules did not decompose completely during growth.

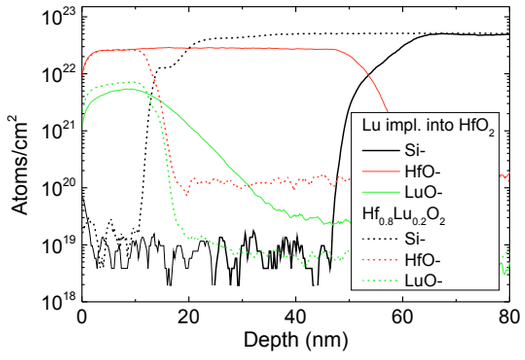

Figure 4.10: TOF-SIMS profile of Lu implanted into HfO_2 ($\approx 50\,nm$) and of $Hf_{0.8}Lu_{0.2}O_{2-\Delta}$ ($\approx 20\,nm$) grown in an ALD process with 25 s opening time of the Lu precursor line.

AFM measurements were executed to assure that the layers were smooth. They revealed an *rms* roughness of 0.5 nm. This is higher than for the other ALD layers (HfO_2 and $Hf_{0.9}Al_{0.1}O_{2-\Delta}$), but still appropriate for device application.

Generally the transformation to a higher κ phase occurs at higher temperatures above 500°C [71, 96, 97]. Therefore, $Hf_{0.85}Lu_{0.15}O_{2-\Delta}$ layers post deposition annealed at temperatures between 600°C and 1000°C were compared to layers without PDA. The phase transformation should be visible in an increase of the effective permittivity.

CV measurements on $Hf_{0.85}Lu_{0.15}O_{2-\Delta}$ MOSCaps annealed at different PDA temperatures are presented in Fig. 4.11 (a). The hysteresis is low for all CV curves so few mobile charges were present. The flat band voltage for the stack with only FGA is shifted about 0.1 eV compared to pure HfO_2. For a PDA temperature of 600°C the CV curve shifts even more towards positive voltages by additional 0.2 eV. For increasing anneal temperatures the flat band voltage shifts back. Thus, the sample annealed at 1000°C has almost equal flat band voltage to pure HfO_2.

Some CV measurements show a slight hump which is an indication of traps at the interface. This coincides with the rather high densities of interfacial traps up to $2.1 \times 10^{12}\,eV^{-1}cm^{-2}$ for the layer annealed at 800°C, see Fig. 4.11 (b). Very low density of interfacial traps ($\approx 3 \times 10^{11}\,eV^{-1}cm^{-2}$) is achieved for very high anneal temperatures of 1000°C.

Fig. 4.11 (b) also depicts the effective permittivities of the respective $Hf_{0.85}Lu_{0.15}O_{2-\Delta}$ layers. The relative permittivity of a non-annealed sample is slightly above 24. Contrary to the expectations mentioned above for anneals between 600°C and 900°C κ_{eff} decreases down to 18. Only for temperatures of 1000°C the permittivity recovers to the value achieved without PDA.

Several effects may play a role to this degradation like silicate formation [101], inter-

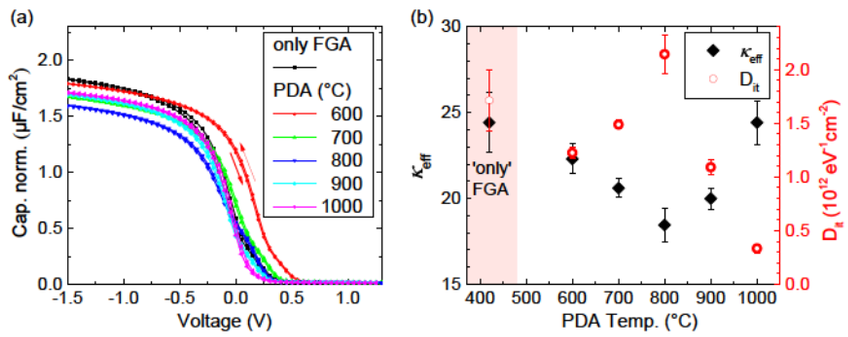

Figure 4.11: Results from measurements on $Hf_{0.85}Lu_{0.15}O_{2-\Delta}$ for different PDA temperatures. (a) Capacitance voltage measurements. Arrows indicate sweep direction. (b) Effective permittivity κ_{eff} (black diamonds, left axis) and density of interfacial traps D_{it} (red circles, right axis) as a function of PDA temperature.

facial layer growth, or a transformation to the unwanted monoclinic phase. Irrespective of the source of this behavior from the point of view of application the non-annealed $Hf_{0.85}Lu_{0.15}O_{2-\Delta}$ is preferred for devices because of the high effective permittivity and the low thermal budget during process. Consequently, in the following investigations samples without any PDA are discussed.

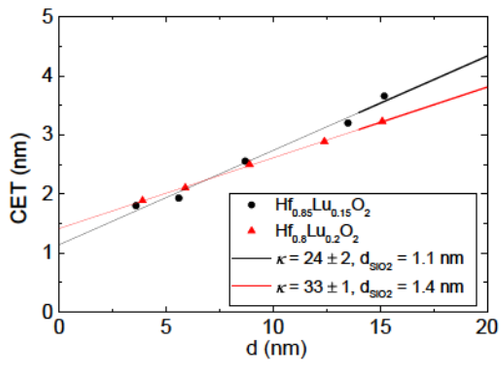

Figure 4.12: CET plot for $Hf_{0.85}Lu_{0.15}O_{2-\Delta}$ and $Hf_{0.8}Lu_{0.2}O_{2-\Delta}$.

Fig. 4.12 shows ***CET*** plots for two different Hf to Lu ratios. The extracted relative permittivities are 25 and 33 for 15 % and 20 % Lu, respectively. Thus, regarding the permittivity, higher Lu content is the better choice for devices, even though both materials show higher κ than pure HfO_2 (ca. 18). However, the samples with 20 % Lu also have a

disadvantage: while $Hf_{0.85}Lu_{0.15}O_{2-\Delta}$ layers on Si showed a D_{it} of $(2-5)\times10^{11}\,eV^{-1}cm^{-2}$, $Hf_{0.8}Lu_{0.2}O_{2-\Delta}$ stacks had trap densities of $(1-1.4)\times10^{12}\,eV^{-1}cm^{-2}$. Further the interfacial layer thickness for $Hf_{0.85}Lu_{0.15}O_{2-\Delta}$ was lower which is important for CET scaling.

4.4 Erbium and Lanthanum doped HfO_2

Also Er and La were used to dope HfO_2. While the Er precursor was evaporated in an oven similarly to Lu during the ALD process, the La precursor was injected as a liquid dissolved in octane. The Er content was determined by SIMS and the La content was determined by RBS. For both materials the content of dopants turned out to be 11 at.%.

Samples with different thicknesses and without PDA were investigated respective their capacitance voltage characteristics. Both types of oxides show low D_{it} of $(6-8)\times10^{11}\,eV^{-1}cm^{-2}$ and the flat band voltages are the same as for pure HfO_2 or up to 0.3 V lower than for pure HfO_2.

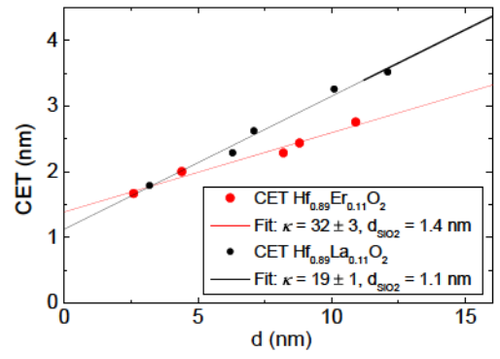

Figure 4.13: CET plot for $Hf_{0.89}Er_{0.11}O_{2-\Delta}$ and $Hf_{0.89}La_{0.11}O_{2-\Delta}$. The linear fits reveal relative permittivities of 32 and 19 for $Hf_{0.89}Er_{0.11}O_{2-\Delta}$ and $Hf_{0.89}La_{0.11}O_{2-\Delta}$, respectively.

The corresponding CET plots are depicted in Fig. 4.13. While $Hf_{0.89}Er_{0.11}O_{2-\Delta}$ with a high κ of 32 reproduces the permittivity enhancement seen for $Hf_{0.8}Lu_{0.2}O_{2-\Delta}$, $Hf_{0.89}La_{0.11}O_{2-\Delta}$ shows a rather low κ of 19 similar to the one for amorphous or monoclinic HfO_2 [80–82]. The source for this discrepancy is due to differences in the crystallization behavior and is discussed in more detail in Section 4.6 and Section 4.7.

4.5 Insulating properties

Apart from a high permittivity it is essential for gate oxides to have good insulating properties. This can be evaluated by determining the band gap and by directly measuring the leakage currents on a MOSCap as a function of EOT.

4.5.1 Band gap of $Hf_{0.8}Lu_{0.2}O_{2-\Delta}$

In the case of $Hf_{0.8}Lu_{0.2}O_{2-\Delta}$ ellipsometry was employed to determine the band gap. For comparison also HfO_2 was investigated. Ellipsometer spectra of HfO_2 and $Hf_{0.8}Lu_{0.2}O_{2-\Delta}$ are presented in Fig. 4.14.

A stacked structure of Si, SiO_2, HfO_2 or $Hf_{0.8}Lu_{0.2}O_{2-\Delta}$ and a surface layer was assumed for modeling, compare Fig. 3.13. The thicknesses of all layers and the optical constants of the Hf based oxides were fitted, while the optical constants of Si and SiO_2 were taken by the software's tabulated database based on [102]. The surface was simulated using the *Bruggeman Effective Medium Approximation* [103]. For the optical constants of the Hf based oxides the general oscillator model was considered consisting of Tauc-Lorentz oscillators [104]. The high quality of the fitting was approved by determination of the MSE (compare Eq. 3.8) which equals 1.4 and 1.2 for HfO_2 and $Hf_{0.8}Lu_{0.2}O_{2-\Delta}$, respectively, and can be seen in the good overlap of measurement and model in Fig. 4.14.

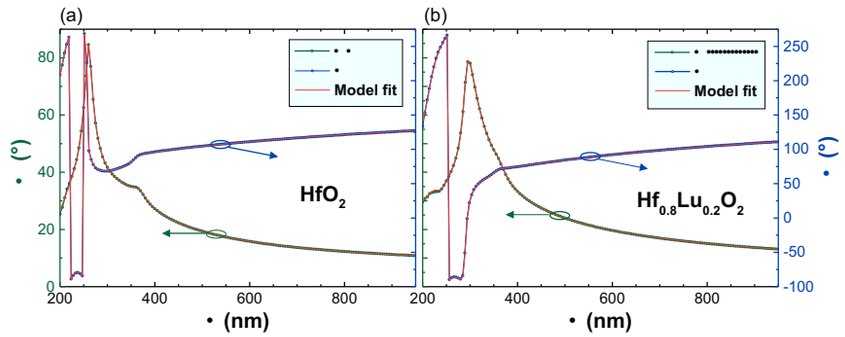

Figure 4.14: Ellipsometric spectra of (a) HfO_2 and (b) $Hf_{0.8}Lu_{0.2}O_{2-\Delta}$: Ellipsometric parameters Ψ (left, green axis) and Δ (right, blue axis) and the respective model fits (red).

The absorption coefficient α was calculated using the relation $\alpha = 4\pi k/\lambda$. The band gap energy E_g can be obtained by the extended Tauc formula for direct band gaps [105]:

$$(\alpha E)^2 \approx E - E_g. \tag{4.1}$$

E_g results from the tangent of $(\alpha E)^2$ with the energy axis, compare Fig. 4.15. For HfO_2 and $Hf_{0.8}Lu_{0.2}O_{2-\Delta}$ energy band gap values of 5.7 eV and 5.8 eV were determined, respectively. In literature even higher values were reported (e.g. 6.0 eV for HfO_2 [23]), but these differences probably relate to the deposition methods used. For the case here - ozone based ALD depositions - it was demonstrated that the band gap of HfO_2 can be increased by Lu doping. In the next section the insulating properties will also be directly tested by leakage current measurements.

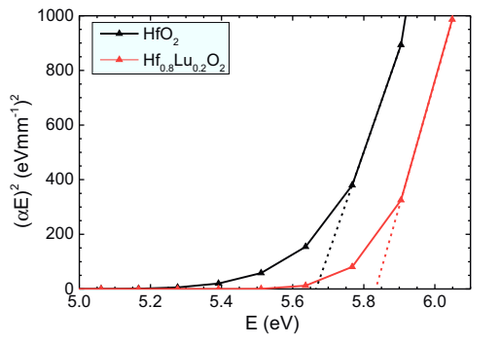

Figure 4.15: $(\alpha E)^2$ as a function of E for HfO_2 and $Hf_{0.8}Lu_{0.2}O_{2-\Delta}$. The band gap can be determined from the intercept of the extrapolated slope with the energy axis.

4.5.2 Leakage currents

Leakage current measurements are presented for $Hf_{0.9}Al_{0.1}O_{2-\Delta}$ and $Hf_{0.8}Lu_{0.2}O_{2-\Delta}$ in Fig. 4.16: the absolute values of the current densities are plotted as a function of applied voltage for different EOT values (which correspond to different layer thicknesses). In the case of $Hf_{0.9}Al_{0.1}O_{2-\Delta}$ (Fig. 4.16 (a)) the leakage currents rise slightly for increasing positive voltages because the inversion layer in the semiconductor adds to the total insulating layer thickness. For decreasing voltages respective the flat band voltage the leakage currents rise in a steeper manner. In this case the MOSCap is in accumulation and charge carriers are present directly at the semiconductor oxide interface. As expected for thicker layers, i.e. higher EOT, the leakage current density decreases: at $(V_{fb} - 1V)$ the leakage current density decreases from $3 \times 10^{-3}\,\mathrm{A/cm^2}$ to $1.5 \times 10^{-9}\,\mathrm{A/cm^2}$ for EOT between 1.2 nm and 2.8 nm.

For $Hf_{0.8}Lu_{0.2}O_{2-\Delta}$ (see Fig. 4.16 (b)) the leakage currents are almost independent on layer thickness: at $(V_{fb}-1V)$ the leakage current density is around $3\times10^{-7}\,\mathrm{A/cm^2}$ for EOT between 1.2 nm and 2.8 nm. In contrast to $Hf_{0.9}Al_{0.1}O_{2-\Delta}$ there is hardly any difference between the accumulation and the depletion branch in the current voltage course.

To compare different materials the leakage current densities at $V = V_{fb} - 1V$ are plotted as a function of EOT, see Fig. 4.17. For gate dielectrics EOT and leakage currents are supposed to be as low as possible. For a given material the EOT can be lowered by decreasing the layer thickness but for thin layers the leakage currents are dominated by tunneling currents. This is also observed for Al doped HfO_2: for small EOT the leakage current densities start to increase exponentially, cf. Section 2.8. The measured values for $Hf_{0.9}Al_{0.1}O_{2-\Delta}$ lie on one line with the values for pure HfO_2 demonstrating that they show almost equal tunneling characteristics and that the leakage is not increased by Al doping.

The fact that the current densities of $Hf_{0.8}Lu_{0.2}O_{2-\Delta}$ do not depend on EOT means that

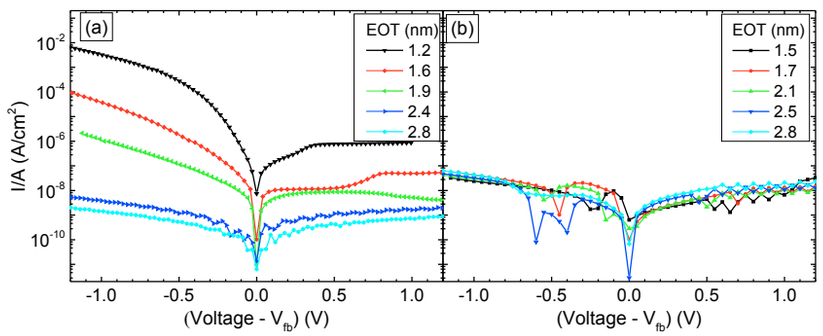

Figure 4.16: Representative leakage current densities as a function of applied voltage of (a) $Hf_{0.9}Al_{0.1}O_{2-\Delta}$ annealed at 800°C and (b) $Hf_{0.8}Lu_{0.2}O_{2-\Delta}$ without PDA for different *EOT*.

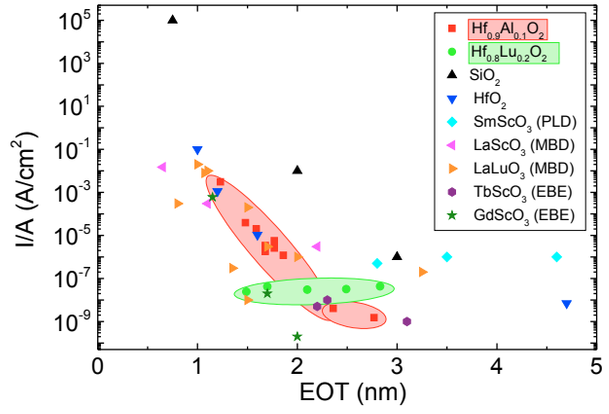

Figure 4.17: Representative leakage current densities as a function of *EOT* for doped HfO_2 in comparison to various oxides, adapted from [106]. The abbreviations in brackets identify the deposition method for the respective oxide (PLD - pulsed laser deposition, MBD - molecular beam deposition, EBE - electron beam evaporation). The leakage current values for $Hf_{0.9}Al_{0.1}O_{2-\Delta}$ are taken from Fig. 4.16 but also from measurements of samples without PDA or PDA at 600°C and 700°C. The leakage current densities of $Hf_{0.8}Lu_{0.2}O_{2-\Delta}$ are presented for samples without PDA.

for the oxides thicknesses investigated tunneling does not dominate yet. Investigations on thinner oxides stacks are needed to investigate where the tunneling starts.

Fig. 4.17 demonstrates that $Hf_{0.8}Lu_{0.2}O_{2-\Delta}$ outperforms most of the other oxides, also $Hf_{0.9}Al_{0.1}O_{2-\Delta}$, for *EOT* between 1.5 nm and 2 nm. Only $LaLuO_3$ shows similar leakage current density in this *EOT* range.

The detailed analysis of $Hf_{0.9}Al_{0.1}O_{2-\Delta}$ and $Hf_{0.8}Lu_{0.2}O_{2-\Delta}$ revealed that these newly developed oxides are suitable as gate dielectric. Thin and smooth layers can be deposited that show high permittivities of 30 and 33, respectively. $Hf_{0.9}Al_{0.1}O_{2-\Delta}$ shows low $D_{it} \approx (0.5-1) \times 10^{12}\,\mathrm{eV^{-1}cm^{-2}}$ and low leakage currents that fit to the values determined for pure HfO_2. $Hf_{0.8}Lu_{0.2}O_{2-\Delta}$ shows slightly higher $D_{it} \approx 10^{12}\,\mathrm{eV^{-1}cm^{-2}}$ and even outperforms pure HfO_2 respective its insulating properties: the band gap $E_g = 5.8\,\mathrm{eV}$ is slightly higher than for HfO_2 and the leakage currents are in the range of $10^{-8}\,\mathrm{A/cm^2}$ for an *EOT* down to 1.5 nm.

4.6 Crystallographic Characterization

The crystal structure of the films is investigated to be able to interpret the origin of the permittivity enhancement in the doped HfO_2 layers.

Well-oriented, single-crystalline films are unlikely because the deposition was done on an amorphous SiO_2 layer which hinders epitaxial growth. Hence, gracing incidence XRD (GIXRD) and TEM were used to determine whether the films are amorphous or polycrystalline.

Crystal structure of $Hf_{0.9}Al_{0.1}O_{2-\Delta}$

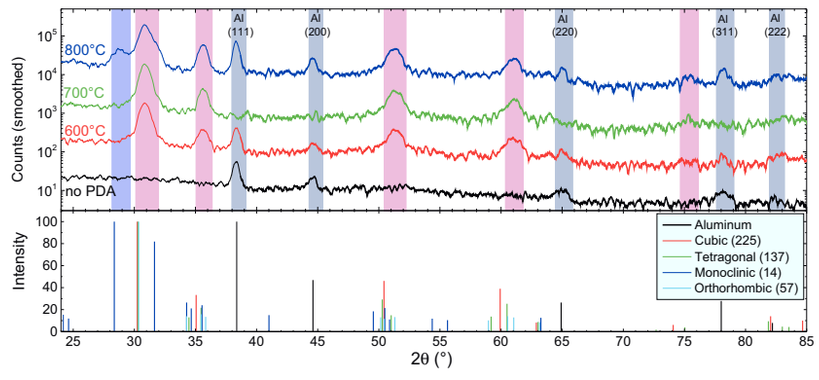

Figure 4.18: Upper graph: GIXRD of $Hf_{0.9}Al_{0.1}O_{2-\Delta}$ for different PDA temperatures. To reduce noise the measurement data were smoothed over 20 points. (The measured counts are multiplied by 10, 100 and 1000 for the 600°C, 700°C and 800°C PDA samples, respectively, to facilitate the comparison of the four samples.) Only the sample annealed at 700°C was measured before TiN and Al deposition. The shaded areas in the background categorize the different peaks: gray - Al-reflexes, red - peaks present for annealed samples, blue - peak only present for the sample annealed at 800°. Lower graph: Calculated diffraction patterns for Al [107] and for HfO_2 in the cubic, tetragonal, monoclinic or orthorhombic unit cells [75–78]. The numbers in brackets specify the space group numbers of the different polymorphous cells. Note: at 30.3° reflections of cubic, tetragonal and orthorhombic HfO_2 are present. The lattice constants of the different HfO_2 phases are summarized in Tab. 4.1

The upper part of Fig. 4.18 summarizes GIXRD measurements on $Hf_{0.9}Al_{0.1}O_{2-\Delta}$ for different PDA temperatures. Three of the samples were analyzed after Al deposition and therefore show several Al reflections (see peaks marked by gray shaded areas). The sample without PDA did not show any additional peaks to the Al peaks. After annealing at either

600°C or 700°C diffraction peaks arose marked in red. After an 800°C PDA a peak at 28.8° (blue area) and possibly a shoulder around 32.5° added up to the spectra.

To be able to correlate the peaks to the known phases of HfO_2 calculated diffraction patterns of different HfO_2 unit cells are depicted in the lower part of Fig. 4.18. To distinguish between the cubic, tetragonal and orthorhombic phase is difficult since at 30.3° the reflections overlap and for higher angle they typically cluster in groups of peaks. Further, one cannot exclude that only one phase is present at the same time. Thus, an unambiguous conclusion is not possible. Nevertheless, assuming that the broadening of the measured reflections is rather caused due to the thin film than due to the many phases present, the peaks above 30° most probably originate from a cubic phase. For the reflection at 28.8° the monoclinic phase fits best.

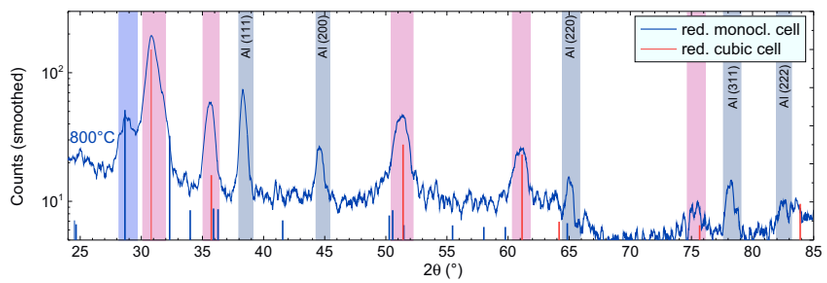

Figure 4.19: GIXRD of $Hf_{0.9}Al_{0.1}O_{2-\Delta}$ annealed at 800°C in comparison to the diffraction patterns of reduced monoclinic and cubic cells. Shaded areas are identical to Fig. 4.18.

Yet the exact angles for the calculated and measured reflections do not coincide. The measured peaks tend to be at slightly higher angles than the calculated ones. This can be explained by the Al doping. The bond length between Al and O is smaller than the one between Hf and O [72], and therefore, replacing Hf atoms by Al can cause a reduction of the unit cell volume. Smaller lattice constants result in higher angles in the diffraction pattern. In Fig. 4.19 the cubic and monoclinic unit cells are adjusted to fit best the GIXRD pattern of the sample annealed at 800°C. (This sample was chosen because it shows all peaks.) Reducing the lattice constant of cubic HfO_2 from $a = 5.115\,\text{nm}$ [75] to $a = 5.023\,\text{nm}$ the reflections marked in red can be well described. The same can be done for the monoclinic phase, but the result is less reliable because only one peak is present and four parameters describe the unit cell. Here a cell constructed with $a = 5.02\,\text{nm}$, $b = 5.27\,\text{nm}$, $c = 5.07\,\text{nm}$ and $\beta = 99.7°$ fits well (in comparison: $a = 5.113\,\text{nm}$, $b = 5.295\,\text{nm}$, $c = 5.172\,\text{nm}$ and $\beta = 99.19°$ for pure monoclinic HfO_2 [77]).

Hence, these observations lead to first structure conclusions: the non annealed sample seems amorphous, all annealed layers show a higher κ HfO_2 phase, probably the cubic one, the film annealed at 800° shows an additional monoclinic contribution and the lattice constants are sightly reduced due to the incorporation of Al.

TEM should give more insights into the crystalline structure. Due to the time-consuming preparation and measurement only the sample annealed at 700°C with the highest permittivity was chosen for TEM.

The cross section TEM images in Fig. 4.20 present the $Hf_{0.9}Al_{0.1}O_{2-\Delta}$ layer on top of Si and a SiO_2 interfacial layer in between. The interfacial layer of roughly 3 nm is quite thick. After cleaning the SiO_2 is typically around 1 nm thick. Hence, it grows in thickness either during ALD process, during the post deposition annealing or during TEM imaging. Furthermore both surface and interface to SiO_2 of the Al doped HfO_2 are smooth. In the left part of Fig. 4.20 three different grains are visible in the oxide film. The visible part of $Hf_{0.9}Al_{0.1}O_{2-\Delta}$ in the right part forms a single crystal. The images confirm that the films are polycrystalline. Even more images (not shown here) reveal that grains can reach sizes of up to hundreds of nanometers along the surface plane. In the normal direction the grain size is limited by the layer thickness.

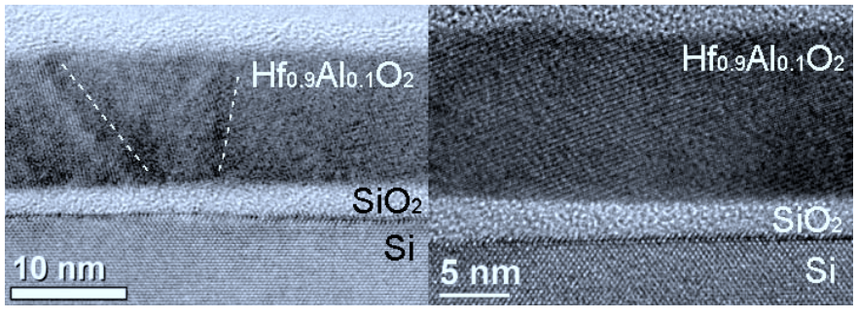

Figure 4.20: Cross section HRTEM images of different regions of $Hf_{0.9}Al_{0.1}O_{2-\Delta}$ on Si with a SiO_2 interface. Three different grains can be distinguished in the left image. Grain boundaries are indicated by dashed lines. The right image demonstrates one crystallite of polycrystalline $Hf_{0.9}Al_{0.1}O_{2-\Delta}$.

The Fast Fourier Transform (FFT) in Fig. 4.21 of one of the $Hf_{0.9}Al_{0.1}O_{2-\Delta}$ grains observed in TEM can be related to the monoclinic lattice of HfO_2: the spots correspond to the (011) and (11-2) reflections of monoclinic HfO_2 when assuming that one looks at the [4-11]-pole. The lattice distances $d_{011} = 0.36\,\text{nm}$ and $d_{11-2} = 0.18\,\text{nm}$ fit within 0.01 nm to what is expected for monoclinic HfO_2 in literature [77].

Crystal structure of rare earth doped HfO_2

The film structures of the rare earth doped HfO_2 layers were investigated by GIXRD and TEM. GIXRD measurements were done before metal deposition and typically on films with thicknesses of about 12 nm. The results are depicted in the upper part of Fig. 4.22.

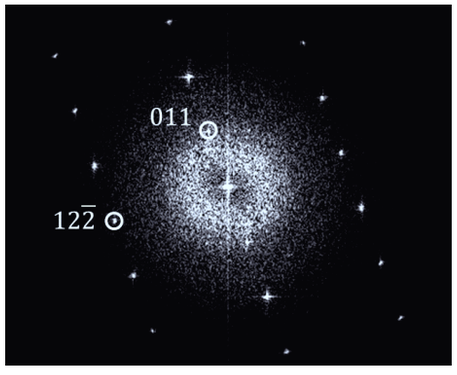

Figure 4.21: Fast Fourier Transform (FFT) of a $Hf_{0.9}Al_{0.1}O_{2-\Delta}$ grain detected by TEM cross section imaging. Assuming a monoclinic lattice in the [4-11]-pole the (011) and (11-2) reflexes are marked.

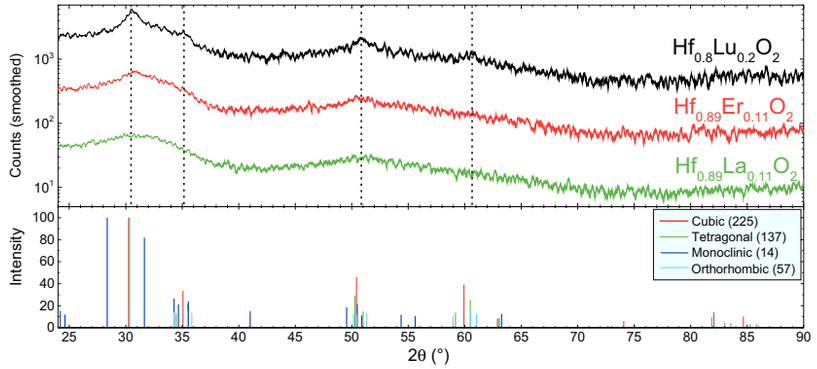

Figure 4.22: Upper part: GIXRD of $Hf_{1-x}M_xO_{2-\Delta}$ with M = Lu, Er, La and $x = 0.2, 0.11, 0.11$, respectively. (The measured counts are multiplied by 8 and 64 for Er and Lu doped HfO_2, respectively, to facilitate the comparison of the three materials.) Vertical dashed lines indicate maxima in the $Hf_{0.8}Lu_{0.2}O_{2-\Delta}$ diffraction measurement. Lower part: Calculated diffraction patterns for HfO_2 in the cubic, tetragonal, monoclinic or orthorhombic unit cells [75–78]. Numbers in brackets specify the space group numbers of the different polymorphous cells. Note: at 30.3° reflections of cubic, tetragonal and orthorhombic HfO_2 are present, compare Fig. 4.18.

In comparison to GIXRD on $Hf_{0.9}Al_{0.1}O_{2-\Delta}$ (Fig. 4.18) no clear, sharp peaks but rather broad humps are present. However, a closer comparison of the three curves depicted here reveals slight differences. While the very broad humps over several degrees of 2θ are the same for all layers, $Hf_{0.8}Lu_{0.2}O_{2-\Delta}$ also exhibits some smaller and narrower peaks indicated by dashed lines. These peaks might also be present in $Hf_{0.89}Er_{0.11}O_{2-\Delta}$, but are not visible at all for $Hf_{0.89}La_{0.11}O_{2-\Delta}$.

The broad humps probably describe typical next neighbor distances of an amorphous phase in the layer [108]. It is also possible that the films are polycrystalline with very small grains which are no more detectable by GIXRD for the setup used since diffraction peaks get broader with decreasing grain size (cf. Section 3.2.1). In contrast the narrow peaks in $Hf_{0.8}Lu_{0.2}O_{2-\Delta}$ can be compared to diffraction patterns extracted from HfO_2 unit cells mentioned in literature (see lower part of Fig. 4.22). Again the cubic phase seems to fit best, even though a tetragonal or orthorhombic phase cannot be completely excluded. Other than for $Hf_{0.9}Al_{0.1}O_{2-\Delta}$ the lattice constants are not shifted to smaller values since the bonds to the rather large rare earth atoms do not result in a reduction of bond length as for Al [72].

In short the three measurements in Fig. 4.22 might demonstrate a transition from a polycrystalline, mainly cubic $Hf_{0.8}Lu_{0.2}O_{2-\Delta}$ to an amorphous $Hf_{0.89}La_{0.11}O_{2-\Delta}$ or to a polycrystalline $Hf_{0.89}La_{0.11}O_{2-\Delta}$ with very small grains. TEM images and diffraction patterns are needed for clarification.

Fig. 4.23 represents a TEM cross sectional image of $Hf_{0.89}La_{0.11}O_{2-\Delta}$. One can clearly see that this layer is amorphous without any polycrystalline grains shortening the discussion started above. The interfacial SiO_2 has roughly a thickness of 1 nm which fits well to the SiO_2 thickness of 1.1 nm derived from the CET plot in Fig. 4.13.

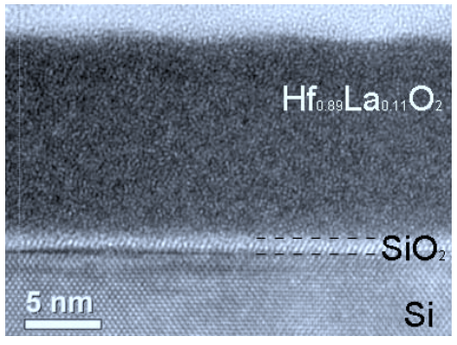

Figure 4.23: Cross section TEM of $Hf_{0.89}La_{0.11}O_{2-\Delta}$. The image demonstrates that $Hf_{0.89}La_{0.11}O_{2-\Delta}$ stays amorphous and does not crystallize into a higher κ phase.

TEM images of $Hf_{0.8}Lu_{0.2}O_{2-\Delta}$ look quite differently regarding the oxide structure. As can be seen in the cross section and plan view images in Fig. 4.24 the layers are

polycrystalline and the grains have diameters of approximately 10 nm. In some cases one can even observe Moiré fringes which can be explained by differently oriented grains stacked above one another respective the normal of the image plane. The cross section image in Fig. 4.24 also demonstrates that the film is very smooth.

The inset in the plan view image in Fig. 4.24 shows the Fast Fourier transform of one of the grains (marked by a white square). The transform indicates that this grain is cubic.

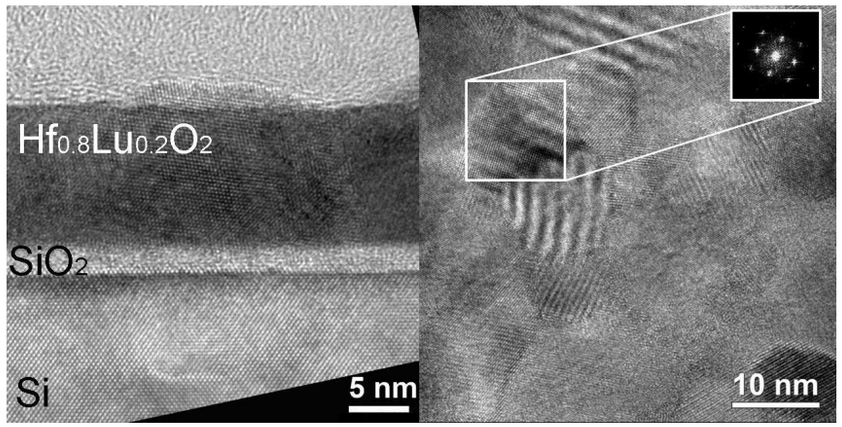

Figure 4.24: Cross section (left) and plan view (right) TEM of $Hf_{0.8}Lu_{0.2}O_{2-\Delta}$. One of the grains (region inside white square) is further investigated by a Fast Fourier transform in the inset. Both images demonstrate that the $Hf_{0.8}Lu_{0.2}O_{2-\Delta}$ layers inhibit numerous small grains with grain sizes around 10 nm.

The electron diffraction pattern in Fig. 4.25 is derived from the same plan view sample as the right image in Fig. 4.24 but of a much larger area. Four rings are visible besides some spots originating from the substrate. Such rings are typical for polycrystalline films and the radii correspond to the reciprocal lattice plane distances in the grains.

Tab. 4.5 lists the corresponding direct lattice plane distances to the four rings and compares them to the ones found in GIXRD. (The peak angles in GIXRD can also be converted into lattice plane distances.) Allowing a divergence of up to 0.1 nm the four rings can be correlated to the four reflexes observed in GIXRD and also to the most intense reflexes expected for cubic HfO_2. Hence, also electron diffraction points out that $Hf_{0.8}Lu_{0.2}O_{2-\Delta}$ crystallizes in a higher-κ phase of HfO_2, probably the cubic one.

The SiO_2 interfacial layer thickness of roughly 2.5 nm in the TEM image in Fig. 4.24 is again higher than the one of 1.4 nm found by fitting the *CET* plot data points in Fig. 4.12.

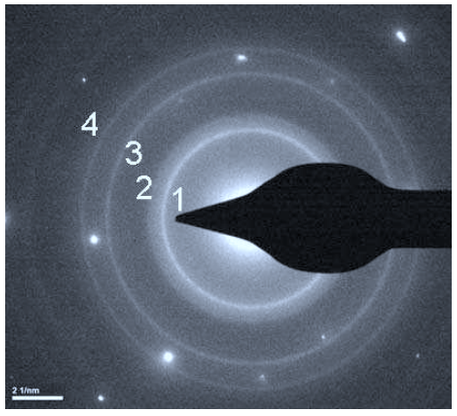

Figure 4.25: Electron diffraction pattern of $Hf_{0.8}Lu_{0.2}O_{2-\Delta}$. Four rings numbered from 1 to 4 with decreasing intensity are visible, whereupon the second ring might also be seen as a 'smearing out' of the first ring towards smaller lattice distances.

Ring	d_{TEM} (nm)	d_{GIXRD} (nm)	d_{cub} (nm)	Reflex
1	2.90	2.92	2.95	(111)
2	2.47	2.56	2.56	(200)
3	1.75	1.8	1.81	(220)
4	1.48	1.52	1.54	(311)

Table 4.5: Lattice distances extracted from electron diffraction and GIXRD for $Hf_{0.8}Lu_{0.2}O_{2-\Delta}$ in comparison to the most intense reflexes expected for cubic HfO_2 [75].

4.7 Discussion

The results presented in this chapter regard the doping of HfO_2 with Al, Lu, Er and La and the resulting permittivity and crystallinity of the oxides.

Before starting the discussion about the main topic - the relation between the permittivity and the crystal structure of the oxides - the interfacial SiO_2 layer is shortly treated.

The thickness of the interfacial layer is crucial regarding scaling since it limits the maximum achievable capacitance of a MOS stack. Interfacial layer thickness was extracted by TEM imaging and by fitting CET plots. Both methods run the risk to give ambivalent results. In TEM effects from a slight defocusing might be confused with SiO_2 layers. Further, the high energetic electron beam can alter the specimen during measurement.

CET-plots offer the possibility to determine the interfacial layer thickness by electrical measurements. It is assumed that the Hf based oxide is homogeneous. In the case of an inhomogeneous top layer, the extrapolated interfacial layer thickness would be false. Though the linear course of the measured data here points out that the layers are homogeneous and that the interfacial layer thicknesses can be trusted.

Considering the interfacial layer thicknesses from the CET plots in the following discussion, the SiO_2 thicknesses for pure and doped HfO_2 vary between 1.1 nm and 1.5 nm, whereupon there is a tendency for polycrystalline films to have thicker SiO_2 than the amorphous ones weakening the positive effect of the higher κ on the total EOT. In the case of Lu doped HfO_2 the process time could be crucial. Even though the ozone pulse and purge times are comparable in the processes, due to large volume of the deposition chamber it is possible that not all oxygen is purged out when the Lu precursor pulse starts and since the Lu precursor pulse is much longer than the one of Hf in a typical HfO_2 process there is a long time period for the residual oxygen to diffuse through the oxide to the Si interface and oxidize it. This would also explain why the pure Lu_2O_3 growth rate does not saturate for high exposure times, cf. Subsection 3.1.2. No saturation also means that the ALD growth is not in ideal ALD mode. To prevent an ongoing oxidation a more efficient purge would be needed after the ozone pulse.

Another explanation for the increased SiO_2 interfacial layer thickness could be an enhanced oxygen conductivity in the oxide. Substituting Hf^{4+} with trivalent dopants like Lu^{3+} and Al^{3+} promotes the formation of oxygen vacancies which give rise to a strongly enhanced oxygen conductivity [109]. Thus during each deposition cycle oxygen from the ozone could easily diffuse to the oxide/Si interface.

For further device scaling in the future, the SiO_2 thickness has to be reduced. There are different possible approaches: changing the cleaning of the Si surface before oxide deposition, introducing passivation layers below the HfO_2 that stop oxygen diffusion, choosing a different deposition technique without the highly reactive ozone or reducing the SiO_2 thickness afterwards by scavenging [110, 111].

Respective the relative permittivities, $Hf_{0.9}Al_{0.1}O_{2-\Delta}$ layers annealed after deposition showed high κ up to 30. As discussed in the introduction it is expected that the en-

hancement is related to a phase transformation. GIXRD measurements (Fig. 4.18) help to resolve this question.

The sample without annealing seems to be amorphous and therefore has the lowest κ of 19. The samples annealed at 600°C and 700°C show higher measured permittivity ($\kappa = 26-30$) and show predominantly the cubic phase in GIXRD which is supposed to be a higher permittivity phase compared to amorphous HfO_2 [72, 80]. At 800°C the monoclinic part in the sample increases and the permittivity decreases to 24. This fits expectations because pure monoclinic HfO_2 has a similar permittivity to amorphous HfO_2 [82]. Even when interpreting the red-shaded peaks in Fig. 4.18 as tetragonal or orthorhombic phase, the conclusions would be congruent because also for these two phases a higher permittivity is expected than for monoclinic or amorphous HfO_2 [80, 112]. For simplicity one can distinguish between low permittivity HfO_2 phases, i.e. amorphous and monoclinic HfO_2, and high permittivity HfO_2 phases, i.e. cubic, tetragonal and orthorhombic HfO_2.

TEM gives some more insights into the $Hf_{0.9}Al_{0.1}O_{2-\Delta}$ layers annealed at 700°C: While XRD shows reflections fitting to a higher-κ phase, TEM shows grains that fit to the monoclinic phase of HfO_2. Most probably a mixed phase is present.

The results on $Hf_{0.9}Al_{0.1}O_{2-\Delta}$ can be compared to the investigations of Park and Kang on HfO_2 doped with roughly 6 at.% Al. Samples annealed at 700°C showed a relative permittivity $\kappa = 47$ [65]. In contrast to the work presented here, the films were rather thick (100 nm) and therefore the crystallization behavior might be different. The authors claim that they can stabilize pure tetragonal HfO_2 [65]. This endorses the assumption made for the layers presented here that they consist of a mixed phase because otherwise a higher κ would be expected.

The presence of the mixed phase also suggests that as expected from literature [72] the shorter bonds to Al reduce the difference in energy of formation between the monoclinic and the tetragonal or cubic phase.

In the cases of $Hf_{0.8}Lu_{0.2}O_{2-\Delta}$ and $Hf_{0.89}Er_{0.11}O_{2-\Delta}$ high permittivities of 33 and 32, respectively, were achieved without any additional annealing after oxide deposition. The high κ correlates with the fact that in GIXRD and TEM (see Figs. 4.18 and 4.23) a most likely cubic structure was identified and no monoclinic compounds were observed.

The fact, that the doped HfO_2 crystallizes directly during deposition in a higher κ phase is almost unique compared to other works presented in literature. While studies on Lu doped HfO_2 are not known to the author, investigations of Er doped HfO_2 also showed an enhancement of the permittivity but only after annealing at 800°C or higher [71, 96, 109, 113]. There exists one example of Er doped HfO_2 grown by ALD where also the tetragonal phase was present directly after the deposition but the best κ of 33 was only observed after a PDA of 900°C [71]. Also doping with other atoms typically requires post deposition annealing to increase the permittivity [97]. The possibility to grow high κ films at 300°C without a post oxide deposition annealing is a huge advantage for certain applications especially when high temperature anneals have to be avoided to hinder diffusion like when using GeSn substrates [22].

In contrast, for $Hf_{0.89}La_{0.11}O_{2-\Delta}$ no increased κ was observed for oxide layers without annealing: the relative permittivity unfolds to 19. TEM gives an explanation for this

low permittivity (cf. Fig. 4.23): the observed layer is clearly amorphous explaining a permittivity equal to the one of amorphous HfO_2. Probably a post deposition annealing at higher temperatures is needed to increase κ for $Hf_{1-x}La_xO_{2-\Delta}$, as shown by Toriumi et al. [114].

The results confirm the expectation that the phase of the oxide is the essential factor to increase the permittivity and that doping and an enhancement of the surface and interface area due to thin films and small grain sizes changes the favored phase from monoclinic to tetragonal or cubic matching the results in [72–74, 85, 115].

Additionally to doping, also oxygen vacancies and carbon incorporation from the precursor molecules might support the reduction of the grain sizes [116, 117]. For example oxygen vacancies $V_O^{\cdot\cdot}$ are introduced when replacing the tetravalent Hf^{4+} cations by trivalent rare earth RE^{3+} cations [65, 72]. Also calculations based on a self-consisting tight-binding model on ZrO_2 (knowledge about ZrO_2 is often transferred to HfO_2 because the two materials are very similar, especially their behavior respective phase transitions [76, 84, 88, 112]) demonstrate that the introduction of oxygen vacancies (without introduction of dopants) leads to a stabilization of the tetragonal or cubic phase instead of the monoclinic one [98].

A question that remains is why $Hf_{0.8}Lu_{0.2}O_{2-\Delta}$ and $Hf_{0.89}Er_{0.11}O_{2-\Delta}$ crystallize directly during deposition while $Hf_{0.89}La_{0.11}O_{2-\Delta}$ stays amorphous.

The origin is probably found in the deposition process. While the precursor molecules of Hf, Al and La saturate the surface rather quickly during the ALD process, the Lu and Er precursors have very low vapor pressures and do not saturate the surface even after 150 second pulses. As mentioned above maybe residual oxygen hinders the saturation. It is also possible that the bonds between the metal atom and the rest of the organic precursor do not break as intended and that carbon is incorporated which would explain the enhanced C content observed by SIMS. In any case the unsaturated surface might offer nuclei for the formation of small crystalline grains. Following this approach the grain size would be determined by the number of nuclei.

Other than for carbon incorporated into ZrO_2 investigated by Cho et al. [117] in the films presented here the carbon does not deteriorate the electrical properties.

Another specialty in the process is the use of O_3 instead of H_2O as oxygen source during ALD. Due to the high reactivity of ozone the reactions are expected to be fast suppressing an equilibrium growth mode and assisting the formation of nuclei for crystallites. A similar effect was seen for ZrO_2 grown by ALD: the ratio between tetragonal and monoclinic parts was enhanced by using O_3 instead of H_2O as oxidizing precursor [98].

Respective leakage current densities presented in Fig. 4.17 it is worth to note that the polycrystalline doped HfO_2 layers are equally good or even outperform pure HfO_2. Often amorphous oxides are preferred compared to polycrystalline ones because it is suspected that grain boundaries build up leakage paths and enhance the leakage currents. This is not an issue for the doped oxides presented here and also other groups demonstrated that the leakage through HfO_2 is not increased due to crystallization of the films [72, 118].

Pure HfO_2 and $Hf_{0.9}Al_{0.1}O_{2-\Delta}$ show the same trend in leakage current as a function of *EOT* and this trend can be attributed to tunneling. This means that the effects of an

enhanced permittivity and enlarged leakage currents for a given thickness cancel each other out in terms of dielectric properties. The increase in leakage current for a given thickness in the Al doped HfO_2 correlates either to a decreased band gap, to a lowered effective electron mass or to a higher defect density. All of these three factors would contribute to higher tunneling probabilities.

The leakage currents through $Hf_{0.8}Lu_{0.2}O_{2-\Delta}$ as a function of EOT do not show an exponential increase for decreasing EOT down to an EOT of 1.5 nm thus direct or Fowler-Nordheim tunneling did not set in yet. Since the band gap differs only slightly by ca. 0.1 eV between pure HfO_2 and $Hf_{0.8}Lu_{0.2}O_{2-\Delta}$, possibly a higher effective mass for $Hf_{0.8}Lu_{0.2}O_{2-\Delta}$ reduces the tunneling probability and keeps the leakage currents low.

4.8 Summary

The successful development of ALD processes to deposit doped HfO_2 was reported. Primary focus was the doping of HfO_2 with Al and Lu and thus the ALD processes were optimized respective the maximum achievable permittivity. $Hf_{0.9}Al_{0.1}O_{2-\Delta}$ demonstrated a high relative permittivity of 30 for a post deposition annealing at 700°C which is higher than for pure HfO_2 showing $\kappa = 18$. For $Hf_{0.8}Lu_{0.2}O_{2-\Delta}$ even a higher κ of 33 was achieved without additional annealing procedures, which is unique among the doped HfO_2 layers. While doping with La did not lead to an increase of the permittivity, for Er doping without PDA a similar behavior as for Lu was found: $Hf_{0.89}Er_{0.11}O_{2-\Delta}$ demonstrated a κ of 32.

By plotting the leakage current densities of various oxides as a function of EOT the good insulating properties of doped HfO_2 were confirmed. $Hf_{0.9}Al_{0.1}O_{2-\Delta}$ and $Hf_{0.8}Lu_{0.2}O_{2-\Delta}$ show leakage current densities of $4\times10^{-5}\,A/cm^2$ and $3\times10^{-7}\,A/cm^2$ at an EOT of 1.5 nm, respectively. Hence, $Hf_{0.8}Lu_{0.2}O_{2-\Delta}$ outperforms various binary and ternary oxides, among them HfO_2, for $EOT = 1.5$ nm. Further, as observed by other groups for pure HfO_2 [118], the leakage currents through the doped HfO_2 were not enlarged due to the polycrystallinity.

Additionally the band gap of $Hf_{0.8}Lu_{0.2}O_{2-\Delta}$ was determined by ellipsometry. In comparison to HfO_2 deposited with a very similar ALD process (just without opening the Lu precursor line) the band gap was increased by 0.1 eV to 5.8 eV.

$Hf_{0.9}Al_{0.1}O_{2-\Delta}$ demonstrated slighty lower density of interfacial traps than $Hf_{0.8}Lu_{0.2}O_{2-\Delta}$. Yet, all investigated stacks revealed D_{it} smaller than $2 \times 10^{12}\,eV^{-1}cm^{-2}$ which is still appropriate for devices.

Flat band voltages shifted in comparison to pure HfO_2 depending on doping and annealing, but these shifts stay below 0.5 V.

The structural investigations gave an explanation for the augmentation of the permittivity: For $Hf_{0.9}Al_{0.1}O_{2-\Delta}$ annealed at 700°C the high permittivity has its origin in the polycrystallinity of the films with a large fraction of high-κ phases of HfO_2, most probably the cubic form. The permittivity decreased for higher anneal temperatures because the monoclinic ratio in the film increased which has a lower permittivity than the other crystalline phases. Also for $Hf_{0.8}Lu_{0.2}O_{2-\Delta}$ the observed reflections fit to higher κ phases of HfO_2. The crystallites observed in TEM were even smaller than for Al doped HfO_2 with

grain sizes in the range of 10 nm.

TEM images and AFM demonstrated that all doped HfO_2 films are smooth with *rms* roughnesses of 0.5 nm and below.

Even though doped HfO_2 deposited in an ozone based ALD process offers films with excellent dielectric properties, for further device scaling additional process development steps are needed: it has to be tested whether the oxides are polycrystalline for even thinner films and the interfacial layer thickness should to be decreased e.g. by scavenging processes.

In conclusion three forms of doped HfO_2 grown by ALD with a high κ (30-33) and low leakage currents were presented. Hence, the smooth polycrystalline films are suitable for the use as Hf based gate dielectric in Si nanotechnology. Two of the materials - Lu and Er doped HfO_2 - even reached the high permittivity with a thermal budget not higher than 420°C, the temperature used during gate metal deposition, and therefore they are also promising candidates for the use in devices demanding a low thermal budget.

5 Epitaxial oxides on GaN

While silicon is the basis for standard microelectronics such as transistor chip technology using small voltages, for certain specific applications other semiconductors are more suitable. The band gap width of III-V semiconductors can be adjusted by their composition and thus be optimized for various applications. The hexagonal III-nitrides, for example, can cover an energy gap range between 1.9 eV (pure InN) up to 6.2 eV (pure AlN) [119], compare Fig. 5.1.

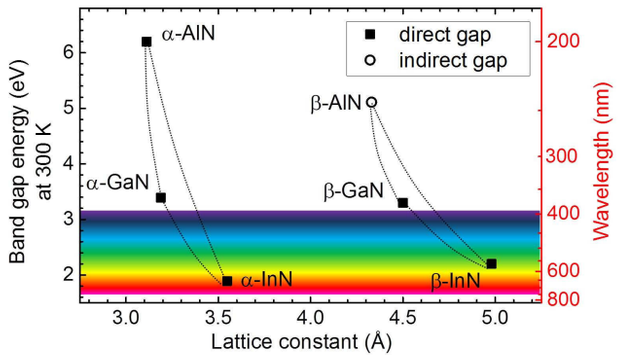

Figure 5.1: Band gap (left axis) and wavelength (right axis) as a function of lattice constant for cubic (β-) and hexagonal (α-) InN, GaN, AlN and their compounds. Data points taken from [120]. The regime used for visible light is marked by the colored region.

Other than Si or GaAs, III-nitrides' performance does not suffer from elevated temperatures or caustic environments and thus III-nitrides are interesting for high-temperature and high-power electronics [121, 122]. Further AlGaN layers on GaN can form two dimensional electron gases at the interface resulting in greatly enhanced electron mobilities which are needed for high electron mobility transistors (HEMTs) [13].

All these III-V devices need appropriate dielectrics and passivation layers. Adopting the knowledge gained for Si transistor technology amorphous Al_2O_3 and HfO_2 are often used for III-V HEMTs [123–125] but also many other materials are investigated [126–129].

Typically amorphous oxides are chosen because the growth conditions are easy to find and because dislocations and other defects in epitaxial oxides might create pathways for unwanted leakage currents. On the contrary, if such leakage effects can be prevented,

epitaxial oxides can offer superior properties such as higher permittivity, larger band gap or reduced defect densities at the oxide semiconductor interface [130–133]. For example using lattice matched oxides Wang et al. demonstrated that it is possible to reduce the density of interfacial traps of La_2O_3 on GaAs (111) down below $3 \times 10^{11}\,\mathrm{cm}^{-2}\mathrm{eV}^{-1}$ near the conduction band edge [133].

An oxide for the application as gate dielectric needs to have a high permittivity κ to ensure good gate control and good insulating properties, i.e. low leakage currents at specified voltages and high breakdown electric fields, which is particularly important for high power applications. Furthermore the oxide thin films should have low densities of interface and oxide traps, should be smooth and should be stable in contact with the substrate and with the electrodes.

For future devices it would also be great to be able to have different transistor types on one chip, i.e. to integrate III-V semiconductors on a silicon substrate. It is not possible to grow high quality GaN directly on Si due to a high thermal and lattice mismatch and because Ga reacts with Si [134]. Tarnawska et al. presented an approach to overcome these problems introducing a passivating buffer layer consisting of epitaxial Y_2O_3 and Sc_2O_3 between Si (111) and GaN [39]. Also for the application as a buffer the oxide films need to have low surface roughnesses and good insulating properties and must not react with either GaN or Si.

The approach here is to use epitaxial oxides - $GdScO_3$ and $LaLuO_3$ - as either gate dielectric on top of GaN or as a buffer beneath GaN, e.g. when GaN is integrated on Si.

Therefore $GdScO_3$ and $LaLuO_3$ were deposited by pulsed laser deposition on two different growth templates. On the one hand the aim was to investigate how the growth conditions, such as temperature and substrate, influence the crystal formation and to find the structural characteristics of the oxides, such as the crystal structure and crystallinity. On the other hand it was evaluated whether these polymorphs are suitable as gate dielectric on GaN based devices or as buffer layer on Si.

The first two sections in this chapter introduce the growth templates and the oxides. In the following sections the growth of $GdScO_3$ and $LaLuO_3$ on the different templates is investigated. For different layer thicknesses and substrate temperatures the phases are identified and if necessary characterized in more detail. Section 5.6 treats the dielectric characterization of the present $GdScO_3$ and $LaLuO_3$ polymorphs to evaluate the permittivity and the insulating properties. In an excursus in Section 5.7 the effects of hexagonal $LaLuO_3$ on the GaN characteristics are explored.

5.1 Growth templates

Two growth templates were chosen in this work for the epitaxial growth of oxides:

- **GaN** - α-GaN was deposited by MOVPE on sapphire substrates. α-GaN is the hexagonal form of GaN and it was oriented in the (0001) orientation (Ga-faced), compare Fig. 5.2. The GaN lattice constants are $a = 0.3189\,\mathrm{nm}$ and $c = 0.5185\,\mathrm{nm}$

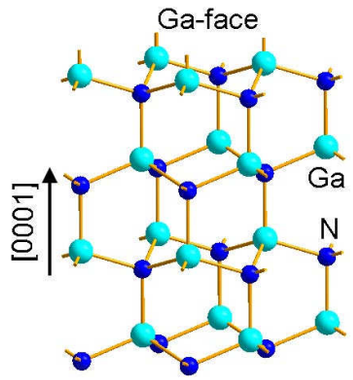

Figure 5.2: Schematics of the crystal structure of Ga-faced wurtzite GaN. Drawing made with *Diamond* [135].

[119]. GaN thicknesses ranged between 1.5 μm and 8 μm. Due to the large lattice mismatch between sapphire and GaN, GaN typically exhibited misfit dislocations that are present as pin holes on the surface.

- **Y_2O_3/Si -** Thin layers of Y_2O_3 were deposited on Si by molecular beam epitaxy. Both materials were cubic with the (111) direction parallel to the surface normal. Bulk Y_2O_3 exhibits a slightly smaller lattice constant ($a_{YO} = 10.6\,\text{nm}$ [39]) than the doubled lattice constant of Si ($a_{Si} = 5.43\,\text{nm}$ [16]). The mismatch between a_{YO} and $2a_{Si}$ is around 2.4% and allows epitaxial overgrowth. Y_2O_3 thicknesses ranged from 1 nm to 30 nm. The Y_2O_3 served as an auxiliary layer during PLD epitaxy. Due to the high oxygen ambient in the growth chamber during PLD (oxygen partial pressure $\geq 10^{-3}$ mbar), bare Si would have immediately oxidized and would have hindered epitaxial overgrowth. One disadvantage of this stack is the temperature stability. At temperatures around 650°C Y_2O_3 and Si started to form a silicate[136] and thus at high deposition temperatures an amorphous interlayer formed.

The growth templates showed either a sixfold or a threefold symmetry along the surface and thus we define that they both have an in-plane hexagonal geometry. This is also visualized in Fig. 5.3.

5.2 $GdScO_3$ and $LaLuO_3$

The most widely known phases of $GdScO_3$ are the amorphous and the orthorhombic one. Both belong to the high-κ oxides with relative permittivities of 23 and 19-30 (depending on the lattice orientation), respectively [7, 137].

Various techniques, such as electron beam evaporation and atomic layer deposition [137–139], were used to deposit thin films of amorphous $GdScO_3$ and it was success-

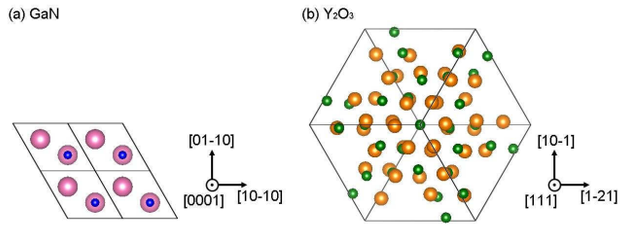

Figure 5.3: Schematic of (a) 4 unit cells of GaN (0001) and (b) 1 unit cell of Y_2O_3 (111). Colors: Ga - blue, N - rose, Y - green, O - orange. The drawings were made using *VESTA* [86].

fully integrated into devices, e.g. in Si MOSFETs, AlGaN/GaN heterojunction FETs and InAlN/GaN high electron mobility transistors [126, 128, 140].

The orthorhombic phase is the stable bulk crystal phase of $GdScO_3$. In 1926 Goldschmidt presented a rule to distinguish between the different possible crystal forms of perovskites of the form ABX_3 with R_A, R_B and R_X the ion radii of the respective elements [141]. If the Goldschmidt tolerance factor t

$$t = \frac{1}{\sqrt{2}} \frac{R_A + R_X}{R_B + R_X} \tag{5.1}$$

lies between 0.75 and 0.9 the orthorhombic form in the space group *Pbnm* (No. 62) is favored [142]. With $t = 0.81$ [143] $GdScO_3$ falls into this category. Orthorhombic $GdScO_3$ can either be synthesized as bulk crystal using the Czochralski growth [144, 145] or deposited as thin films on various substrates such as $LaAlO_3$, $SrTiO_3$, $BaTiO_3$/MgO or $SrRuO_3/SrTiO_3$ [146–148].

During this work two more phases of $GdScO_3$ were discovered and will be presented here in detail. Part of the results are already published in [149, 150].

Lanthanum lutetium oxide also belongs to the versatile group of higher-κ materials. Four polymorphs are known for $LaLuO_3$, i.e. the amorphous, orthorhombic, cubic and hexagonal one [10, 132, 151–153], even though the hexagonal phase is only mentioned on the sideline of a comparative work on Nd_2O_3 [153].

Amorphous $LaLuO_3$ revealed a high κ of up to 32 [151] and was used as gate dielectric on strained silicon on insulator devices, on AlGaN/GaN high electron mobility transistors and on InAs nanowires [129, 154, 155].

The stable bulk form of crystalline $LaLuO_3$ is the orthorhombic form and belongs to the *Pbnm* space group just like $GdScO_3$. Orthorhombic $LaLuO_3$ can be synthesized as bulk [156, 157] or as thin films on various substrates such as $SrTiO_3$, $SrRuO_3/SrTiO_3$ and $SrRuO_3/LaAlO_3$ [10]. The cubic form of $LaLuO_3$ could be stabilized on Si (111) and GaAs (111) [132, 152, 158]. The cubic crystal structure was explored by Niehle et al. using HRTEM [159]. While cubic $LaLuO_3$ demonstrated a relative permittivity of 30 [132], the highest κ of up to 50 was found for orthorhombic $LaLuO_3$ deposited on $SrRuO_3$ [10].

5.3 Structural characterization of epitaxial $GdScO_3$

5.3.1 Epitaxial $GdScO_3$ on GaN

RBS measurements were performed on $GdScO_3$ grown on GaN at 620°C to get a first impression of the thickness, stoichiometry and crystal order of the oxide layer, see Fig. 5.4. A simulation that fits the random spectrum best reveals a stoichiometry of ca. 1:1 for Gd:Sc and a thickness of 20 nm. Putting the channeling signal in relation to the random signal for Gd gives a minimum yield of 60 %. The fact that there is a channeling signal present which is significantly smaller than the random one implies that there is some crystal order present in the oxide film.

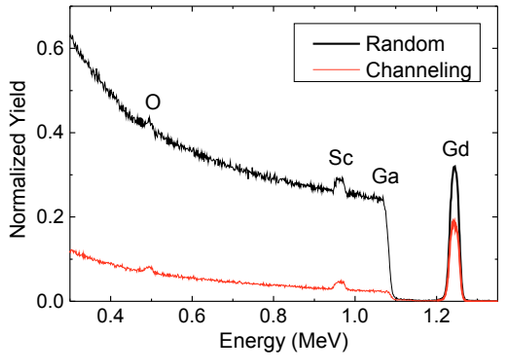

Figure 5.4: RBS measurement of $GdScO_3$ grown on GaN. A simulation of the random signal reveals a $GdScO_3$ layer thickness of 20 nm and a stoichiometry of Gd:Sc of about 1:1. The minimum yield of the Gd channeling signal in relation to the random Gd signal is 60 %.

In the following sections the oxygen to metal atomic content is assumed to be 3:2 because the metals have a cation valence of 3 and oxygen has an anion valence of 2. This is done for convenience because it is difficult to determine the exact oxygen content. For example in the RBS spectra in Fig. 5.4, the oxygen content almost vanishes due to the intense signal of Ga.

Atomic force microscopy (AFM) measurements of a $GdScO_3$ layer grown on GaN, see Fig. 5.5, reveal that the layers are very smooth with an *rms* roughness of 0.4 nm [149]. Furthermore, atomic steps are visible in the image. These steps are typical for GaN on sapphire (cf. [160]) and the $GdScO_3$ seems to preserve these steps indicating conformal growth.

XRD measurements were carried out in order to characterize the crystal order of $GdScO_3$. In Fig. 5.6 (a) a θ-2θ scan in the out of plane direction is presented. Besides the peaks belonging to GaN and sapphire two reflections are present that can only originate from

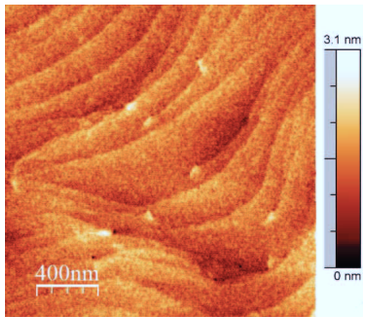

Figure 5.5: AFM of $GdScO_3$ grown on GaN at 620°C.

$GdScO_3$ and correspond to the (0002) and (0004) reflections of hexagonal $GdScO_3$ as will be demonstrated further on.

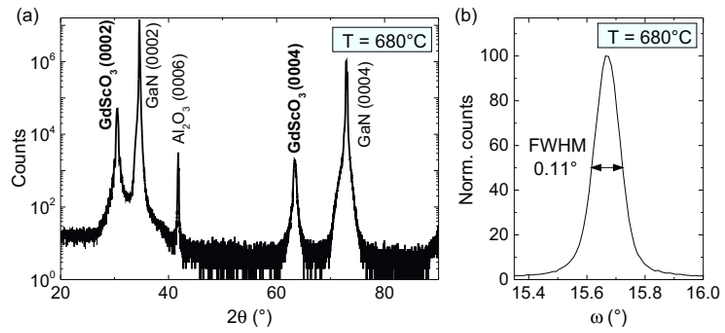

Figure 5.6: XRD of $GdScO_3$ grown on GaN at 680°C: (a) θ-2θ scan in the out of plane direction; (b) Rocking curve around (0002) reflex of $GdScO_3$.

A rocking curve around the $GdScO_3$ (0002) peak in Fig. 5.6 (b) displays a $FWHM$ of 0.11° which is in the same range as the underlying GaN with a $FWHM$ of the corresponding rocking curve of 0.1° [149]. Hence, the crystallinity of the films seems to be limited by the crystallinity of the growth template.

Fig. 5.7 demonstrates the growth temperature dependence of the $GdScO_3$ crystalline films. The XRD θ-2θ scans in the out of plane direction for the first $GdScO_3$ and GaN peak presented in the left part of the figure show a congruent pattern for temperatures between 620°C and 740°C. The position of the $GdScO_3$ reflection hardly changes and all three layers show thickness oscillations around this peak which illustrates that the layers are smooth as was already deduced from AFM. The XRD pattern changes for the layer grown at 860°C. A second peak appears, the intensity decreases and the thickness oscillations vanish. Thus

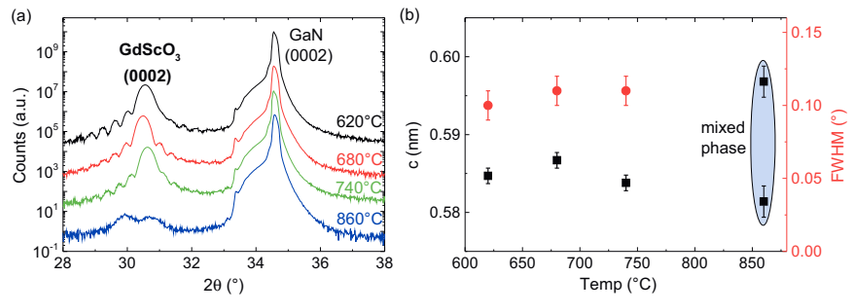

Figure 5.7: (a) XRD θ-2θ scan of $GdScO_3$ grown on GaN for different temperatures. The layers grown at 620°C, 680°C and 740°C show thickness oscillations around the (0002) reflection of $GdScO_3$ at 30.49°. (b) Lattice constants derived from $GdScO_3$ (0002) and (0004) peak positions (black squares, left axis) and $FWHM$ of the rocking curves derived from $GdScO_3$ (0002) reflexes (red circles, right axis) as a function of temperature.

in this deposition temperature regime there seems to occur a phase transition. The lattice constants deduced from the XRD scans by applying a Nelson-Riley plot [54] to the (0002) and (0004) reflections are plotted as a function of temperature in Fig. 5.7 (b). The out of plane lattice constant c lies between 0.58 nm and 0.59 nm, the additional reflex for the layer grown at 860°C corresponds to an out of plane lattice distance of 0.597 nm. As shown in red, the single crystalline layers all exhibit a $FWHM$ of the rocking curve between 0.1° and 0.12°.

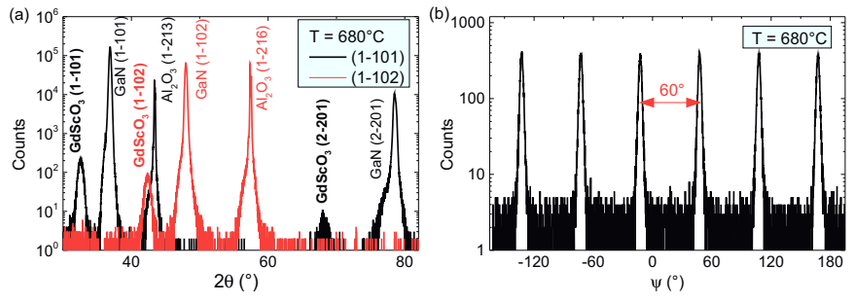

Figure 5.8: (a) XRD $\theta - 2\theta$ scan around $GdScO_3$ (1-101) and (1-102) reflections. (b) XRD ψ scan around $GdScO_3$ [1-101] direction adapted from [149]. The $GdScO_3$ layer was deposited at 680°C.

Assuming a hexagonal lattice with an in plane lattice constant a of 0.36 nm and an out of plane lattice constant c of 0.585 nm θ-2θ scans were made in the [1-101] and [1-102] direction

of $GdScO_3$ presented in Fig. 5.8 (a). Besides GaN and Al_2O_3 reflections $GdScO_3$ (1-101), (2-201) and (1-102) reflections can be found confirming the assumption that a hexagonal lattice is present. The existence of a hexagonal lattice is further confirmed by the ψ scan around the (1-101) reflex of $GdScO_3$ shown in Fig. 5.8 (b). The six peaks for the scan over 360° can be correlated to the sixfold symmetry of a hexagonal lattice.

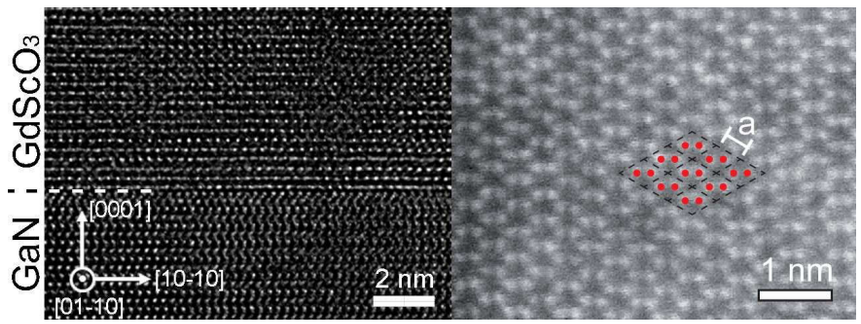

Figure 5.9: TEM images of hexagonal $GdScO_3$ on GaN adapted from [150] . Left: HRTEM cross section image showing GaN and $GdScO_3$ and their interface. Right: plan view STEM image. Unit cell used to determine the in plane lattice constant of hexagonal $GdScO_3$ is marked.

Transmission electron microscopy was also carried out to analyze the $GdScO_3$ crystalline layers. Fig. 5.9 presents a cross section image of $GdScO_3$ grown on GaN and a plan view image of $GdScO_3$. In the cross sectional image one can see that the interface to GaN is atomically smooth within the area under inspection. In some regions the contrast is slightly blurred which probably arises from orientation variations due to structural defects. Furthermore the $GdScO_3$ is clearly single crystalline, but the lattice type cannot be deduced. In contrast, the plan view image nicely shows the in plane hexagonal structure of $GdScO_3$. The bright spots have all the same intensity and result from the metal atoms. Oxygen can be excluded because only the elements with high atomic number are visible. Since all bright spots have the same intensity there have to be Gd and Sc atoms stacked on top of each other. Otherwise different intensities would be expected due to the different atomic numbers of Gd and Sc.

A $GdScO_3$ unit cell is marked in the right part of Fig. 5.9 from which an in plane lattice constant of 0.36 nm could be deduced.

The electron diffraction pattern in the [01-10] zone axis of the cross section TEM sample of $GdScO_3$ grown on GaN in Fig. 5.10 gives more insight into the crystal order. Intense spots belong to GaN, weaker ones to $GdScO_3$. The $GdScO_3$ spots are located next to the GaN spots but shifted towards smaller radii which correspond to larger lattice constants in the direct lattice compared to GaN. The positions of the spots confirm coherent growth of the $GdScO_3$ on GaN and the (2-1-10) and (0002) spots for both materials can be assigned.

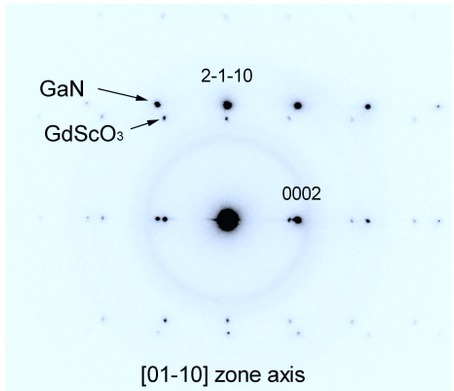

Figure 5.10: TEM electron diffraction pattern in the [01-10] zone axis of hexagonal $GdScO_3$ on GaN [149]. Intense and weak spots correspond to GaN and $GdScO_3$, respectively. (2-110) and (0002) reflections of $GdScO_3$ and GaN are marked in the figure.

Using the known lattice constants of GaN as calibration, lattice constants of a = 0.36 nm and c = 0.584 nm can be extracted from the electron diffraction which correspond nicely to the ones deduced from XRD and direct TEM imaging.

5.3.2 Alternative growth template for $GdScO_3$: Y_2O_3/Si

Since native GaN substrates are difficult to obtain [122], GaN is typically grown as layers on substrates appropriate for epitaxial growth. Unfortunately, these layers exhibit defects that may limit electrical characteristics even though the GaN crystallinity continuously improved over the years (cf. [44, 119, 120]). For example pin holes in the GaN may hinder the conformal overgrowth with an oxide and may create centers for leakage currents.

Capacitance voltage measurements on GaN are generally possible (see Section 5.6.2), but in this work only limited data could be extracted from measurements on GaN because for many contacts either the capacitance did not reach its maximum due to leakage issues or the CV course was stretched out due to defects.

The oxide epitaxy on Y_2O_3/Si is not only explored to test the approach to use these oxides as buffer between Si and GaN, but also to be able to perform the electrical characterization of the oxide properties on Si. That way there is no need to account for effects induced by the growth template when analyzing the electrical data, since bulk Si can be grown in perfect crystals.

First, characterization of $GdScO_3$ grown on Y_2O_3/Si is done by XRD θ-2θ scans in the out of plane direction for different Y_2O_3 thicknesses, see Fig. 5.11.

Surprisingly, the peak positions of $GdScO_3$ for 1 nm and 7 nm thin Y_2O_3 differ. For the

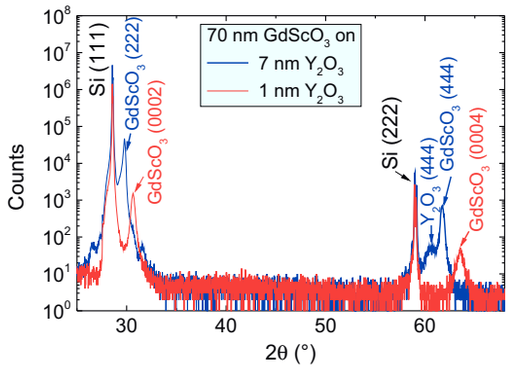

Figure 5.11: XRD θ-2θ scan in the out of plane direction of $GdScO_3$ grown on Y_2O_3/Si at 550°C for Y_2O_3 layer thicknesses of 7 nm and 1 nm. $GdScO_3$ forms a cubic structure on 7 nm Y_2O_3 (blue) and a hexagonal structure on 1 nm Y_2O_3 (red).

very thin Y_2O_3, the $GdScO_3$ reflection at 30.6° corresponds to the peak position observed for $GdScO_3$ (0002) on GaN. Thus $GdScO_3$ grows hexagonally for very thin Y_2O_3. For thicker Y_2O_3 the $GdScO_3$ peak position shifts to smaller angles (29.8°) which correlates to a larger out of plane lattice distance. This is also true for XRD θ-2θ scans in the out of plane direction for $GdScO_3$ on Y_2O_3 layers with thicknesses of 5 nm or 30 nm (not shown here).

In the case of hexagonal $GdScO_3$ on thin Y_2O_3 the crystallinity seems to be degraded. Apart from the (0002) and (0004) reflection observed in Fig. 5.11, reflections in other directions can hardly be found. Possibly the layer consists of hexagonal grains that are oriented with their c-axis along the normal of the surface, but disordered respective the in plane lattice directions.

A TEM image of hexagonal $GdScO_3$ grown on 1 nm Y_2O_3 on Si(111) is presented in the left part of Fig. 5.12. In the top part one clearly sees the crystalline $GdScO_3$, but the planes seem rippled and towards the interface to Si the $GdScO_3$ becomes amorphous. Furthermore at the interface to Si a SiO_2 layer of about 4 nm forms. Since the lattice planes of $GdScO_3$ are practically parallel to the surface like it is typical for epitaxial growth, the amorphization of $GdScO_3$ and the formation of SiO_2 probably occur during growth, but are slower than the epitaxial growth.

Energy dispersive x-ray spectroscopy (EDX) was done along the vertical direction of the TEM direct image in Fig. 5.12 to detect whether a diffusion of elements occurs. As can be seen in Fig. 5.13, Si diffuses partly into the Y_2O_3 and $GdScO_3$ and probably forms a silicate which explains the partial amorphization of the $GdScO_3$ layer. Maybe lower deposition temperatures than 550°C could attenuate the Si diffusion.

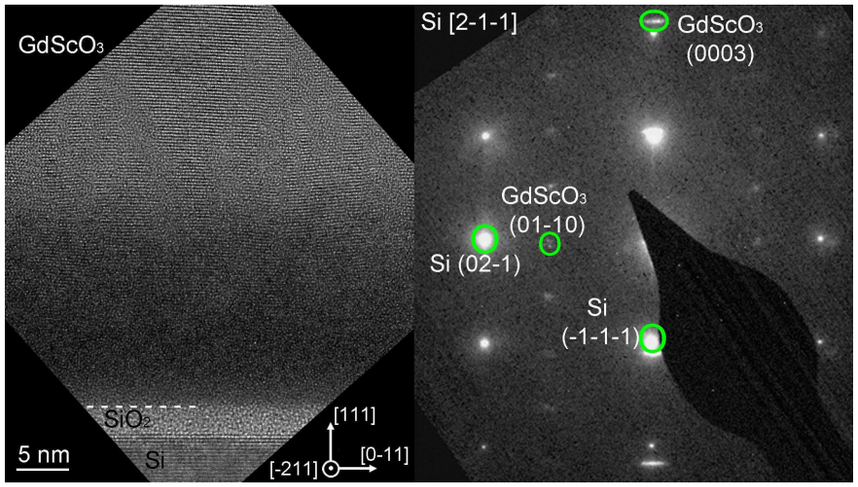

Figure 5.12: HRTEM image (left) and electron diffraction pattern (right) of 65 nm thick hexagonal $GdScO_3$ grown on 1 nm Y_2O_3 on Si(111).

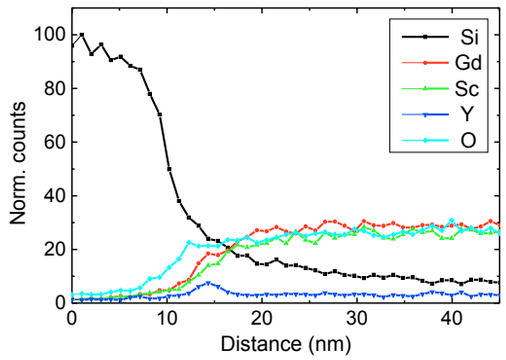

Figure 5.13: EDX line scan performed perpendicular to the interfaces of hexagonal $GdScO_3$ grown on ca. 1 nm Y_2O_3 on Si(111).

The diffraction pattern at the right of Fig. 5.12 illustrates reflections of both, Si and $GdScO_3$ which can be indexed by the known lattice type and lattice constants. The $GdScO_3$ reflections such as the (0003) reflection are elongated horizontally. This corroborates the assumption deduced from XRD that the hexagonal $GdScO_3$ grown on thin Y_2O_3 is aligned along the normal of the surface but somehow disordered parallel to the surface.

In the case of $GdScO_3$ grown on thicker layers of Y_2O_3 apparently a cubic crystal in the (111) direction forms adopting the structure of the underlying Y_2O_3. The lattice constant of cubic $GdScO_3$ is therefore $a = 1.06\,\mathrm{nm}$. The cubic symmetry is confirmed by a ψ scan around the (004) direction which exhibits a threefold symmetry, compare Fig. 5.14 (a).

The rocking curve of the $GdScO_3$ (222) reflection in Fig. 5.14 (b) discloses a $FWHM$ of 0.08° which is lower compared to the one of hexagonal $GdScO_3$ on GaN (0.1°-0.12°) but slightly higher than the underlying Y_2O_3 itself with 0.06° (cf. Fig. 5.14 (c)). The rocking curve of $GdScO_3$ shows some background below the sharp peak which is also visible somewhat weaker for Y_2O_3. In the case of Y_2O_3 it is known that the background is caused by misfit dislocations [39], so probably they continue in the $GdScO_3$ layer.

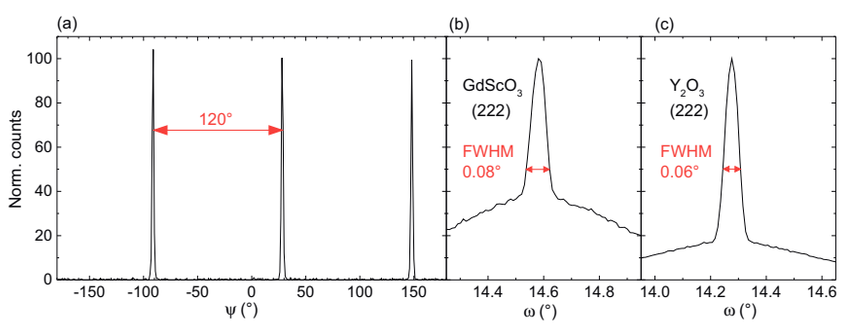

Figure 5.14: (a) XRD ψ scan around $GdScO_3$ (004) with a thickness of 70 nm grown on 7 nm Y_2O_3 on Si. (b) XRD rocking curves of $GdScO_3$ (222) and (c) XRD rocking curves of Y_2O_3 (222) for 70 nm $GdScO_3$ grown on 30 nm Y_2O_3 on Si (111). $GdScO_3$ reveals a slightly higher rocking curve width of 0.08° than Y_2O_3 of 0.06°. The background that can be seen for both rocking curves originates from misfit dislocations [39].

$GdScO_3$ layers were deposited at different substrate temperatures to investigate the influence on lattice type and crystallinity. Fig. 5.15 shows that the lattice parameter stays rather constant for a wide temperature range between 500°C and 750°C: it varies between 1.040 nm and 1.037 nm for layers with thicknesses of 50 nm and is a little higher with $a = 1.041\,\mathrm{nm}$ for a $GdScO_3$ with three times the layer thickness grown at 700°C. The

$FWHM$ (red squares in Fig. 5.15) is typically below 0.1° for cubic layers revealing good crystallinity. But there are two exceptions: for the thicker layer with 150 nm thickness and for the high temperature sample grown at 750°C the $FWHM$ goes up by more than half of the intensity due to an increased broad background . In these cases the number of defects such as misfit dislocations increases. Hence, to ensure good crystallinity the layers should be kept thin (below 50 nm) and should be deposited at temperatures below 700°C. This constraint is fulfilled for the application as gate dielectric where generally thin layers are employed.

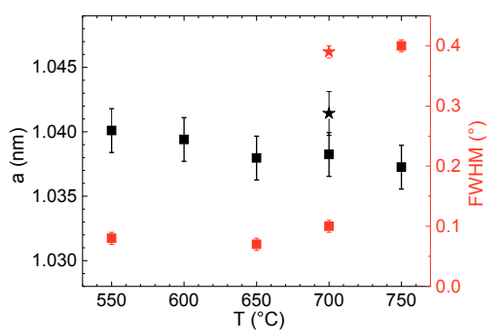

Figure 5.15: Temperature dependence of lattice constant a (left axis) of cubic $GdScO_3$ with a layer thickness of 50 nm (black squares) or 150 nm (black star) grown on 30 nm Y_2O_3 on Si and temperature dependence of the $FWHM$ of the corresponding rocking curves (right axis, red squares and star for 50 nm and 150 nm $GdScO_3$, respectively).

The coherent growth of cubic $GdScO_3$ can also be observed by TEM, see Fig. 5.16. The direct image in the left part shows a smooth interface and good crystallinity. Close to the interface the contrast changes and the image becomes darker. This occurs probably due to strain. The diffraction pattern on the right in Fig. 5.16 demonstrates how similar the lattice distances are: the bright spots belong to Si, but just a little outwards of every bright spot follow spots from Y_2O_3 and $GdScO_3$. For example the Si (111), Y_2O_3 (222) and $GdScO_3$ (222) spots and the Si (02-2), Y_2O_3 (04-4) and $GdScO_3$ (04-4) spots group together. The lattice constants derived from TEM are consistent with the ones from XRD.

The weaker reflections in between the bright spots refer to Y_2O_3 and $GdScO_3$ and fit to a bixbyite structure. For Y_2O_3 it is known that it crystallizes in the bixbyite structure. Considering that Gd_2O_3 and Sc_2O_3 also crystallize in a bixbyite lattice, probably also $GdScO_3$ does. The diffraction pattern underlines this interpretation.

Even though the above experiments aimed at reproducing the hexagonal form of $GdScO_3$ on an alternative growth template, it was discovered that this hexagonal phase can only be achieved for very thin Y_2O_3 layers. However, the studies reveal the existence of a cubic

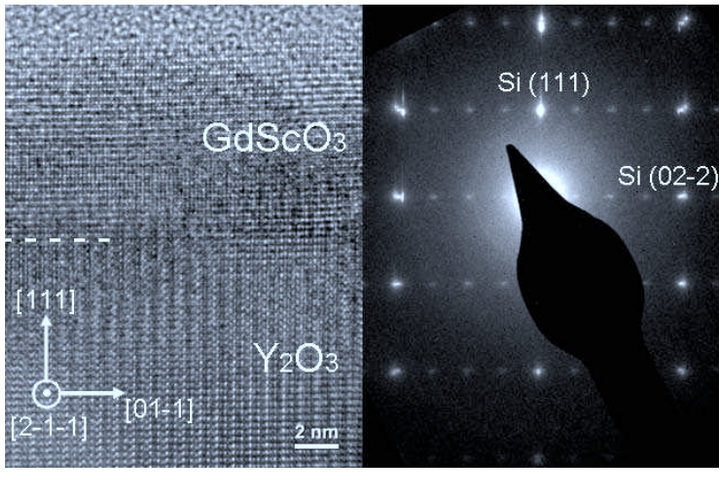

Figure 5.16: HRTEM image (left) and electron diffraction pattern in the $GdScO_3$ [2-1-1] zone axis (right) of 35 nm thick $GdScO_3$ grown on 30 nm Y_2O_3 on Si (111) adapted from [150] . The bright spots of Si (111) and Si (02-2) are marked, Y_2O_3 (222), $GdScO_3$ (222) spots and Y_2O_3 (04-4) and $GdScO_3$ (04-4) spots lie right next to the Si reflection in the outward direction.

phase of $GdScO_3$ that was not mentioned in literature before. Consequently, now four polymorphs of $GdScO_3$ are known: amorphous, orthorhombic, hexagonal and cubic. The lattice constants of the three crystalline forms are summarized in Tab. 5.1.

As mentioned already in the introduction of this chapter, this work focuses on two epitaxial oxides, namely $GdScO_3$ and $LaLuO_3$. Yet, alongside this work, also other scandates were investigated among them $SmScO_3$. Because Gd and Sm have very similar atomic number (64 and 62, respectively) and atomic weight (157 and 150, respectively) [100], also the ternary oxides $GdScO_3$ and $SmScO_3$ are quite similar: the lattice constants of orthorhombic $GdScO_3$ and $SmScO_3$ differ maximally by 0.005 nm and the respective relative permittivities are 24 and 23.8 for $GdScO_3$ and $SmScO_3$, respectively [7].

Lattice constant	a (nm)	b (nm)	c (nm)
Orthorhombic [143]	0.549	0.575	0.793
Hexagonal [149]	0.36		0.585
Cubic [150]	1.04		

Table 5.1: Experimentally found lattice constants for orthorhombic, hexagonal and cubic $GdScO_3$.

Investigations on $SmScO_3$ revealed that $SmScO_3$, in contrast to $GdScO_3$, grows hexagonally on 5 nm or 30 nm thick Y_2O_3 layers on Si (111). The lattice constants for hexagonal $SmScO_3$ are in the margin of errors the same as for hexagonal $GdScO_3$. Hence, hexagonal $SmScO_3$ was tested as another alternative growth template for hexagonal $GdScO_3$. This approach was successful and the associated XRD θ-2θ scan in the out of plane direction can be seen in Fig. 5.17.

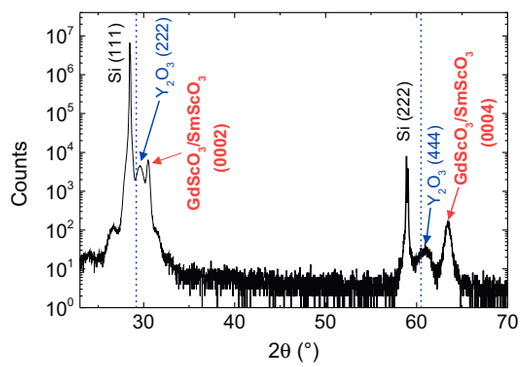

Figure 5.17: XRD θ-2θ scan of hexagonal $GdScO_3$ (0002) (40 nm) on $SmScO_3$ (5 nm) on Y_2O_3 (5 nm)/Si. The position of the $GdScO_3/SmScO_3$ reflection exactly corresponds to the $GdScO_3$ (0002) reflection found for $GdScO_3$ on GaN. The reflections assigned to Y_2O_3 are shifted towards higher angles compared to what is expected for bare Y_2O_3 from former measurements marked with vertical dashed blue lines.

The small, sharp reflection at 30.49° assigned to $GdScO_3/SmScO_3$ (0002) corresponds exactly to the reflection found for hexagonal $GdScO_3$ (0002) on GaN. However, the reflections of the underlying Y_2O_3 are shifted towards higher angles than expected from earlier measurements and from a lattice constant of 1.06 nm (compare blued dashed lines). Possibly the rather thin Y_2O_3 is strained by the thicker oxide layers above.

A ψ-scan in the $GdScO_3$ (1-101) direction (not shown here) exhibits sixfold symmetry and confirms the hexagonal structure of the oxide layer. Furthermore XRD analysis reveals that the crystallinity is improved compared to hexagonal $GdScO_3$ grown on thin Y_2O_3 on Si: a rocking curve around the $GdScO_3/SmScO_3$ (0002) reflection reveals a $FWHM$ of 0.06°. Therefore also a set of $GdScO_3$ layers grown on $SmScO_3$ was prepared for CV measurements, cf. Section 5.6.2.

As noted before the formation of a specific phase of $GdScO_3$ on a certain substrate was not always the expected one. DFT calculations will be presented in Section 6.2.1 evaluating the energy of formation of the different polymorphs of $GdScO_3$ in order to obtain more insight into the origins of the crystallization behavior.

5.4 Structural characterization of epitaxial $LaLuO_3$

Two different growth templates - GaN and Y_2O_3/Si - and different substrate temperatures are used to stabilize and explore either the hexagonal or the cubic phase of $LaLuO_3$. The procedure to characterize the lattices is analog to the one used for $GdScO_3$ and is therefore kept short.

Part of the results were already published by Schäfer et al. in [161].

5.4.1 $LaLuO_3$ on GaN

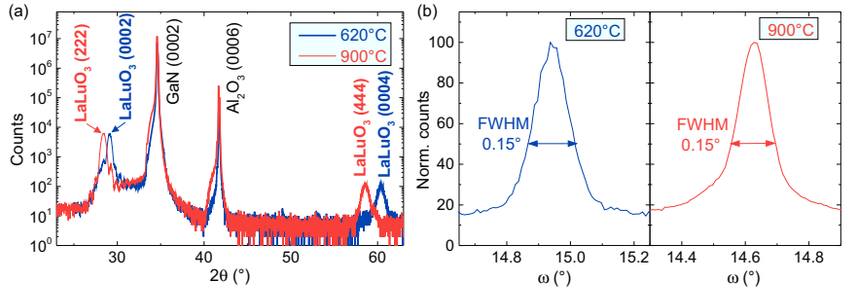

Figure 5.18: (a) XRD θ-2θ scan of hexagonal (blue) and cubic (red) $LaLuO_3$ with a thickness of 15 nm grown on GaN at 620°C and 900°C, respectively. The $LaLuO_3$ peak position in the θ-2θ scan shifts towards lower angles for higher growth temperatures. This corresponds to the phase transition from hexagonal to cubic $LaLuO_3$. (b) Rocking curves around the (0002) reflection of hexagonal $LaLuO_3$ (blue) and around the (222) reflection of cubic $LaLuO_3$ (red).

XRD θ-2θ scans in the out of plane direction of $LaLuO_3$ on GaN deposited at different temperatures are depicted in Fig. 5.18. The $LaLuO_3$ reflections are shifted towards lower angles for deposition temperatures of 900°C compared to 620°C. Hence, the out of plane lattice distances and the phase of $LaLuO_3$ depend on temperature. Further analysis shows that layers grown at 620°C form a hexagonal lattice with an out of plane lattice constant c of 0.612 nm and that films grown at 900°C form the cubic structure of $LaLuO_3$ along the (111) direction with a lattice constant a of 1.086 nm. The rocking curve measurements of the $LaLuO_3$ (0002) and $LaLuO_3$ (222) reflections in Fig. 5.18 (b) reveal a $FWHM$ of 0.15° for both hexagonal and cubic $LaLuO_3$ on GaN. These values are slightly higher than the ones determined for hexagonal $GdScO_3$ on GaN grown with a $FWHM$ between 0.1° and 0.11°.

From XRD θ-2θ scans in the (1-101) and (1-102) direction of hexagonal $LaLuO_3$ presented in Fig. 5.19 the in plane lattice constant of hexagonal $LaLuO_3$ is deduced to be 0.375 nm. A ψ scan along the (1-101) direction (not shown here) exhibits sixfold symmetry

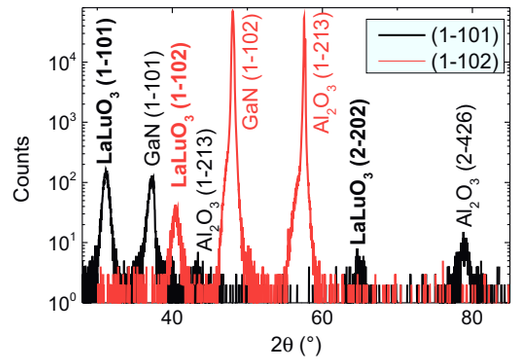

6

Figure 5.19: XRD θ-2θ scan along the (1-101) (black trace) and (1-102) (red trace) direction of hexagonal $LaLuO_3$ grown on GaN at 620°C.

and confirms the assumption of a hexagonal lattice.

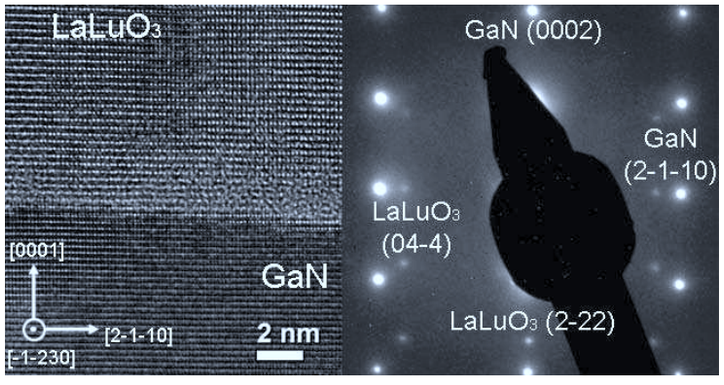

Figure 5.20: HRTEM direct image (left) and electron diffraction (right) of cubic $LaLuO_3$ grown on GaN at 900°C. Several reflections of $LaLuO_3$ and GaN are marked.

TEM measurements were performed to study cubic $LaLuO_3$ in more detail. The direct image in Fig. 5.20 gives evidence to the high crystallinity of the $LaLuO_3$ although close to the interface the $LaLuO_3$ is partly disordered probably due to strain. The bright and weak spots in the corresponding electron diffraction pattern on the right of Fig. 5.20 belong to GaN and $LaLuO_3$, respectively, and can be indexed applying the known unit cells of hexagonal GaN and cubic $LaLuO_3$.

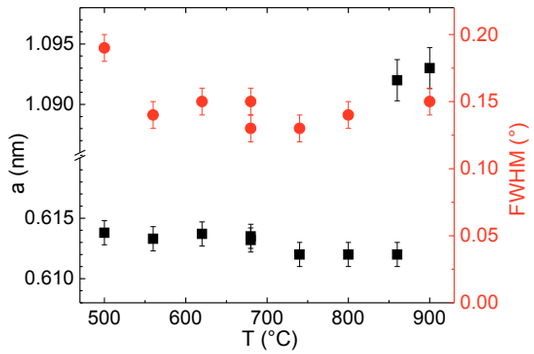

Figure 5.21: Temperature dependence of lattice constant (left axis, black squares) and $FWHM$ of the rocking curve (right axis, red circles) of $LaLuO_3$ grown on GaN. A phase transition is visible for 860°C from hexagonal to cubic $LaLuO_3$. Mind the broken axis for a.

An evaluation of the temperature dependence of the out of plane lattice constant of $LaLuO_3$ films grown on GaN, compare Fig. 5.21 (black squares, left axis), discloses that the phase transition from hexagonal to cubic $LaLuO_3$ occurs around 860°C, where both phases are present. Below 860°C the lattice parameter is almost constant belonging to the hexagonal form of $LaLuO_3$. The $FWHM$ of the rocking curves (red circles, right axis in Fig. 5.21) is typically around 0.15° for single-phase films, only the low temperature layer grown at 500°C exhibits a higher $FWHM$ of 0.19°.

5.4.2 $LaLuO_3$ on Y_2O_3/Si

Structural investigations of $LaLuO_3$ grown on Y_2O_3/Si (111) were carried out in the same manner as for layers grown on GaN, i.e. the lattice was analyzed by XRD and TEM for different deposition temperatures and different Y_2O_3 layer thicknesses.

In the case of $LaLuO_3$ grown on 30 nm thick Y_2O_3 on Si (111) at a deposition temperature of 550°C the $LaLuO_3$ crystallizes in the hexagonal phase. Fig. 5.22 (a) compares θ-2θ scans in the out of plane direction of samples with and without $LaLuO_3$ with a layer thickness of 100 nm and reveals that Y_2O_3 and $LaLuO_3$ have the same out of plane lattice distance. This out of plane lattice distance corresponds to the one found for hexagonal $LaLuO_3$ deposited on GaN. The hexagonal lattice type is confirmed by a ψ scan along the (1-101) direction of $LaLuO_3$ exhibiting sixfold symmetry, see Fig. 5.22 (b). The $FWHM$ of a rocking curve around $LaLuO_3$ (0002) also depicted in Fig. 5.22 (b) amounts to 0.06°. This high crystallinity matches the one of the underlying Y_2O_3.

The good crystallinity is disclosed by TEM. Some defects, which are visible for Y_2O_3 in the direct image in Fig. 5.23, continue in the $LaLuO_3$ layer. Apart from that the layers

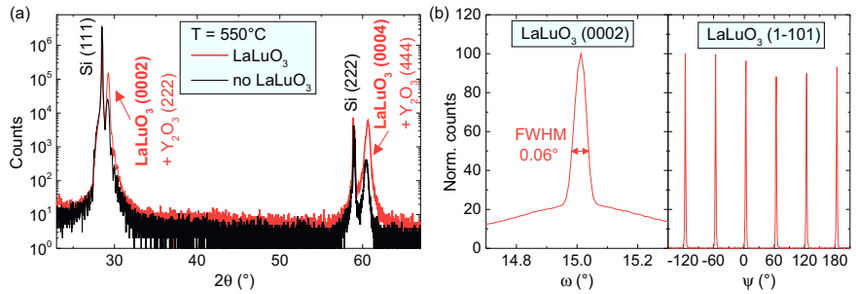

Figure 5.22: (a) XRD θ-2θ scan in the out of plane direction with (red) and without (black) hexagonal $LaLuO_3$ (with a thickness of about 100 nm) on 30 nm Y_2O_3 on Si (111) grown at 550°C adapted from [161]. (b) Rocking curve around $LaLuO_3$ (0002) reflection and ψ scan around $LaLuO_3$ (1-101) reflection with a thickness of $\sim$ 50 nm on 7 nm Y_2O_3 on Si (111) grown at 550°C.

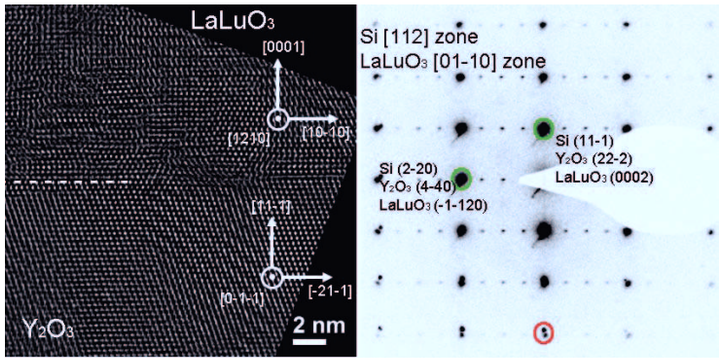

Figure 5.23: HRTEM direct image (left) and electron diffraction (right) of hexagonal $LaLuO_3$ grown on Y_2O_3/Si at 550°C, adapted from [161]. The reflections of Si, Y_2O_3 and $LaLuO_3$ overlap for smaller radii in the diffraction pattern. Examples are marked by green circles. For higher radii the spots separate, compare the example marked by the red circle: the Si reflection which has a higher lattice plane spacing is slightly closer to the center than the reflections of the two oxide layers.

are well ordered. Many different spots are visible in the electron diffraction pattern in Fig. 5.23 which belong to Si, to Y_2O_3, which is rotated by 30° around the out of plane axis compared to Si, and to hexagonal $LaLuO_3$. Two of the $LaLuO_3$ reflections are indexed in the figure.

The lattice constants extracted from TEM are consistent with the ones extracted from XRD.

XRD θ-2θ scans of $LaLuO_3$ deposited on Y_2O_3/Si are repeated for substrate temperatures between 450°C and 800°C. Between 450°C and 700°C the diffraction pattern retains its form, but the $LaLuO_3$ reflection shifts to higher angles which corresponds to a decrease in c from 0.613 nm to 0.608 nm (cf. Fig. 5.24 (b)). Probably, for lower energy, i.e. lower deposition temperature, the $LaLuO_3$ is constrained by the Y_2O_3 lattice in a stronger way than for higher energies.

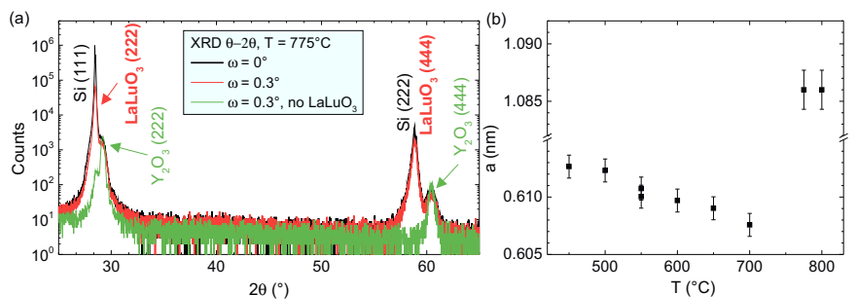

Figure 5.24: (a) XRD θ-2θ scan in the out of plane direction of cubic $LaLuO_3$ grown on Y_2O_3/Si at 775°C. The $LaLuO_3$(222) reflection overlaps with the Si(111) reflection (black curve). To uncover the pure $LaLuO_3$ signal, the scan is repeated after tilting the sample around ω by 0.3° (red curve). For comparison a θ-2θ scan for a tilted sample without $LaLuO_3$ is depicted (green curve). (b) Temperature dependence of the lattice constant of $LaLuO_3$ on Y_2O_3/Si. Mind the broken axis for a. A phase transition from hexagonal to cubic $LaLuO_3$ occurs between 700°C and 775°C.

The analysis of a θ-2θ scan in the out of plane direction of 100 nm $LaLuO_3$ deposited on Y_2O_3/Si at 775°C in black in Fig. 5.24 (a) is more difficult to interpret than the ones before. Only the Si reflections are visible, the ones of Y_2O_3 vanished and also $LaLuO_3$ reflections are not visible. The Y_2O_3 reflection vanished because at these high temperatures it reacts with Si to an amorphous silicate [136]. In order to determine whether there is an $LaLuO_3$ reflection underneath the Si reflection, the method described in Section 3.2.1 is applied: the XRD θ-2θ scan was repeated after tilting the sample by 0.3° around ω to cancel out the reflection from the Si substrate. The result is presented in red in Fig. 5.24 (a). To confirm that the visible reflection belongs to $LaLuO_3$, the same tilted scan was performed for the sole Y_2O_3/Si growth template, see the green trace in Fig. 5.24 (a). The comparison

proves that $LaLuO_3$ has the same out of plane lattice spacing as Si. This result fits to cubic $LaLuO_3$ which shows exactly the doubled lattice constant of Si: $a_{LLO} = 1.086\,\text{nm}$ and $a_{Si} = 0.543\,\text{nm}$ [16, 132].

Hence, for high deposition temperatures the $LaLuO_3$ forms the cubic phase rather than the hexagonal one. The same behavior was already observed for $LaLuO_3$ on GaN. The temperature dependence of the lattice structure is summarized in Fig. 5.24 (b) revealing a phase transition between 700°C and 775°C.

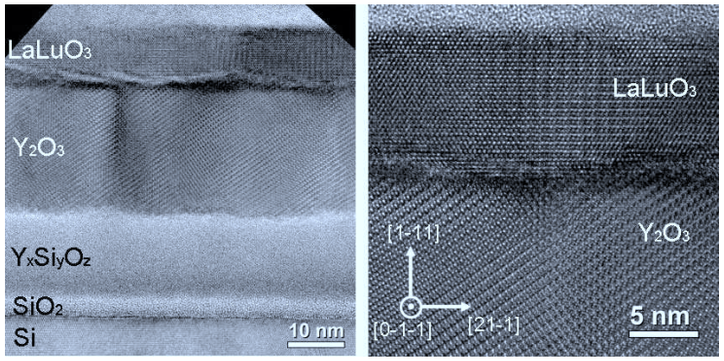

Figure 5.25: TEM and HRTEM direct images of cubic $LaLuO_3$ grown on Y_2O_3/Si at 775°C. $LaLuO_3$ grows epitaxially on the surface of Y_2O_3 while an amorphous silicate is forming at the interface between Si and Y_2O_3 due to the high deposition temperature. The right image shows an enlargement of the interface $LaLuO_3$ to Y_2O_3.

TEM images in Fig. 5.25 give more insight into the processes during deposition of cubic $LaLuO_3$ on Y_2O_3/Si at high temperatures. Directly at the Si interface a SiO_2 layer of roughly 3 nm forms. On top of this layer the amorphous silicate is visible. But not all of the Y_2O_3 reacts with the Si. Part of it is still crystalline on top of the silicate. The $LaLuO_3$ layer exhibits several defects and contrast differences close to the interface to Y_2O_3 which are probably caused by strain due to a lattice mismatch. After approximately 5 nm the $LaLuO_3$ lattice is stabilized and shows high crystallinity.

XRD and TEM consistently reveal a lattice constant of 10.86 nm for cubic $LaLuO_3$ which fits the value given for cubic $LaLuO_3$ by Liu et al. [132].

In addition to the temperature dependence of the $LaLuO_3$ phase also the dependence on the Y_2O_3 layer thickness was explored. In contrast to $GdScO_3$ grown on Y_2O_3, the $LaLuO_3$ phase does not depend on the Y_2O_3 thickness.

Since La_2O_3 is known to be hygroscopic and thus air exposure enlarges the roughness and degrades the permittivity of La_2O_3 films [162], the degradation of $LaLuO_3$ in air was examined. As an example in Fig. 5.26 XRD $\theta-2\theta$ scans are presented of 100 nm hexagonal $LaLuO_3$ deposited on 30 nm Y_2O_3 on Si (111).The first scan (black) was recorded the same day as the deposition, the second one (red) was carried out more than a year later. The

Lattice constant	a (nm)	b (nm)	c (nm)
Orthorhombic [10]	0.583	0.602	0.838
Hexagonal [161]	0.375		0.612
Cubic [132, 152]	1.086		

Table 5.2: Experimentally found lattice constants of orthorhombic, hexagonal and cubic $LaLuO_3$.

comparison of the two shows that there is no change over time in the XRD characteristics. Hence, hexagonal $LaLuO_3$ does not degrade in air and is not hygroscopic and fulfills an essential requirement for device processing.

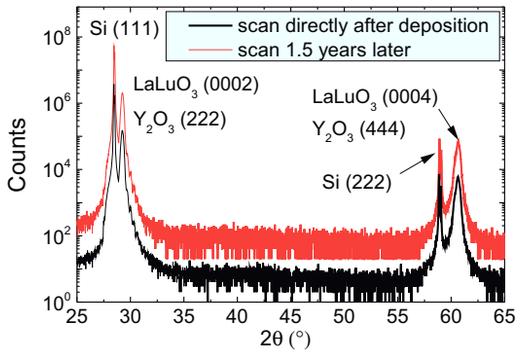

Figure 5.26: XRD θ-2θ scans of hexagonal $LaLuO_3$ on Y_2O_3/Si measured the same day as the deposition took place (black) and measured one and a half years later (red), adapted from [161].

In summary, for both presented growth templates - GaN and Y_2O_3 - it is possible to stabilize both the hexagonal (along [0001]) and the cubic phase (along [111]) of $LaLuO_3$. Hereby, the substrate temperature range during growth for hexagonal $LaLuO_3$ is quite broad (up to 300°C) while cubic $LaLuO_3$ only forms at high temperatures close to the limit of the PLD system. In all cases the crystallinity of $LaLuO_3$ is typically in the same range as the one of the growth template. The lattice constants of the three known crystalline polymorphs of $LaLuO_3$ are collected in Tab. 5.2.

5.5 Discussion: Structure of $GdScO_3$ and $LaLuO_3$

In Section 5.5.1 models for possible space groups of the hexagonal and cubic oxides are presented in order to have a basis for the discussion of the stacking of the lattices.

The studies presented above demonstrated that small variations in the deposition conditions can change the phase of the oxide. Factors such as lattice mismatch and differences in the energies of formation have influence on the phase stabilization. To understand better why a certain polymorphous phase prevails, the lattice mismatch will be evaluated for the different material combinations in Section 5.5.2. Later the energy of formation will be taken into account. In the case of $LaLuO_3$ these energies were calculated by Watahiki et al. [152]. For $GdScO_3$ the energies of formation calculated by density functional theory are discussed in Chapter 6.

5.5.1 Space group models

The cubic form of $LaLuO_3$ was also investigated by other groups which deposited cubic $LaLuO_3$ on GaAs (111) [132] and Si (111) [152, 158, 159]. The lattice constant of 1.086 nm fits well to what was found in this work. Niehle and Trampert suggested that $LaLuO_3$ forms a bixbyite crystal structure associated with space group number 206 (*Ia-3*) [159]. This can probably be extended to cubic $GdScO_3$: the diffraction spots of smaller intensity in Fig. 5.16 are typical for bixbyite lattices. Furthermore the binary compounds Gd_2O_3 and Sc_2O_3 both crystallize in space group *Ia-3* [39, 163] and even many other rare earth binary and ternary rare earth oxides can be added to this group such as Y_2O_3, $EuYbO_3$ or $GdYO_3$ [164–166]. Hence, in the following discussion it is assumed that both cubic $GdScO_3$ and cubic $LaLuO_3$ crystallize in the space group *Ia-3*. Sketches of the crystals such as the one in Fig. 5.27 (a) are constructed adapting the crystal lattice of $EuYbO_3$ [165] in combination with the experimentally found lattice constants for cubic $LaLuO_3$ and cubic $GdScO_3$.

In the case of hexagonal $LaLuO_3$ or $GdScO_3$ no detailed analysis of the atomic order in the crystal is known to my knowledge. Nevertheless, there is a high temperature hexagonal phase of La_2O_3: for temperatures above $\approx$2000°C La_2O_3 transforms into space group number 194 ($P6_3/mmc$) [167] which is one of the hexagonal space groups. The possible atom positions all have a probability of occupancy of one half. In the following discussion we assume that also hexagonal $LaLuO_3$ and $GdScO_3$ crystallize in space group number 194 and that the La positions with occupancy of 0.5 in hexagonal La_2O_3 are occupied by La and Lu or Gd and Sc, respectively, with individual occupancies of 0.25.

For the case of $LaLuO_3$ the resulting hexagonal and cubic unit cells are presented in Fig. 5.27. The unit cells are depicted as three dimensional unit cells and in topview with respect to the sample surface present here, i.e. the (0001) plane for hexagonal $LaLuO_3$ and the (111) plane for cubic $LaLuO_3$.

5.5.2 Lattice mismatch

The lattice mismatch is calculated for the different growth templates for either the hexagonal or the cubic form of the epitaxial oxides in Tab. 5.3 and is then compared to stacked systems experimentally stabilized.

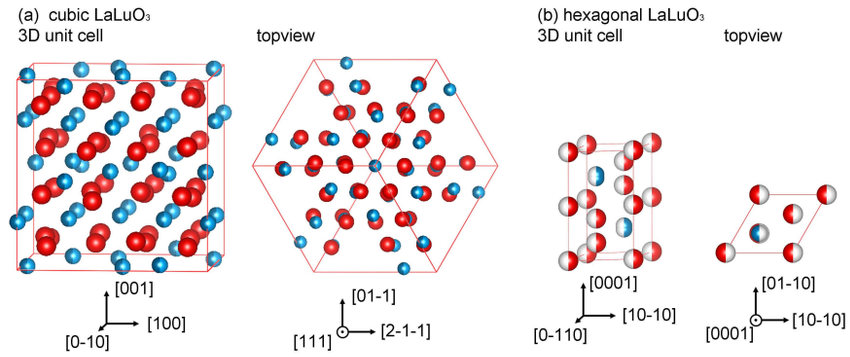

Figure 5.27: Schematics of unit cells of cubic (a) and hexagonal (b) $LaLuO_3$ depicted in three dimensional view and as topview with respect to the growth planes in the presented experiments. The cubic unit cell contains in total 80 atoms, the hexagonal one 5 atoms. Red spheres represent O and blue spheres represent either La and Lu. The metal atoms are distributed randomly on the respective positions. Half filled spheres depict atomic sites with a probability of occupancy of 0.5. Sketches were made using *VESTA* [86].

When the lattice system of the the epitaxial layers and the substrate are identical, e.g. cubic $GdScO_3$ on cubic Y_2O_3 or hexagonal $LaLuO_3$ on hexagonal GaN, with identical orientation the lattice mismatch can be calculated right away with Equation 2.2.

When the lattice system of the epitaxial layer differs from the one of the growth template, the calculation of the lattice mismatch becomes more complex. Therefore as an example the lattice mismatch of hexagonal $LaLuO_3$ deposited on cubic Y_2O_3 will be discussed here in detail.

First the orientation of the layer with respect to the growth template has to be determined. This can be done either by TEM analysis or by XRD Ψ scans. Fig. 5.28 demonstrates three ψ scans on one layer system along the Si (202) (black), Y_2O_3 (404) (red) and $LaLuO_3$ (10-11) (green) reflections. Si and Y_2O_3 both show a threefold symmetry which assures the cubic structures. There is a 60° offset between the peak positions of Si and Y_2O_3. A stacking fault at the Si/Y_2O_3 interlayer leads to a rotation of 180° of the upper epitaxial layer around Si (111) and is the origin of this 60° offset [39]. As was discussed before $LaLuO_3$ shows a sixfold symmetry typical for hexagonal crystals. Hence, the in-plane alignment of the structure is described by the relationship: $LaLuO_3$ [10-10] ∥ Y_2O_3 [2-1-1] ∥ Si [-211].

Apart from establishing a basis for the lattice mismatch calculations, this discussion also enables to predict how the first $LaLuO_3$ layer could be positioned with respect to Y_2O_3. Fig. 5.29 is assembled assuming that a first layer of La and Lu atoms aligns with a top

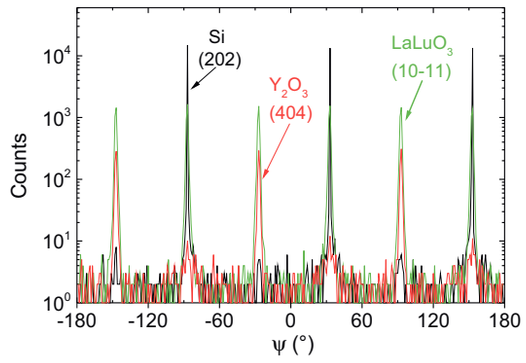

Figure 5.28: ψ scans along the Si (202) (black), Y_2O_3 (404) (red) and $LaLuO_3$ (10-11) (green) reflections of hexagonal $LaLuO_3$ deposited on Y_2O_3/Si (111).

layer of O atoms of the Y_2O_3 including the orientation results just described. No detailed interface examination has been done yet, so this picture is just a proposal on the growth mode and still has to be confirmed by experiments, i.e. HRTEM.

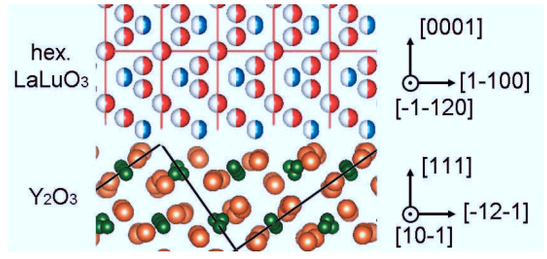

Figure 5.29: Side view schematics of the lattice structure of hexagonal $LaLuO_3$ deposited on Y_2O_3. Red, blue, orange and green spheres represent O, La/Lu, O and Y atoms, respectively. Sketches were made using *VESTA* [86].

To continue the determination of the lattice mismatch the projections along the surface normal of Y_2O_3 and hexagonal $LaLuO_3$ are sketched in Fig. 5.30 (a) and (b), respectively. Y_2O_3 is oriented in the (111) orientation in this configuration and shows a threefold symmetry. $LaLuO_3$ is oriented along (0001).

An overlay of both projections is depicted in Fig. 5.30 (c). Even though the borders of the unit cells sketched by black and red lines do not coincide, the atom positions do coincide and hence the lattice mismatch has to be small or even negligible. The distances

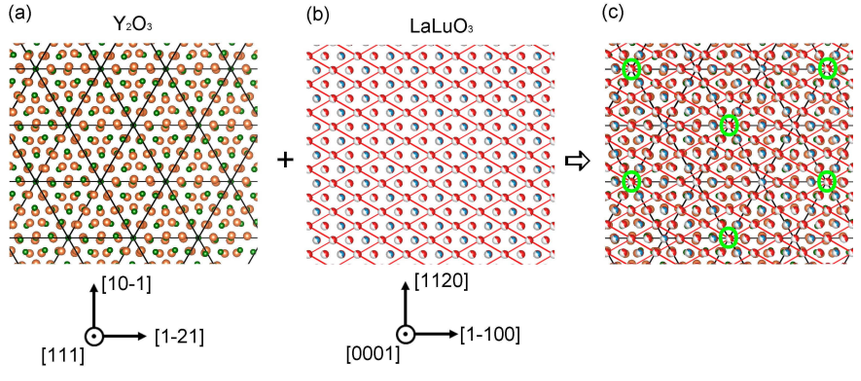

Figure 5.30: Schematics of topview lattice structure of hexagonal $LaLuO_3$ deposited on cubic Y_2O_3. (a) Topview of cubic Y_2O_3 after [168]: Y in green and O in orange. The black lines depict the edges of the cubic unit cell and the side length of the triangles is $d = \sqrt{2/3}\, a_{Y_2O_3} = 0.865\,\text{nm}$. (b) Topview of hexagonal $LaLuO_3$ assuming the same lattice as for La_2O_3 [169] combined with the $LaLuO_3$ lattice constants: La/Lu in blue, O in red. Half filled spheres mean that the probability of occupancy of this atom position is 0.5. The red lines depict the edges of the hexagonal unit cell. The side length of each rhomb is the in plane lattice constant of $LaLuO_3$ $a = 0.612\,\text{nm}$. (c) Overlay of both structures. The green circles indicate the crossing points of the two lattices and are the lattice points used to determine the lattice mismatch. Sketches were made using *VESTA* [86].

between the overlapping lattice points of the two lattices marked by the green circles in Fig. 5.30 (c) are compared to calculate the lattice mismatch between hexagonal $LaLuO_3$ and Y_2O_3. For this configuration the lattice mismatch equals 0.02 %. This is below the margin of error ($\approx$ 0.1 %) for the determination of the in plane lattice constant of $LaLuO_3$ by XRD and thus it is concluded that the lattice mismatch is smaller than the detection limit of the presented measurements, i.e. smaller than 0.1 %.

One can also use the patterns of the reciprocal lattices in the [111] or [0001] zone axis to decide if the lattices fit above each other and to find the respective lattice planes to determine the mismatch. For the example of hexagonal $LaLuO_3$ deposited on Y_2O_3, the electron diffraction patterns are calculated and overlaid, see Fig. 5.31.

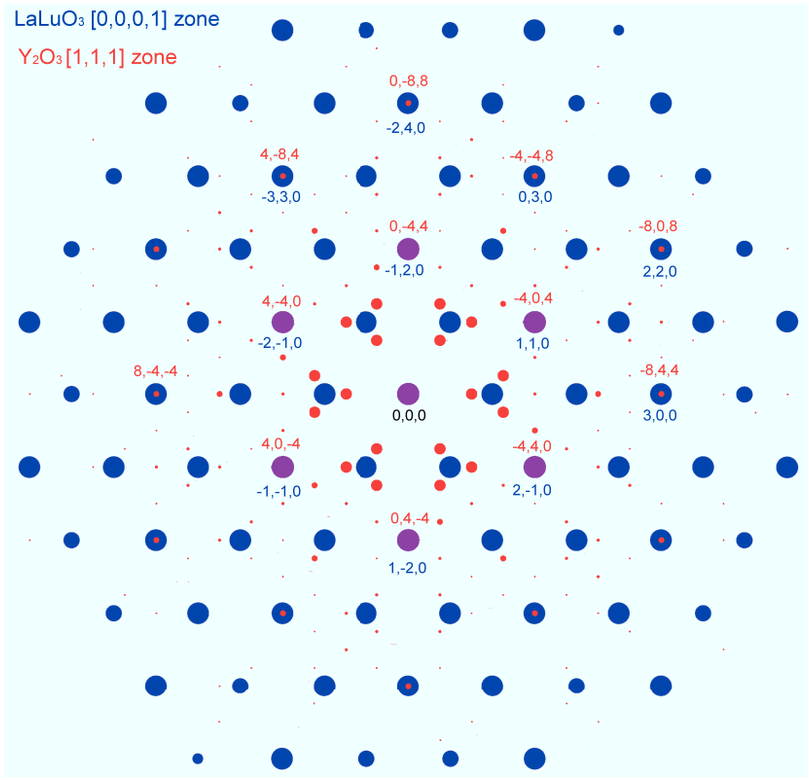

Figure 5.31: Calculated electron diffraction pattern of hexagonal $LaLuO_3$ in the [0001] zone axis (blue) on Y_2O_3 in the [111] zone axis (red). When diffraction spots of both oxides with equal intensity overlap they are colored in purple. Diffraction patterns calculated using [170].

One can clearly see that certain diffraction spots overlap and their Miller indexes can be

Oxide	(hkl)	Substrate	(hkl)	ϵ (%)	Exp. stabilized
$hLaLuO_3$	(11-20)	Y_2O_3	(-404)	-0.02	yes
$cLaLuO_3$	(440)	Y_2O_3	(440)	-2.4	yes, for high T
$hLaLuO_3$	(10-10)	GaN	(10-10)	-17.9	yes
	(60-60)		(50-50)	1.7	
$cLaLuO_3$	(-633)	GaN	(20-20)	-7.3	yes, for high T
	((-10)55)		(30-30)	3.4	
$hGdScO_3$	(11-20)	Y_2O_3	(-404)	4.0	no
$cGdScO_3$	(-404)	Y_2O_3	(-404)	1.9	yes
$hGdScO_3$	(11-20)	Si	(-202)	6.2	yes, low crystallinity
$cGdScO_3$	(-404)	Si	(-202)	4.2	no
$hGdScO_3$	(10-10)	GaN	(10-10)	13.2	yes
	(80-80)		(70-70)	0.9	
$cGdScO_3$	(-633)	GaN	(20-20)	-2.8	no

Table 5.3: Lattice mismatch ϵ of cubic (c-) and hexagonal (h-) $LaLuO_3$ and $GdScO_3$ for the different growth templates discussed in this work. The pairs of lattice plane spacings were found comparing the calculated electron diffraction patterns in the zone axis perpendicular to the surface. The last column annotates whether the stack could be realized experimentally. T describes the substrate temperature during PLD deposition.

used to determine the respective lattice plane spacings and the lattice mismatch.

Using the same approach the lattice mismatch was determined for cubic and hexagonal $LaLuO_3$ and $GdScO_3$ on the different growth templates, compare Tab. 5.3.

Some cases are not as clear as the one presented in Fig. 5.31. For example, the cubic $LaLuO_3$ lattice does not fit well on the GaN lattice, compare Fig. 5.32. The $LaLuO_3$ (-633) and GaN (20-20) or the $LaLuO_3$ ((-10)55) and GaN (30-30) almost overlap. The lattice mismatch for these lattice planes is 7.3 % and 3.4%, respectively.

A comparison between the lattice mismatch of cubic and hexagonal $LaLuO_3$ with respect to Y_2O_3 - 2 % and below 0.1 %, respectively - gives an explanation why the hexagonal form stabilizes for lower energies, i.e. lower growth temperatures.

Similarly, in the case of $GdScO_3$ deposited on Y_2O_3 (with thicknesses of 5 nm or more) the lattice mismatch for the cubic form (2 %) is smaller than for the hexagonal form (4 %) and the cubic form is the one observed experimentally. For very thin Y_2O_3 layers of 1 nm on Si (111) the hexagonal form of $GdScO_3$ could be stabilized experimentally. For such thin Y_2O_3 films it can be assumed that the Y_2O_3 is not yet relaxed and the lattice constant is determined by the underlying Si. In Tab. 5.3 also the lattice mismatch to Si was determined. For both cubic and hexagonal $GdScO_3$ the mismatch increases compared

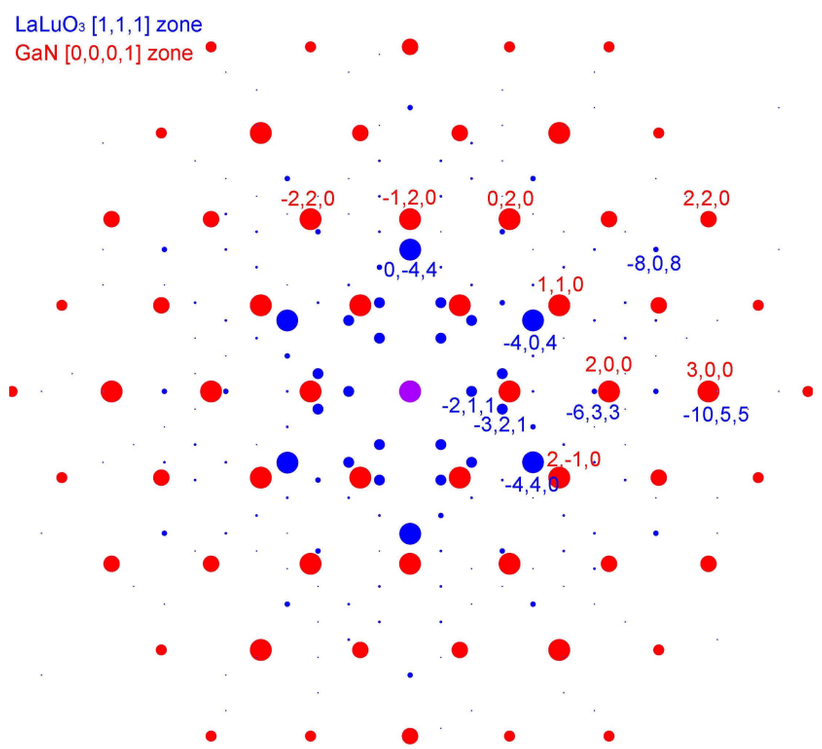

Figure 5.32: Calculated electron diffraction pattern of cubic $LaLuO_3$ in the [111] zone axis (blue) on GaN in the [0001] zone axis (red). Diffraction patterns calculated using [170].

to thick Y_2O_3 but the tendency remains the same and thus there is no advantage for the hexagonal $GdScO_3$ to form regarding mismatch. The decreased crystallinity of the hexagonal films on thin Y_2O_3 correlates with the less matched lattices.

In the case of hexagonal ternary oxides deposited on GaN the classical lattice mismatch is quite high: 18 % for $LaLuO_3$ and 13 % for $GdScO_3$. It is surprising that this form is favored on GaN compared to the cubic form which has a lattice mismatch to GaN between 2 % and 7 %. Regarding higher order lattice planes such as (60-60) of hexagonal $LaLuO_3$ and (50-50) of GaN, the mismatch of 2 % is rather small. Likewise, in the case of hexagonal $GdScO_3$ on GaN a value of 1 % is revealed. Hence, possibly five $LaLuO_3$ unit cells align along six GaN unit cells and the lattices match better than expected from the classical mismatch calculation.

Apart from considering the lattice match, also the energies of formation for the different polymorphs are crucial for the formation of a certain phase. In the case of $LaLuO_3$ Watahiki et al. determined these energies by ab-initio calculations [152]. It was demonstrated that for bulk crystals the energy of formation of hexagonal $LaLuO_3$ is roughly 100 meV lower than the cubic one and thus the hexagonal form is energetically favored. This fits the here observed tendency for both growth templates that cubic $LaLuO_3$ forms at higher substrate temperature, i.e. higher energy, than hexagonal $LaLuO_3$.

In Chapter 6 the respective calculated energies are presented for $GdScO_3$ crystals and afterwards the results are discussed in comparison to the experimental results.

The lattice mismatch is related to the critical thickness of an epitaxial layer, compare Eq. 2.3. In the case of hexagonal $GdScO_3$ deposited on GaN with a lattice mismatch of 13 % the critical thickness t_c equals 1.5 nm. Hence, one can conclude that the hexagonal $GdScO_3$ layers investigated here are all fully relaxed because their thicknesses exceed 5 nm. This coincides with the fact that no systematic tendency of the lattice constant change with layer thickness was observed on GaN.

5.6 Electrical characterization of $GdScO_3$ and $LaLuO_3$

After identifying the different polymorphs of $GdScO_3$ and $LaLuO_3$ that can be stabilized on GaN and Y_2O_3, it is important to evaluate the electrical properties of the polymorphous oxides for future applications. While the amorphous and orthorhombic phases of $GdScO_3$ and $LaLuO_3$ are already explored, little data exist on the cubic and hexagonal form. The following section focuses on the permittivity and the band gap of these new phases to judge their general suitability as a gate dielectric.

5.6.1 Permittivity approximations for $GdScO_3$ and $LaLuO_3$

As discussed in Section 2.4.1, it is possible to roughly estimate the relative permittivity using the Clausius-Mossotti equation. This is done for hexagonal and cubic $GdScO_3$ and $LaLuO_3$ in Tab. 5.4. Higher κ values are expected for $LaLuO_3$ than for $GdScO_3$ and for the hexagonal form compared to the cubic form. Since the predicted value for cubic $LaLuO_3$ is only half as large as the experimentally found one of 30 [132], one can see that

	Phase	a_m (Å^3)	V_m (Å^3)	κ
$GdScO_3$	hexagonal	13.21	65.66	17.1
	cubic		70.30	12.1
$LaLuO_3$	hexagonal	15.74	74.53	24.0
	cubic		80.05	15.4

Table 5.4: Polarizability α_m, molar volume V_m and estimated relative permittivities κ for cubic and hexagonal $GdScO_3$ and $LaLuO_3$ calculated using the Clausius Mossotti equation 2.8. Ion polarizabilities were taken from Shannon [27]. For hexagonal $LaLuO_3$ an adjusted ion polarizability for O^{2-} was used because of the high volume contribution of oxygen in this crystal, compare [27].

the Clausius-Mossotti equation should rather be used for qualitative than quantitative evaluations.

5.6.2 Permittivity of $GdScO_3$

Capacitance voltage measurements are carried out in order to determine the permittivity of hexagonal and cubic $GdScO_3$. This is done for $GdScO_3$ films with different layer thicknesses deposited on either 1 nm or 5 nm thin Y_2O_3, compare Fig. 5.33.

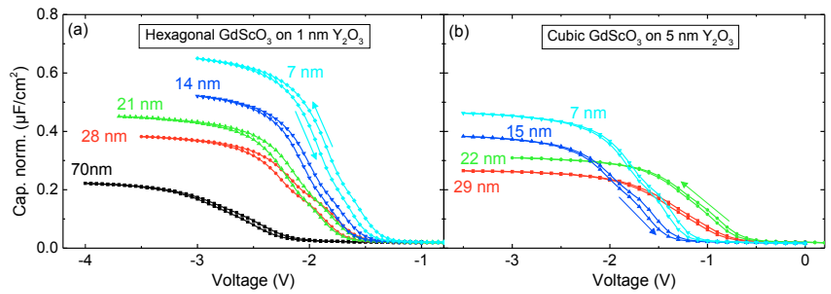

Figure 5.33: CV measurements of (a) hexagonal $GdScO_3$ deposited on 1 nm Y_2O_3 on Si(111) and (b) cubic $GdScO_3$ deposited on 5 nm Y_2O_3 on Si(111). Arrows indicate the sweep direction.

For both cases the CV curves are shifted towards negative voltages and show hysteresis effects which are slightly higher for the hexagonal $GdScO_3$. The density of interfacial traps is around 1×10^{12}eV^{-1}cm^{-2} or below. Since $GdScO_3$ was not deposited directly on Si, the D_{it} is dominated by the Y_2O_3 to Si interface here. In the case of hexagonal $GdScO_3$ the CV curves shift further towards negative voltage for increasing thickness which is an

indication for an increasing number of positive charges. The stretch out for thick layers is a sign for an increased number of traps in the oxide. In the case of cubic $GdScO_3$ the CV curves are also shifted, but there is no visible tendency with oxide layer thickness.

The ***CET*** extracted from the maximum capacitances were plotted as a function of oxide thickness in ***CET*** plots presented in Fig. 5.34. The ***CET*** of the interfacial layers are quite similar with values of 4.4 nm and 5 nm even though the underlying Y_2O_3 thickness is quite different: 1 nm for hexagonal $GdScO_3$ and 5 nm for cubic $GdScO_3$. This effect can be explained by an interfacial SiO_2 layer that forms during PLD deposition which was observed by TEM (cf. Fig. 5.12). For the thinner Y_2O_3 the SiO_2 has a thickness of 4 nm, for the thicker Y_2O_3 it is about 3 nm thick. The Y_2O_3 and SiO_2 layers both contribute to the ***CET*** of the interfacial layer.

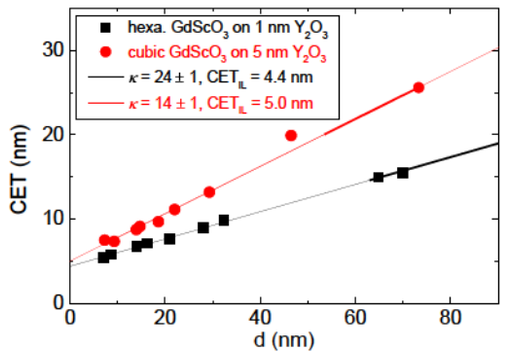

Figure 5.34: CET plots for hexagonal (black) and cubic (red) $GdScO_3$ deposited on 1 nm and 5 nm Y_2O_3 on Si (111), respectively, adapted from [149, 161]. The intercept and the slope of the corresponding linear fits reveal the ***CET*** of the interfacial layer and the permittivity of $GdScO_3$, respectively.

The relative permittivities are deduced from the inverses of the slope of the fitted lines in Fig. 5.34: κ equals to 24 and 14 for hexagonal and cubic $GdScO_3$, respectively.

As described in Section 5.3, it is also possible to stabilize hexagonal $GdScO_3$ on other growth templates based on $SmScO_3$ and GaN. In Fig. 5.35 (a) CV curves are presented for $GdScO_3$ grown on a template composed of 5 nm $SmScO_3$ and 5 nm Y_2O_3 on Si (111). Hysteresis effects are reduced compared to the pure Y_2O_3/Si template which probably correlates to the increased crystallinity of the oxide films. Again there is a shift towards negative voltages which is higher for thinner $GdScO_3$ in this case and might be dominated by $SmScO_3$. The D_{it} which is mainly affected by the Y_2O_3 varies between 4 and $12 \times 10^{11}\,eV^{-1}cm^{-2}$.

Also in the case of hexagonal $GdScO_3$ deposited on GaN CV measurements were carried

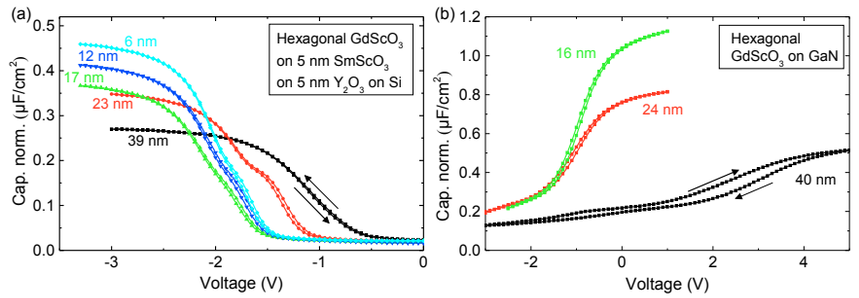

Figure 5.35: Capacitance voltage measurements of hexagonal $GdScO_3$ layers with different thicknesses deposited on (a) 5 nm $SmScO_3$/5 nm Y_2O_3/p-Si and on (b) n-doped GaN. Arrows indicate the sweep direction.

out, see Fig. 5.35 (b). Below some contact pads leakage currents hindered reasonable measurements probably due to pinholes in the GaN. For $GdScO_3$ layer thicknesses of 16 nm and 24 nm the CV curves are steep and show very small hysteresis so there are few traps in the oxide. Also the interfacial trap density is low $D_{it} = 6 \times 10^{11}\,\mathrm{eV}^{-1}\mathrm{cm}^{-2}$. For the thick layer of 40 nm thickness the D_{it} is increased to $1 \times 10^{12}\,\mathrm{eV}^{-1}\mathrm{cm}^{-2}$ and also the stretch out of the CV and the increased hysteresis point out that the number of oxide traps is increased. Thus thicker layers suffer from increased trap densities.

CET plots are derived for all three sets of CV data of hexagonal $GdScO_3$, see Fig. 5.36. The corresponding linear fits show varying CET of the interfacial layers which is due to the different oxide layer thicknesses before $GdScO_3$ growth but also because a SiO_2 layer forms during PLD growth for the Si based samples while in the case of GaN no native oxide forms.

The relative permittivities extracted from the CET plot are 25, 24 and 27 and fit to each other within the margin of error. In the case of hexagonal $GdScO_3$ grown on thin Y_2O_3 one has to keep in mind, that part of the $GdScO_3$ layer was amorphized and affects the determination of κ. Probably the value of 24 is a mean permittivity value of amorphous $GdScO_3$ (23 [137]) and hexagonal $GdScO_3$ (which should have a relative permittivity $\kappa \approx 26$ regarding the measurements on the other growth templates). Hence, even though the crystallinity of the hexagonal $GdScO_3$ differs from substrate to substrate (cf. Section 5.3), the extracted permittivity values in the out of plane direction agree well with each other.

5.6.3 Permittivity of $LaLuO_3$

Also hexagonal and cubic $LaLuO_3$ were investigated with respect to their relative permittivities. Unfortunately, no reasonable CV measurements could be carried out for $LaLuO_3$ on GaN. This might be due to a decreased quality of the GaN or due to small band offsets of $LaLuO_3$ to GaN.

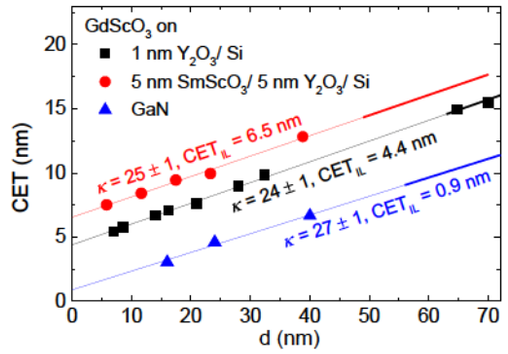

Figure 5.36: CET of hexagonal $GdScO_3$ deposited on 1 nm Y_2O_3 on Si (111) (black squares), on 5 nm $SmScO_3$ on 5 nm Y_2O_3 on Si (111) (red circles) and on GaN (blue triangles).

In the case of high temperature growth of cubic $LaLuO_3$ during PLD the pulse frequency was changed instead of varying the deposition time to keep the thermal budget constant for all layers. Thus the silicate formation should be more or less identical for all layers and the silicate should give a constant contribution to the total capacitance.

The CV measurements for cubic and hexagonal $LaLuO_3$ on the Si based growth template exhibit a typical dependence on thickness. The permittivity was extracted from CET plots, compare Fig. 5.37. The layers grown on Y_2O_3/Si at 550°C disclose a CET of the interfacial layer of 5 nm. Here the Y_2O_3 and a SiO_2 interfacial layer contribute to the CET_{IL} value. For 30 nm Y_2O_3 deposited at 750°C the CET of the interfacial layer of 16 nm is composed of three contributions: a SiO_2 interlayer, the yttrium silicate formed during PLD growth and the remaining crystalline Y_2O_3. The slopes of the linear fits reveal similar relative permittivities: 26 for hexagonal and 23 for cubic $LaLuO_3$, although the permittivity of cubic $LaLuO_3$ is questionable due to the silicate formation (see above). The permittivity of cubic $LaLuO_3$ is lower than the value of 30 deduced by Liu et al. for cubic $LaLuO_3$ on GaAs [132].

The CV studies on $GdScO_3$ and $LaLuO_3$ show that hexagonal $GdScO_3$ and cubic and hexagonal $LaLuO_3$ have high permittivities even though they do not outperform the orthorhombic phases. The investigations on hexagonal $GdScO_3$ deposited on GaN show that for layer thicknesses up to 20 nm the MOS stack shows small traps densities (e.g. $D_{it} = 6 \times 10^{11}\,\mathrm{eV^{-1}cm^{-2}}$, few mobile or oxide charges) which is important for application as gate dielectric.

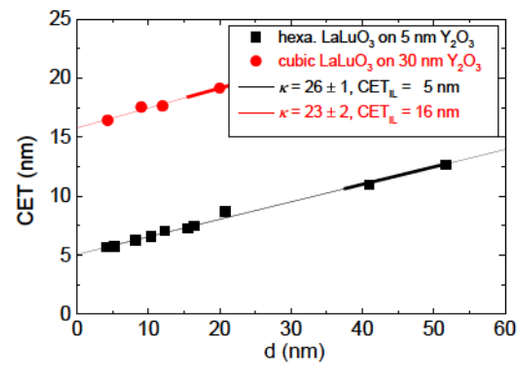

Figure 5.37: CET plots for hexagonal (black) and cubic (red) $LaLuO_3$ deposited on 5 nm and 30 nm Y_2O_3 on Si (111) at 550°C and 750°C, respectively. The intercept and the slope of the corresponding linear fits reveal the *CET* of the interfacial layer and the permittivity of $GdScO_3$.

5.6.4 Band gap determination

As was discussed before, in order to be suitable for the use as passivation or gate dielectric, the oxides need to exhibit good insulating properties. Therefore, Schlom et al. designated amongst other requirements that a gate oxide should have a band gap above 5 eV [6]. This is just a pre-condition. Also the band offsets of the conduction band and the valence band of the oxide with respect to the semiconductor should be greater than 1 eV [23]. The band gap can be determined rather quickly compared to the band offsets and for many large band gap insulators also the band offsets are sufficient.

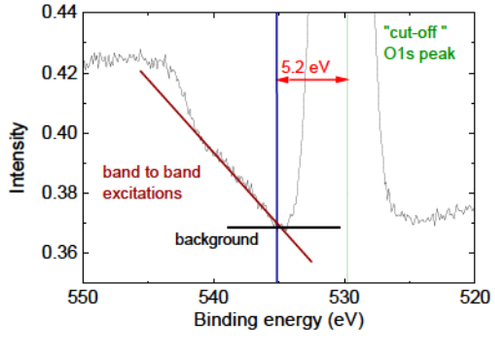

Figure 5.38: XPS O 1s spectra of hexagonal $GdScO_3$ deposited on GaN. The colored lines indicate how the band gap is determined using the method of Miyazaki.

The different polymorphs of $GdScO_3$ and $LaLuO_3$ are analyzed using XPS spectra by the method of Miyazaki (see Section 3.2.1). The XPS spectrum was analyzed in the region of the O 1s peak. An example of the O 1s spectra for hexagonal $GdScO_3$ deposited on GaN is depicted in Fig. 5.38. Due to huge intensity differences only the base of the O 1s peak is presented and its maximum is marked by the vertical green line. The energy region of the band-to-band excitations is marked by the brown line, the background by the horizontal black line. The band gap energy is then defined by the difference between the O 1s peak and the onset of band to band excitations (vertical blue line).

The case presented here reveals a band gap of (5.2 ± 0.2) eV for hexagonal $GdScO_3$. This analysis was repeated for all polymorphs of $GdScO_3$ and $LaLuO_3$ and the resulting band gaps are summarized in Tab. 5.5. In addition, a comparison to experimentally found band gaps in literature is added and details are given on which growth template the respective phase was stabilized.

There are some variations between the different measurement techniques and between the different polymorphs, but in general all band gap values are in the range between 5.2 eV and 6.0 eV for both $GdScO_3$ and $LaLuO_3$. In average the $LaLuO_3$ band gap is slightly higher. Even though the band gaps are smaller then the ones of HfO_2 and Al_2O_3, they are still sufficient for typical MOS devices, compare Schlom et al. [6].

For comparison the band gap of $LaLuO_3$ was additionally determined by ellipsometry as it was done for $Hf_{0.8}Lu_{0.2}O_2$ in Section 4.5.1. A band gap value of 5.4 eV was determined which is right in the middle between the value that was deduced by XPS (5.6 eV - 5.8 eV) and the one determined by internal photoemission (5.2 eV [153]). The different extracted band gap values are a good example of the uncertainties of the different methods.

5.6.5 Leakage current investigation of $GdScO_3$ on GaN

Besides the determination of the band gap, the leakage currents can be regarded to verify the good insulating properties. The current was measured between two Al contacts to evaluate the interplay of hexagonal $GdScO_3$ and GaN.

The leakage current densities of $GdScO_3$ on GaN are plotted as a function of EOT in Fig. 5.39 to compare its suitability as dielectric with other high-κ oxides. The $GdScO_3$ layers show leakage currents of $1.2 \times 10^{-8}\,\mathrm{Acm}^{-2}$ at 1 V applied voltage and at $EOT = 3\,\mathrm{nm}$ which is lower for PLD deposited amorphous $SmScO_3$. A comparison with other oxides is hindered because the EOT values achieved so far are rather high. Here further tests are needed to compare the leakage in the low EOT region to evaluate the suitability in low power devices.

Regarding high power applications the current density was observed for increasing electric field (voltage per oxide thickness) until the oxide collapsed and become conductive, compare Fig. 5.40. The soft breakdown typically started between $1\,\mathrm{MVcm}^{-1}$ and $1.7\,\mathrm{MVcm}^{-1}$. The hard breakdown set in at $2.2\,\mathrm{MVcm}^{-1}$ and $2.4\,\mathrm{MVcm}^{-1}$ for oxides layers with thicknesses of 16 nm and 23 nm to 39 nm, respectively. These values are an indication

Material	Phase	Growth template	Deposition temp. (°)	XPS E_g (eV)	Lit. E_g (eV)
$GdScO_3$	amorphous	Si	25	5.8 [150]	5.6 [5], 5.5 [146]
	orthorhombic	$LaAlO_3$	800	5.2 [150]	5.8 [146]
	hexagonal	GaN	680	5.2 [149]	
	hexagonal	Y_2O_3/Si	650	5.9	
	cubic	Y_2O_3/Si	550	5.2 [150]	
$LaLuO_3$	amorphous	Y_2O_3/Si	25	6.0	5.2 [9]
	orthorhombic	$SrTiO_3$	650	5.9	5.6 [6]
	hexagonal	Y_2O_3/Si	550	5.6 [161]	5.2 [153]
	hexagonal	Y_2O_3/Si	650	5.8	
	cubic	Y_2O_3/Si	800	6.0	
	cubic	GaN	900	6.0	
HfO_2	amorphous				6.0 [23]
Al_2O_3	amorphous				8.8 [23]

Table 5.5: Growth template, deposition temperature and band gap determined by XPS for the different polymorphs of $GdScO_3$ and $LaLuO_3$ in comparison to experimental band gap values found in other reports and in comparison to HfO_2 and Al_2O_3. The margin of error for the band gap values determined by XPS amounts to 0.2 eV.

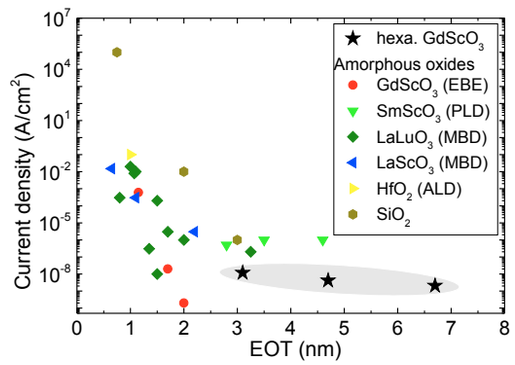

Figure 5.39: Leakage current density as a function of EOT (black stars) for hexagonal $GdScO_3$ layers grown on GaN. For comparison leakage current densities for other high-κ oxides are added adapted from [106].

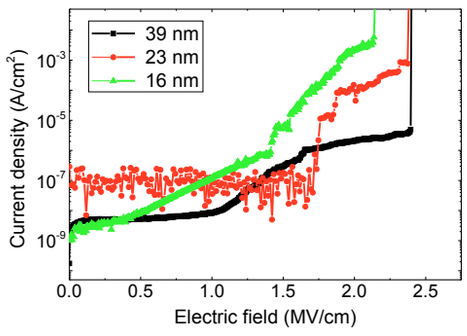

Figure 5.40: Representative leakage current density as a function of electric field for hexagonal $GdScO_3$ deposited on GaN to determine the dielectric breakdown for different layer thicknesses adapted from [150]. Breakdown electric fields between $2.2\,MVcm^{-1}$ and $2.4\,MVcm^{-1}$ are extracted.

for a stable oxide. In comparison, orthorhombic $GdScO_3$ on $SrTiO_3$ breaks down at electric fields of $1.2\,MVcm^{-1}$ [147] and amorphous $GdScO_3$ on InAlN/GaN at electric fields of $7\,MVcm^{-1}$ [126].

In conclusion, even though improvements are needed to achieve homogeneous GaN and $GdScO_3$ layers over the complete substrate, it was shown that low leakage currents and high breakdown electric fields can be accomplished by depositing hexagonal $GdScO_3$ on GaN for different layer thicknesses.

5.7 Excursus: Influence of $LaLuO_3$ on GaN characteristics

The main focus of this work is placed on the material characteristics of newly developed oxides and thus it was examined how the semiconducting substrate influences the oxide characteristics. Yet one can also explore how the epitaxial oxides influence the properties of the semiconductor. In this section some first attempts to disclose such phenomena are presented: in the case of hexagonal $LaLuO_3$ deposited on GaN the photoluminescence spectroscopy is studied and the Hall mobility of GaN are investigated as a function of oxide layer thickness.

5.7.1 Micro-photoluminescence

Fig. 5.41 represents the micro-photoluminescence (μ-PL) spectra of five GaN samples with different $LaLuO_3$ layer thicknesses. One can clearly see an increase in intensity with increasing oxide layer thickness. The band gap of hexagonal $LaLuO_3$, which is between $5.2\,eV$ and $5.8\,eV$ (compare Tab. 5.5), is larger than the wavelength of the μ-PL incident beam ($3.81\,eV$) and no interaction of the laser light with the oxide is expected. Hence,

the measured spectra have their origin in the GaN and the GaN is affected by the oxide thickness.

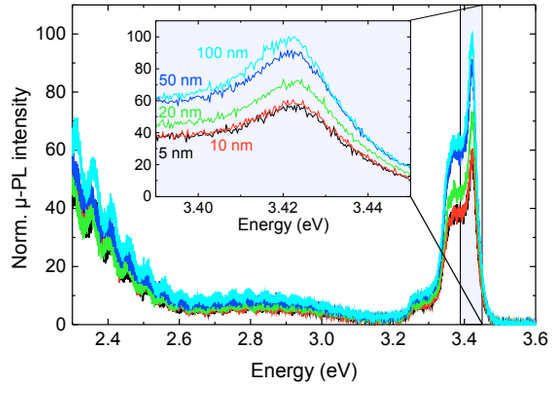

Figure 5.41: Micro photoluminescence intensity as a function of energy for different $LaLuO_3$ thicknesses. Inset: Zoom into the peak area of the spectrum.

The peak of the band edge luminescence at energies around 3.42 eV, which is close to the band gap value of 3.44 eV of GaN at 300 K [16], is analyzed in more detail in Fig. 5.41 as a function of oxide layer thickness. To achieve more accurate results, the extracted values are averaged over several measurements. The left axis shows the maximum μ-PL intensity of the investigated peak. The intensity is continuously rising and the value for 100 nm $LaLuO_3$ is almost the double of the one for 5 nm $LaLuO_3$. Further the respective positions (in terms of energy) of the peak maximum (Fig. 5.42 right axis, red circles) shows a very slight decrease, i.e. a 'red shift', as a function of oxide thickness in the range of meV.

There are several possible explanations for these effects. The hexagonal $LaLuO_3$ might induce strain in the underlying GaN. Strain alters the band gap and band alignment and possibly the number of charge carriers is increased without an increase in the number of positive ions which would produce carrier scattering. This would lead to a mobility increase. Such charge carriers also contribute to the photoluminescence signal (compare [171]). The $LaLuO_3$ might also have a passivation impact. For bare GaN surface states might be present due to roughness and defects which induce states in the band gap. Such surface states might be electrically neutralized by the $LaLuO_3$ top layer.

5.7.2 Hall measurements

Hall mobility measurements done on $LaLuO_3$/GaN with either Al or In contacts for different oxide layer thicknesses are summarized in Fig. 5.43 (a). Almost independent of the oxide thickness and the contact material the Hall mobility varies between 350 cm^2/Vs

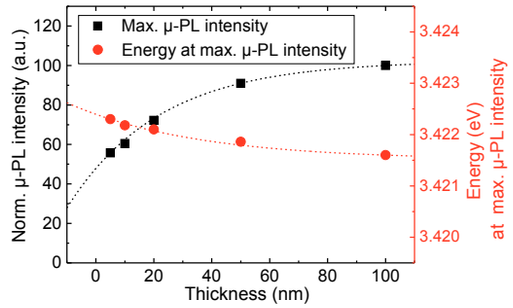

Figure 5.42: Maximum μ-PL intensity (left axis, black squares) and energy at maximum μ-PL intensity (right axis, red circles) as a function of $LaLuO_3$ layer thickness. Dashed lines are included as guide to the eye.

and 450 cm^2/Vs while the sample without $LaLuO_3$ shows considerably lower mobility of 280 cm^2/Vs.

In a second set of samples the ratio between the Si precursor (serving as GaN dopant) and the Ga precursor during MOVPE GaN growth was varied and the resulting carrier concentrations and Hall mobilities were extracted, compare Fig. 5.43 (b). For increasing amount of Si precursor the carrier concentration first rises, but decreases again for gas flow ratios Si:Ga above 0.5. For very high doping concentrations the defect density becomes so high, that so-called dislocation walls form derogating charge transport [172].

Furthermore one can observe that for increasing carrier concentration (left axis, black squares) the Hall mobility (right axis, red circles) is decreasing. This is typical for GaN, compare Mohammad et al. [121].

Yet, most interestingly for this work, the Hall mobility increases for GaN with a 30 nm $LaLuO_3$ top layer compared to bare GaN no matter what carrier concentration, even though the increase is lower than the one observed in the first set of samples presented in Fig. 5.43 (a), which is probably due to the higher carrier concentrations for the second set of samples.

Again, these effects of $LaLuO_3$ on GaN can have different origins, namely passivation of surface states or strain in the GaN induced due to the high lattice mismatch between $LaLuO_3$ and GaN.

These positive mobility effects of $LaLuO_3$ on GaN justify further experiments to elucidate the processes. The positive effects of $LaLuO_3$ on GaN could be beneficial for both high frequency devices which need highly insulating passivation layers on undoped GaN and for optoelectronics where effective insulators are needed on highly conductive GaN for the vertical integration of devices.

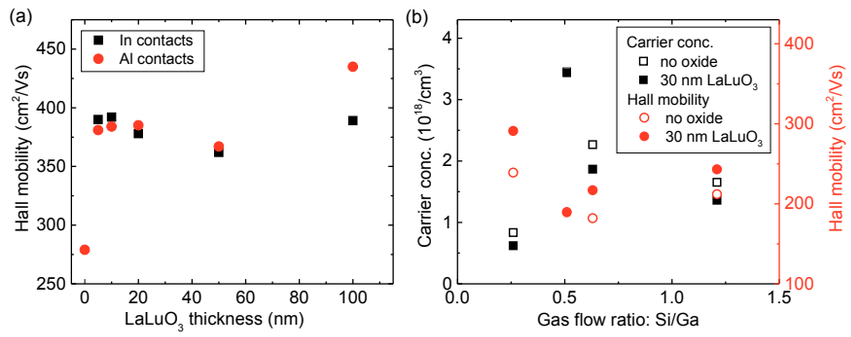

Figure 5.43: (a) GaN Hall mobility as a function of $LaLuO_3$ layer thickness for In (black) and Al (red) contacts. The GaN has carrier concentrations of (1-2) $\times 10^{17}/\mathrm{cm}^3$ (b) Carrier concentration (left axis, black squares) and Hall mobility (right axis, red circles) as a function of gas flow ratio of Si and Ga precursor during GaN growth for samples without (open symbols) and with (filled symbols) 30 nm $LaLuO_3$. The GaN thickness was around 1.5 μm and all samples were annealed for 170 s or longer to achieve better contact to GaN.

5.8 Discussion: Dielectric properties of $GdScO_3$ and $LaLuO_3$

The current chapter shows that in general the relatively unknown polymorphs of $GdScO_3$ and $LaLuO_3$ - the cubic and the hexagonal one - are suitable as gate dielectrics. The different crystalline phases all have band gaps above 5 eV and the variations in band gap values are rather small. Hence, it is expected that also the band offsets to the conduction and valence bands are similar and therefore sufficiently large for application.

Nevertheless, leakage issues were observed for measurements on GaN. Pinholes in the GaN itself, that could be observed by optical microscopy or AFM, are expected to be the origin for leakage currents. Hence, CV measurements on GaN should be repeated with higher quality GaN. Additionally, leakage currents could be determined if the epitaxial oxides could be stabilized directly on Si (111) without any additional Y_2O_3 or SiO_2. For this purpose the deposition technique needs to be changed. Due to the oxygen ambient during PLD deposition a SiO_2 interfacial layer forms. A possible alternative can be molecular beam deposition which takes place at much lower pressures.

The relative permittivity of cubic $GdScO_3$ of 14 is rather low, all other investigated oxides show high permittivities of 24-27. $GdScO_3$ fits well into the tendency for binary rare-earth oxides observed by Bonera et al.: they stated that they expect 1.5-2 times higher relative permittivity for hexagonal binary rare earth oxides of the composition A_2O_3 compared to the cubic ones [173]. So for $GdScO_3$ this rule can be extended. The case of $LaLuO_3$ is different: the relative permittivities in this work (24 or 27) hardly differ and Liu et al. even found a higher κ of ≈ 30 for cubic $LaLuO_3$. Eventually there are chances for an

enhancement of the permittivity. In the case of orthorhombic $LaLuO_3$ it was demonstrated that κ could be enlarged from 20 to 50 by increasing the substrate temperature during growth [10].

5.9 Summary

In conclusion, it is possible to stabilize the less investigated polymorphs of $GdScO_3$ and $LaLuO_3$ - the cubic and the hexagonal one - on different hexagonal growth templates by pulsed laser deposition. GaN and Y_2O_3 on Si(111) served as growth templates. The layers were analyzed with respect to their composition, crystal structure, homogeneity and crystallinity by RBS, XRD and TEM. Growth template and deposition temperature turned out to be the crucial parameters for crystal formation. Hexagonal oxides could be stabilized on GaN even though a large lattice mismatch was present. Cubic $GdScO_3$ and hexagonal $LaLuO_3$ are favored on relaxed Y_2O_3. For very thin Y_2O_3 also hexagonal $GdScO_3$ could be stabilized. Cubic $LaLuO_3$ formed on both growth templates for very high substrate temperatures.

For both hexagonal and cubic oxides the lattice constants were determined and models were proposed to construct the unit cells. All films presented showed atomically smooth interfaces and smooth surfaces with an *rms* roughness below 1 nm. Rocking curve measurements disclosed $FWHM$ values of 0.12° and below and it was shown that the crystallinity is limited by the substrates. Hence, the crystallinity can probably be improved by choosing substrates with superior crystallinity. Repeated XRD analysis after long periods of times proved that the presented ternary oxides are stable in air and do not degrade which enables device processing. Consequently, from the structural point of view, the hexagonal and cubic forms of $LaLuO_3$ and $GdScO_3$ can be integrated into devices.

All polymorphs of $GdScO_3$ and $LaLuO_3$ fulfill the precondition for dielectrics to exhibit a band gap above 5 eV. The high band gap value for $LaLuO_3$ was confirmed by ellipsometry investigations.

Leakage currents determined for hexagonal $GdScO_3$ deposited on GaN are low, e.g. lower than for amorphous $SmScO_3$ with equal EOT. This is important for high power or high frequency devices.

Capacitance voltage measurements disclosed the relative permittivities of the epitaxial oxides. Cubic $GdScO_3$ and $LaLuO_3$ demonstrated permittivities of 14 and 24, respectively, while hexagonal $LaLuO_3$ and $GdScO_3$ demonstrated higher relative permittivities above 25. Even though other oxides outperform the ones presented here, the hexagonal phases of $GdScO_3$ and $LaLuO_3$ can still be regarded as high-κ oxides exhibiting higher permittivity than standard amorphous HfO_2 ($\kappa \approx 21$ [8]).

First results of photoluminescence and Hall measurements for $LaLuO_3$ on GaN were presented. The enhanced mobility compared to GaN without oxide top layer for various carrier concentrations and layer thicknesses makes $LaLuO_3$ a promising candidate as a passivation layer for GaN devices even though the mechanism of the mobility enhancement still has to be explored.

The good homogeneity and crystallinity in combination with the good insulating and passivating properties and high permittivities make especially hexagonal $LaLuO_3$ and $GdScO_3$ promising candidates as passivation layer and gate dielectric. This might include high frequency and high power applications where highly insulating dielectrics are needed or optoelectronic devices based on highly conductive GaN which need a sufficient passivation to prevent mobility degradation.

In the future it would also be fascinating to test the growth of GaN on top of hexagonal ternary oxides on Si. This would be a big step forward towards on-chip integration of GaN on Si.

6 DFT calculations on $GdScO_3$ crystals

In order to gain better understanding on the formation of different crystal structures of $GdScO_3$, theoretical calculations were carried out determining the energy of formation of the different polymorphs. Further the conducted calculations allow to estimate lattice constants and the electrical band gap and the results are compared to the experimentally found values.

Density functional theory (DFT) which will be introduced in Section 6.1 provides the basis for these calculations which are done using the FLAPW approach (see Subsection 6.1.7). In Section 6.2 the results using this approach are presented and set into relation to the experimental data.

6.1 Introduction to DFT

6.1.1 Schrödinger equation

The ground state energy of a system of electrons and nuclei - the key parameter for the material properties of a closed system - is defined by the Schrödinger equation:

$$\hat{H}\,\Psi(\mathbf{r}_1, \mathbf{r}_2, ..., \mathbf{r}_N, \mathbf{R}_1, \mathbf{R}_2, ..., \mathbf{R}_M) = E\,\Psi(\mathbf{r}_1, \mathbf{r}_2, ..., \mathbf{r}_N, \mathbf{R}_1, \mathbf{R}_2, ..., \mathbf{R}_M), \tag{6.1}$$

where $\hat{H}$ represents the Hamiltonian operator, E the total energy of the system and Ψ the wave function of the system which depends on the radii of the N electrons $\mathbf{r}_i$ with $i = 1...N$ and of the M nuclei $\mathbf{R}_j$ with $j = 1...M$ [174].

In the Born-Oppenheimer approximation where the motion of the nuclei is neglected due to their massive masses compared to the electrons, the Hamiltonian - here and in the following equations expressed in atomic units - reduces to:

$$\begin{aligned}\hat{H} &= \hat{T} + \hat{V}_{ext} + \hat{V}_{ee} \\ &= -\frac{1}{2}\sum_{i}^{N}\nabla_i^2 - \sum_{i=1}^{N}\sum_{j=1}^{M}\frac{Z_j}{|\mathbf{r}_i - \mathbf{R}_j|} + \sum_{i<j}^{N}\frac{1}{|\mathbf{r}_i - \mathbf{r}_j|}\end{aligned} \tag{6.2}$$

As can be seen from equation 6.2 the Hamiltonian consists of three terms: the kinetic energy of the N electrons $\hat{T}$, the interactions with an external potential $\hat{V}_{ext}$ due to the frozen nuclei and the electron electron interactions $\hat{V}_{ee}$ [174].

To solve the Schrödinger equation for a complex system like a bulk crystal simplifications and approximations are needed. Density functional theory offers a powerful starting point to reach a computationally feasible solution.

6.1.2 Basic principle of DFT

The main benefit of introducing DFT is to reduce the number of variables. While in the many-body description a 3N-dimensional wave function is used to describe all N electrons which is impossible to store even for a single Fe-atom ($N = 26$), DFT reduces the problem to a function of 3 variables (x, y and z) by describing the energy as a functional of the electron density - $E(\rho)$ [175]. This way the computing time for any calculation can be reduced in principle without loosing an exact solution of the Schrödinger equation.

The electron density $\rho(\mathbf{r})$ gives the probability to find an electron at point $\mathbf{r}$. It is a positive function which vanishes at infinity ($\rho(\mathbf{r} \longrightarrow \infty) = 0$) in the case of a finite system and the integral over $\rho(\mathbf{r})$ gives the total number of electrons N: $\int \rho(\mathbf{r}) d\mathbf{r}) = N$ [174].

Hohenberg and Kohn proved two theorems that substantiate the density functional theory. The first one states that the external potential is uniquely determined (to within a constant) by the electron density and therefore also $\hat{H}$ depends only on ρ [174]. The second theorem states that for each external potential $\hat{V}_{ext}$ there exists a functional $F[\rho]$ which leads to the ground state energy and delivers the minimum energy if and only if the entered density is the ground state density. In other words all trial densities $\tilde{\rho}$ fulfilling the boundary condition $\int \rho(\tilde{\mathbf{r}}) d\mathbf{r} = N$ give an energy which is equal to or greater than the ground state energy: $E[\tilde{\rho}] \geq E_0$. This corresponds to the variational principle [176].

6.1.3 Kohn-Sham Equations

Kohn and Sham demonstrated an approach to approximate the electron density by expressing the real density by a fictive set of wave functions that are not interacting [174]. This way the sum in the Schrödinger equation vanishes and the Kohn-Sham equations describe single electron wave functions:

$$\left[\tilde{T} + V_{ext}(\mathbf{r}) + V_H(\mathbf{r}) + V_{XC}(\mathbf{r})\right] \psi_i(\mathbf{r}) = \epsilon_i \psi_i(\mathbf{r}). \tag{6.3}$$

$\tilde{T}$ depicts the kinetic energy of the non-interacting electron, V_{ext} describes the interaction of the electron with the nuclei and V_H is called the Hartree potential and considers the Coulomb repulsion between the electron and the total electron density:

$$\tilde{T} = -\frac{\hbar^2}{2m}\nabla^2, \tag{6.4}$$

$$V_{ext} = -\sum_{j=1}^{M} \frac{Z_j}{|\mathbf{r}_i - \mathbf{R}_j|}, \tag{6.5}$$

$$V_H(\mathbf{r}) = e^2 \int \frac{\rho(\mathbf{r'})}{|\mathbf{r} - \mathbf{r'}|} d^3r'. \tag{6.6}$$

The exchange correlation potential, the last potential in equation 6.3, V_{XC}, describes all

exchange and correlation effects that are not considered in the first three terms:

$$V_{xc} = (V_{ee} - V_H) + (T - \tilde{T}) \tag{6.7}$$

The exchange correlation potential is small and represents the part which is not known exactly and to find a sufficient description for V_{xc} is the major goal of DFT [176]. In the Kohn-Sham approach as much as possible is calculated exactly and only the remaining part - V_{xc} - is approximated using a functional derived either from analytically known properties or semi-empirically [174].

Many approaches, including the LAPW method (see below) used here, employ a set of basis functions ϕ_α and expansion coefficients $c_{i\alpha}$ to describe the single electron wave function ψ_i:

$$\psi_i(\mathbf{r}) = \sum_\alpha c_{i\alpha}\phi_\alpha(\mathbf{r}). \tag{6.8}$$

Thus $c_{i\alpha}$ are the only variables in the problem [177].

6.1.4 Self-consistency in DFT

Typically the determination of the potential (which depends on charge density) and of the charge density (which depends on the potential) are separated and done alternately. As depicted in the schematic of a standard self-consistency circle in Fig. 6.1 after starting with some trial density ρ_{in} the single particle equations are solved and the energy is determined. From these the electron density ρ_{out} can be calculated and compared to ρ_{in}. If they fit within a certain margin, the two densities are considered to be self consistent and the calculations are finished, otherwise the loop starts again with a new ρ_{in} typically composed of the old ρ_{in} and ρ_{out} [177].

When using approximations to solve the Kohn-Sham Equations by the variational principle, one has to keep in mind that the minimum energy for a chosen functional is just an approximated energy and not the real one. The better the approximation is, the more decreases the difference between the estimated value and the real energy minimum of the system.

6.1.5 Local Density Approximation and Generalized Gradient Approximation

Since the exact form of the exchange-correlation potential V_{xc} is not known, an approximation is needed. The simplest form is to suppose a locally uniform electron gas so that $\rho(\mathbf{r}) =$ constant. This is done in the local density approximation (LDA) and leads to a V_{xc}

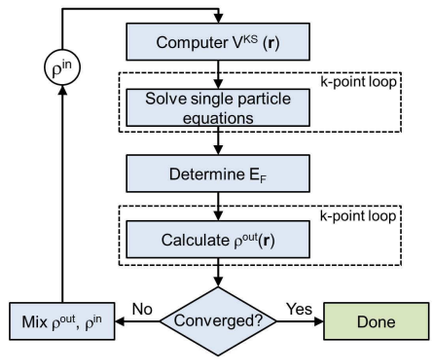

Figure 6.1: Schematics for self consistent DFT calculations to solve single particle Kohn-Sham equations hierarchically, adapted from [177].

that is a function of the density: $V_{xc}(\mathbf{r}) = f(\rho(\mathbf{r}))$. Although this approximation is quite rough it can deliver useful results (see also [176]).
An expansion of the LDA is the Generalized Gradient Approximation (GGA). It uses not only the local electron density but also the gradient of the electron density. More constraints have to be added and there are several approaches to include this gradient of the electron density. Therefore a variety of distinct LDA functionals is used (see also [176]).

6.1.6 "Muffin-tin" approach and augmented plane wave method

In the 'muffin-tin' approach space is divided into spheres with radius S around the atoms (MT) and the interstitial region between those spheres (IR) like depicted in Fig. 6.2. The sketch nicely explains the name of the approach because it looks like a top view of a pan for making muffins.

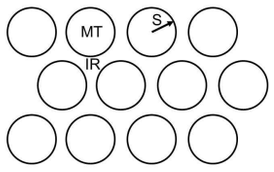

Figure 6.2: 'Muffin-tin' approach to solve the Kohn-Sham equations: Space is subdivided into atomic spheres (muffin tins - MT) of radius S and the interstitial region (IR). Wave functions can be defined differently for the two regions. Sketch modified from [175].

In the augmented plane wave (APW) method this division of space is used to define the effective potential ($V_{eff} = V_{ext} + V_H + V_{xc}$). For example in former times in the interstitial the potential was set constant because it is rather smooth and inside the spheres it was assumed to be spherically symmetric because potential and wave function are similar to those of a single atom [175, 177]. Inside these spheres the wave functions can be written in terms of radial functions of spherical harmonics describing well the highly-localized core-states. Plane waves are used in the interstitial region and cover the delocalized states [175]. The single wave functions can be written as a sum of APW basis functions:

$$\psi_{\mathbf{k},\nu}(\mathbf{r}) = \sum_{|\mathbf{G}+\mathbf{k}| \leq K_{max}} c^{\mathbf{G}}_{\mathbf{k},\nu} \varphi_{\mathbf{G}}(\mathbf{k},\mathbf{r}) \tag{6.9}$$

with $\mathbf{k}$ the Bloch vector in reciprocal space, $\mathbf{G}$ the reciprocal lattice vectors up to a maximum value of K_{max}, ν the band index, $c^{\mathbf{G}}_{\mathbf{k},\nu}$ variational coefficients and $\varphi_{\mathbf{G}}(\mathbf{k},\mathbf{r})$ the APW basis functions defined as:

$$\varphi_{\mathbf{G}}(\mathbf{k}) = \begin{cases} exp(i(\mathbf{k}+\mathbf{G})\mathbf{r}) & \text{IR} \\ \sum_{l,m}(a^{\mu,\mathbf{G}}_{l,m}(\mathbf{k}) u_l(r^\mu|E)) Y_{l,m}(\hat{\mathbf{r}}^\mu) & \text{MT } \mu. \end{cases} \tag{6.10}$$

Here r^μ describes the distance to the center of the sphere or muffin-tin μ, $\hat{r}$ is the angular part of $\mathbf{r}$, l and m are the quantum numbers, $Y_{l,m}$ are the spherical harmonics and u_l are the regular solutions of the radial Schrödinger equation:

$$\left[-\frac{d^2}{dr^2} + \frac{l(l+1)}{r^2} + V(r) - E \right] r u_l(r) = 0. \tag{6.11}$$

The functions u_l defined that way are automatically orthogonal [177, 178]. The coefficients $a^{\mu,\mathbf{G}}_{l,m}(\mathbf{k})$ are giving by the boundary condition that the radial solutions match the plane waves at the border of the spheres [178]. Plane waves were chosen in the interstitial because they solve the Schrödinger equation for a constant potential and the radial functions are solutions for a spherical potential with eigenvalue E_l [177].

One drawback of the APW method is that the energy E has to be chosen as a variable depending on ν leading to a non-linear eigenvalue problem. Therefore solving the equation can not just be done by simple diagonalization [178]. It is also worth mentioning that for the APW method the derivative of the wave functions have a discontinuity at the boundary leading to a modified kinetic energy operator $T = (\nabla\psi)^*\nabla$ [175].

6.1.7 The FLAPW approach

Linearizing the APW ansatz facilitates the solution of the Schrödinger equation. In the linearized APW (LAPW) method the basis functions inside the MT spheres are expanded

by including also the first energy derivative $\dot{u}_l$ which is orthogonal to u_l. u_l is defined as before but with E replaced by a linearization energy E_l and $\dot{u}_l$ is defined by:

$$\left[-\frac{d^2}{dr^2}+\frac{l(l+1)}{r^2}+V(r)-E_l\right]r\dot{u}_l(r)=ru_l(r). \tag{6.12}$$

The wave functions are extended to:

$$\varphi_{\mathbf{G}}(\mathbf{k})=\begin{cases} exp(i(\mathbf{k}+\mathbf{G})\mathbf{r}) & \text{IR} \\ \sum_{l,m}(a_{lm}^{\mu,\mathbf{G}}(\mathbf{k})u_l^{\mu}(r)+b_{lm}^{\mu,\mathbf{G}}(\mathbf{k})\dot{u}_l^{\mu}(r))Y_{lm}(\hat{\mathbf{r}}^{\mu}) & \text{MT } \mu. \end{cases} \tag{6.13}$$

In this case the coefficients $a_{lm}^{\mu,\mathbf{G}}(\mathbf{k})$ and $b_{lm}^{\mu,\mathbf{G}}(\mathbf{k})$ are determined by demanding that $\varphi_{\mathbf{G}}(\mathbf{k})$ and its derivative are continuous at the boundary. Now the energy can be fixed to E_l chosen according to the principal quantum number of the electron that should be calculated and the set of linear equations can be solved by diagonalization [177, 178].

The LAPW method using a spherical-shape approximation inside the MT regions works nicely for closed-packed metal systems but not any more for open structures like semiconductor surfaces. In the full-potential LAPW (FLAPW) the shape approximation is removed.
To describe the Coulomb potential for a general periodic charge distribution in an accurate way can lead to numerical difficulties due to the singularities at the core. Therefore, the so-called pseudocharge is introduced. This can be done because the potential outside a localized charge distribution depends on the charge only through multipole moments. These in turn are not unique and may also be described correctly by a pseudocharge. If the pseudocharge is chosen in that way that its Fourier representation converges rapidly and that it has the same multipoles as the real charge distribution, the exact Coulomb potential can be evaluated outside the spheres. The potential inside the spheres is then found by using the real charge density in this region and by applying the boundary conditions [179].
The FLAPW method is an all-electron algorithm which considers the shape of the charge density, the effective potential and the wave function with high accuracy. Further it offers reasonable computational efficiency. Therefore this quite robust method is widely used to simulate electronic properties of various materials [178].

6.1.8 FLEUR code

The FLEUR code is a freely available program package on the basis of the FLAPW method and was developed and continuously advanced in the 'Quantum-Theory of Materials' (PGI-1/IAS-1) group at the Forschungszentrum Jülich GmbH in cooperation with other groups. For detailed information see [180].
In collaboration with the PGI-1 the FLEUR code was used to gain more insight into the structure and material properties of the experimentally found hexagonal $GdScO_3$ which is treated in detail in this work.

6.2 Results from DFT calculations

For the data presented here the generalized gradient approximation (GGA) was used for the exchange correlation potential and the FLAPW method was chosen for the calculations.

All three crystalline phases found experimentally for $GdScO_3$ (orthorhombic, hexagonal and cubic) were considered and optimized to find the minimum energy of formation and the corresponding lattice constants. For comparison also cubic and hexagonal Gd_2O_3 and Sc_2O_3 were considered. The mean total energy of the bixbyite phases of these two binary oxides was set to zero as reference for the $GdScO_3$ energies of formation.

The *Pbnm* structure was chosen as space group of orthorhombic $GdScO_3$ which is experimentally confirmed [143]. The cubic phase of $GdScO_3$ is less explored. Therefore a bixbyite structure was chosen. When starting the calculations no information was available about the space group of hexagonal $GdScO_3$, hence, several possible unit cells were explored. The simplest one is an ordered in-plane hexagonal phase with alternating Sc and Gd layers in the out-of-plane direction. The other hexagonal models can be regarded as alloys with larger unit cells.

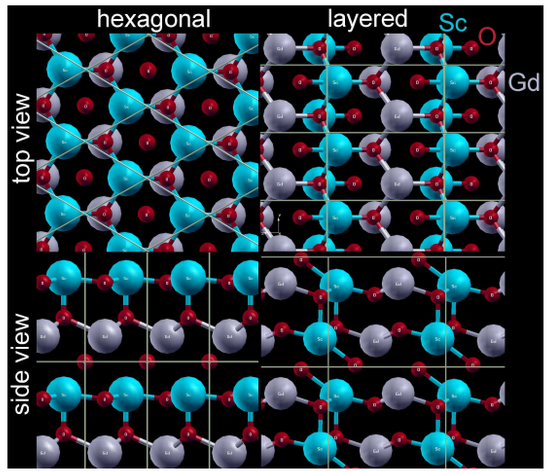

Figure 6.3: Structure schemes for two different structures considered in the DFT calculations for the hexagonal case shown as top view (upper pictures) and side view (lower pictures). The left structure represents a typical hexagonal one, the right picture has the same hexagonal texture, but has to be described in an orthorhombic space group rather than in a hexagonal one due to its periodicity.

Fig. 6.3 presents two of the hexagonal structures studied in DFT calculations shown as top view (upper part) and side view (lower part). The structure on the left is a real hexagonal one with Gd and Sc atoms positioned alternately at the corners of the hexagons.

	DFT			Experiment		
Lattice constant (nm)	a	b	c	a	b	c
Orthorhombic [143]	0.546	0.573	0.790	0.54862	0.57499	0.79345
Hexagonal [149]	0.359		0.571	0.360 ± 0.002		0.585 ± 0.002
Cubic [150]	1.026			1.040 ± 0.002		

Table 6.1: Lattice constants for orthorhombic, hexagonal and cubic $GdScO_3$ extracted from DFT calculations and experiments [150].

The layered structure in the right part of Fig. 6.3 also shows hexagonal planes but can not be described in a hexagonal space group. To correctly describe a structure with such a periodicity an orthorhombic space group has to be used. Nevertheless the two structures are closely related to each other and the minimization of the energy in DFT reveals equal lattice constants. Even more structures with a hexagonal in-plane geometry were considered in DFT giving the same lattice constants and slightly varying energies of formation (compare Fig. 6.4).

6.2.1 Lattice constants and energies

The lattice constants derived from the optimized unit cells are summarized in Tab. 6.1 and compared to the experimentally found values. For the hexagonal and cubic structures the differences between the calculated and measured values are less than 0.02 nm which is within the margin of error for the values derived from XRD in this work. The difference between the experimental lattice constants for the orthorhombic structure from literature and the calculated ones is even smaller: it does not exceed 0.003 nm.

These results show on the one hand that the approximations and methods chosen for DFT nicely match the real crystals. On the other hand one might conclude that the hexagonal and cubic layers measured in this work are fully relaxed or otherwise larger differences would be expected for the lattice constants.

The energies of formation which correspond to the unit cells described by the DFT lattice parameters in Tab. 6.1 are depicted in Fig. 6.4. While the energies of the cubic and orthorhombic phases are almost equal, the hexagonal unit cells reveal much higher energies: the ordered hexagonal form is energetically 340 meV per formula unit above the stable orthorhombic phase. For comparison, calculations on $LaLuO_3$ show that the difference between the hexagonal and orthorhombic phase is just about 60 meV per formula unit [152]. The differences between the various alloys of $GdScO_3$ with in plane hexagonal geometry are lower than the one to the orthorhombic phase and the ordered hexagonal structure on the left in Fig. 6.3 is one of the most stable hexagonal forms.

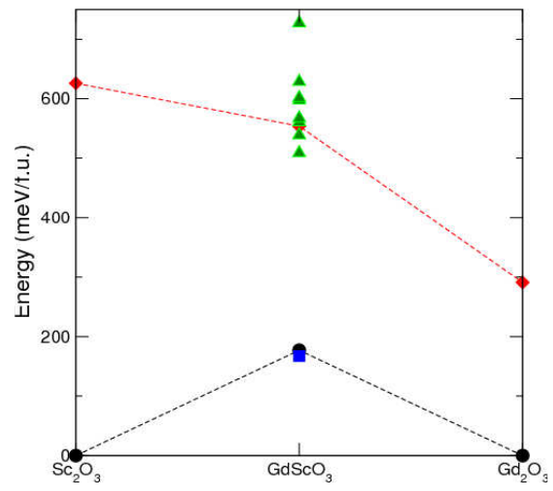

Figure 6.4: Energy of formation for cubic (black circle), orthorhombic (blue square), ordered hexagonal (red diamond) and hexagonally alloyed (green triangles) $GdScO_3$ in comparison to Sc_2O_3 and Gd_2O_3 [150]. The mean total energy of bixbyite Sc_2O_3 and Gd_2O_3 was chosen as the energy reference points.

6.2.2 Band gap determination by DFT

When calculating the energies ϵ_i for the different quantum numbers $i = (k, \nu)$ and for various reciprocal lattice vectors $\mathbf{k}$ (compare Section 6.1.3) one can depict band diagrams of the three crystalline polymorphs of $GdScO_3$ and extract the band energies. The results for the band gaps are summarized in Tab. 6.2 and compared to the experimental values.

The calculations disclose band gaps of 4.65 eV, 4.4 eV and 4.15 eV for orthorhombic, hexagonal and cubic $GdScO_3$, respectively. All values are underestimated compared to the

	Methods		
E_g (eV)	DFT	XPS	Lit.
Amorphous		5.8 ± 0.2	5.6 ± 0.1 [5]
Orthorhombic	4.65	5.2 ± 0.2	5.8 [146]
Hexagonal	4.40	5.2 ± 0.2	
Cubic	4.15	5.2 ± 0.2	

Table 6.2: Band gap for amorphous, orthorhombic, hexagonal and cubic $GdScO_3$ calculated by DFT and experimental values either determined by XPS or found in literature [150].

experimentally found values but this is typical for DFT. The underestimation is due to a missing derivative-discontinuity in the exchange correlation functional [181]. The relative differences for the DFT values are rather small; the experimental values are very similar within the margin of error of 0.2 eV. Hence, experiment and DFT calculations are not contradictory taking into account the typical underestimation of E_g in DFT.

6.3 Discussion

The energy values derived by DFT give indications on the dominant factor for the formation of a crystalline structure during film growth. Experiments have demonstrated that hexagonal $GdScO_3$ forms when deposited on hexagonal growth templates such as GaN (0001) (compare Chapter 5). Two parameters actually should hinder this formation of the hexagonal phase: the huge energy of formation compared to cubic and orthorhombic $GdScO_3$ and the large lattice mismatch of 13 % to GaN. Hence, the substrate and kinetic effects in the initial stages of growth have to be the crucial factors to determine the formation of the crystal. Possibly GaN being a polar material favors a polar hexagonal form of $GdScO_3$ compared to the unpolar cubic or orthorhombic phases.

In summary, one can conclude that for the Y_2O_3/Si template the influences of lattice mismatch and of the energy of formation almost compensate each other when considering whether the hexagonal or the cubic phase of $GdScO_3$ forms. Slight changes in lattice constant of the substrate can change the system. This does not hold for the case of GaN growth templates. Here a large lattice mismatch and large energies of formation actually hinder the hexagonal phase and the polarity of the GaN seems to be the most reasonable explanation for the experimentally observed growth of hexagonal $GdScO_3$ on GaN.

Such as for $GdScO_3$ the hexagonal form of $LaLuO_3$ on GaN is quite surprising taking into account the huge lattice mismatch of 17 %. Other than for $GdScO_3$, DFT calculations for $LaLuO_3$ by Watahiki et al. revealed that the energy of formation of a hexagonal form is lower than the one of the cubic bixbyite one [152]. This energy tendency corresponds to the observed lattice type tendency as a function of temperature. Nevertheless, also for $LaLuO_3$ the energetically most favored form is the orthorhombic one [152].

7 Conclusion

Within the framework of this thesis doped HfO_2 films and epitaxial rare-earth based oxides were developed for the application in nanotechnology. The aim was to find oxides for both Si and GaN transistor technology with eminent structural and dielectric properties, i.e. high layer quality, good insulating properties, low defect densities and, in particular, high relative permittivities.

A standard ALD HfO_2 process based on ozone was extended to deposit HfO_2 thin films doped with different amounts of either Al, Lu, La or Er on Si substrates. The films had smooth interfaces and surfaces with surface roughnesses below $rms = 0.5\,\mathrm{nm}$.

Al doped HfO_2 with an Al content of 11 at. % and annealed in Ar at 700°C after deposition showed an optimized relative permittivity of 30 which is considerably higher than for HfO_2 ($\kappa = 18$). The augmentation of κ can be explained by a phase transition: HfO_2 is typically either amorphous or monoclinic, while the Al doped HfO_2 showed a polycrystalline structure with both a monoclinic portion and a 'higher κ' polymorph, most probably the cubic form of HfO_2. Leakage current densities through $Hf_{0.89}Al_{0.11}O_{2-\Delta}$ films followed the same dependency as a function of the equivalent oxide thickness (EOT) as those observed for HfO_2. Thus, doping and phase transformation did not degrade the insulating properties. The density of interfacial traps D_{it} can be reduced by doping and annealing to $7 \times 10^{11}\,\mathrm{eV^{-1}cm^{-2}}$.

Doping HfO_2 with Lu or Er also leads to greater relative permittivities: $Hf_{0.8}Lu_{0.2}O_{2-\Delta}$ and $Hf_{0.89}Er_{0.11}O_{2-\Delta}$ demonstrated $\kappa = 33$ and 32, respectively. Also these films were polycrystalline. The lattice distances extracted point out that the cubic form is dominant which is expected to have higher κ than monoclinic or amorphous HfO_2. $Hf_{0.8}Lu_{0.2}O_{2-\Delta}$ showed a slightly higher band gap than HfO_2 with $E_g = 5.8\,\mathrm{eV}$ and good insulating properties. At an EOT of 1.5 nm leakage current densities of ca. $10^{-8}\,\mathrm{A/cm^2}$ at (V_{fb}−1 V) were determined. From the fact that no exponential increase with decreasing layer thickness was observed it could be deduced that tunneling currents did not affect the conduction yet for EOT down to 1.5 nm. Densities of interfacial traps amounted to $10^{12}\,\mathrm{eV^{-1}cm^{-2}}$.

Hence, by slight modifications of a standard HfO_2 deposition process the dielectric properties of the oxide thin films could be improved. Both, $Hf_{0.8}Lu_{0.2}O_{2-\Delta}$ and $Hf_{0.89}Al_{0.11}O_{2-\Delta}$ exhibited enhanced permittivity. While $Hf_{0.89}Al_{0.11}O_{2-\Delta}$ stands out due to a low D_{it}, $Hf_{0.8}Lu_{0.2}O_{2-\Delta}$ demonstrated improved insulating properties without the need for additional post deposition anneals.

The studies demonstrated high layer quality and good dielectric characteristics of the newly developed oxides. Since they can easily be implemented into standard $TiN/HfO_2/Si$ based gate stacks, they are suitable as gate dielectric for Si nanotechnology. To prove

their suitability for down scaled devices, future efforts should focus on the reduction of the interfacial SiO_2 thickness.

When searching for a dielectric for the use in GaN based transistors, a different approach was studied. The epitaxy of rare-earth based oxides by PLD on GaN was investigated with the aim to find high permittivity oxides with high quality interfaces. $GdScO_3$ and $LaLuO_3$ were chosen since the orthorhombic phases of these oxides proved to have high permittivities.

When depositing on GaN at temperatures around 550°C a novel phase of those oxides formed which was hexagonal. The lattice constants of $GdScO_3$ ($a = 0.360\,\mathrm{nm}$ and $c = 0.585\,\mathrm{nm}$) and $LaLuO_3$ ($a = 0.375\,\mathrm{nm}$ and $c = 0.612\,\mathrm{nm}$) and the orientation of the crystals were determined. The crystallinity of the oxides was limited by the growth template. The lattice mismatch between $GdScO_3$ and $LaLuO_3$ to GaN was 13 % and 17 %, respectively. For high deposition temperatures around 900°C $LaLuO_3$ became cubic with $a = 10.86\,\mathrm{nm}$.

Cubic $Y_2O_3\,(111)$ on $Si\,(111)$ was introduced as alternative growth template because it can serve as substrate for the growth of GaN. While $LaLuO_3$ was again present in the hexagonal phase along (0001) on top of Y_2O_3/Si, $GdScO_3$ crystallized in a cubic form with $a = 10.40\,\mathrm{nm}$ along (111) just like the underlying Y_2O_3. Again, $LaLuO_3$ transformed into the cubic phase for elevated temperatures, in this case at $T \approx 800°\mathrm{C}$.

$GdScO_3$ could be forced into the hexagonal phase by reduction of the Y_2O_3 layer thickness to approximately 1 nm. However, the crystallinity of the hexagonal $GdScO_3$ on the Si based growth template was clearly reduced and an amorphization at the interface took place as could be seen in TEM images.

Epitaxial layers of cubic $GdScO_3$ and hexagonal and cubic $LaLuO_3$ on Y_2O_3/Si showed high crystallinity with rocking curve widths of $FWHM \approx 0.6°$. Furthermore all films on both growth templates had atomically smooth interfaces and smooth surfaces with roughnesses of $rms \leqslant 1\,\mathrm{nm}$.

The fact that the hexagonal phase of $LaLuO_3$ stabilizes at lower temperatures than the cubic one matches calculations revealing that the hexagonal form has a lower energy of formation than the cubic one [152].

For $GdScO_3$ the energies of formation follow a different trend. While cubic and orthorhombic $GdScO_3$ have almost equal energies of formation, the one for hexagonal $GdScO_3$ is almost 500 meV per formula unit higher. Thus it is very surprising that hexagonal $GdScO_3$ stabilizes on GaN. Since also the lattice mismatch is quite high, the growth kinetics of the first atomic layers have to be crucial. Possibly on the polar substrate also a polar oxide is favored.

Dielectric characterization of the epitaxial oxides revealed that cubic $GdScO_3$ has a rather low relative permittivity $\kappa = 14$. The hexagonal form and cubic and hexagonal $LaLuO_3$ all exhibit higher κ between 23 and 27. Band gaps were determined for all polymorphs of $GdScO_3$ and $LaLuO_3$ by XPS: all crystals featured band gaps between 5 eV and 6 eV. The $LaLuO_3$ band gaps were typically a little higher than the $GdScO_3$ band gaps.

Current voltage measurements confirm the good insulating properties of hexagonal $GdScO_3$ on GaN. For EOT down to 3 nm the leakage stayed as low as $1.2 \times 10^{-8}\,\mathrm{Acm}^{-2}$ at 1 V.

Breakdown of the hexagonal films set in above $2\,\mathrm{MVcm}^{-1}$.

The smooth layers with high crystallinity, relative permittivities above 24 and good insulating properties make hexagonal $GdScO_3$ and $LaLuO_3$ promising candidates as gate dielectric for hexagonal III-V semiconductors such as GaN. GaN with low density of pin holes and high crystallinity would be required to obtain optimal results for application. In future studies, a broader range of rare earth ternary oxides will be investigated in order to gain more insights on why a certain polymorph is stable and to possibly find the perfectly lattice matched oxide for GaN or other hexagonal III-V semiconductors. Applications can go far beyond gate dielectrics, e.g. the epitaxial oxides might be used as a buffer layer to implement GaN on Si.

Bibliography

[1] D.G. Schlom, S. Guha, and S. Datta. Gate Oxides Beyond SiO_2. *MRS Bulletin*, 33:1017–1025, 2008.

[2] G. D. Wilk, R. M. Wallace, and J. M. Anthony. High-κ gate dielectrics: Current status and materials properties considerations. *Journal of Applied Physics*, 89(10):5243–5275, 2001.

[3] D. P. Norton. Synthesis and properties of epitaxial electronic oxide thin-film materials. *Materials Science and Engineering: R: Reports*, 43(5-6):139 – 247, 2004.

[4] J. Robertson. High dielectric constant gate oxides for metal oxide Si transistors. *Reports on Progress in Physics*, 69(2):327, 2006.

[5] V. V. Afanas'ev, A. Stesmans, C. Zhao, M. Caymax, T. Heeg, J. Schubert, Y. Jia, D. G. Schlom, and G. Lucovsky. Band alignment between (100)Si and complex rare earth/transition metal oxides. *Applied Physics Letters*, 85(24):5917–5919, 2004.

[6] D. G. Schlom and J. H. Haeni. A Thermodynamic Approach to Selecting Alternative Gate Dielectrics. *MRS Bulletin*, 27:198–204, 2002.

[7] S. Coh, T. Heeg, J. H. Haeni, M. D. Biegalski, J. Lettieri, L. F. Edge, K. E. O'Brien, M. Bernhagen, P. Reiche, R. Uecker, S. Trolier-McKinstry, D. G. Schlom, and D. Vanderbilt. Si-compatible candidates for high-κ dielectrics with the Pbnm perovskite structure. *Physical Review B*, 82(6):064101, 2010.

[8] K. Cherkaoui, S. Monaghan, M. A. Negara, M. Modreanu, P. K. Hurley, D. O'Connell, S. McDonnell, G. Hughes, S. Wright, R. C. Barklie, P. Bailey, and T. C. Q. Noakes. Electrical, structural, and chemical properties of HfO_2 films formed by electron beam evaporation. *Journal of Applied Physics*, 104(6), Sep. 15 2008.

[9] J. M. J. Lopes, M. Roeckerath, T. Heeg, E. Rije, J. Schubert, S. Mantl, V. V. Afanas'ev, S. Shamuilia, A. Stesmans, Y. Jia, and D. G. Schlom. Amorphous lanthanum lutetium oxide thin films as an alternative high-κ gate dielectric. *Applied Physics Letters*, 89(22):222902, 2006.

[10] J. Schubert, O. Trithaveesak, W. Zander, M. Roeckerath, T. Heeg, H. Y. Chen, C. L. Jia, P. Meuffels, Y. Jia, and D. G. Schlom. Characterization of epitaxial lanthanum lutetium oxide thin films prepared by pulsed-laser deposition. *Applied Physics A-materials Science & Processing*, 90(3):577–579, March 2008.

[11] S. B. Ogale. *Thin films and heterostructures for oxide electronics [E-Book]*. Springer, Boston, MA, p. 31-85. 2005.

[12] S.-G. Lim, S. Kriventsov, T. N. Jackson, J. H. Haeni, D. G. Schlom, A. M. Balbashov, R. Uecker, P. Reiche, J. L. Freeouf, and G. Lucovsky. Dielectric functions and optical bandgaps of high-κ dielectrics for metal-oxide-semiconductor field-effect transistors by far ultraviolet spectroscopic ellipsometry. *Journal of Applied Physics*, 91(7):4500–4505, 2002.

[13] H. Ibach and H. Lüth. *Festkörperphysik Einführung in die Grundlagen*. Springer, Berlin, 7th edition, p. 23, 443–455. 2009.

[14] F. C. Frank. On Miller–Bravais indices and four-dimensional vectors. *Acta Crystallographica*, 18(5):862–866, May 1965.

[15] J. F. Nicholas. The simplicity of Miller–Bravais indexing. *Acta Crystallographica*, 21(6):880–881, Dec 1966.

[16] S. M. Sze. *Physics of semiconductor devices*. Wiley, New York, NY, 3rd ed. edition, p. 57, 197-235, 789. 2007.

[17] J.W. Matthews and A.E. Blakeslee. Defects in epitaxial multilayers: I. Misfit dislocations. *Journal of Crystal Growth*, 27(0):118–125, December 1974.

[18] J.W. Matthews and A.E. Blakeslee. Defects in epitaxial multilayers: II. Dislocation pile-ups, threading dislocations, slip lines and cracks. *Journal of Crystal Growth*, 29(3):273–280, July 1975.

[19] J.W. Matthews and A.E. Blakeslee. Defects in epitaxial multilayers: III. Preparation of almost perfect multilayers. *Journal of Crystal Growth*, 32(2):265–273, February 1976.

[20] S. M. Sze and M. K. Lee. *Semiconductor devices: physics and technology*. Wiley, New York, NY, 2nd. ed. edition, p. 191, 435–437. 2002.

[21] Dieter K. Schroder. *Semiconductor material and device characterization*. Wiley, New York, NY, 3rd ed. edition, p. 63, 347–350. 2006.

[22] S. Gupta, R. Chen, J. S. Harris, and K. C. Saraswat. Atomic layer deposition of Al_2O_3 on germanium-tin (GeSn) and impact of wet chemical surface pre-treatment. *Applied Physics Letters*, 103(24):–, 2013.

[23] J. Robertson. Band offsets of wide-band-gap oxides and implications for future electronic devices. *Journal of Vacuum Science & Technology B*, 18(3):1785–1791, 2000.

[24] R. Kassing. *Festkörper*. De Gruyter, Berlin, Boston, p. 731–732. 2008.

[25] H. G. Tompkins and E. A. Irene. *Handbook of Ellipsometry*. William Andrew Publishing, Springer, Norwich NY, p. 24, 264. 2005.

[26] S. Roberts. Dielectric Constants and Polarizabilities of Ions In Simple Crystals and Barium Titanate. *Physical Review*, 76(8):1215–1220, 1949.

[27] R. D. Shannon. Dielectric polarizabilities of ions in oxides and fluorides. *Journal of Applied Physics*, 73(1):348–366, 1993.

[28] S. Guha and V. Narayanan. High-κ/Metal Gate Science and Technology. *Annual Review of Materials Research*, 39(1):181–202, 2009.

[29] Y.-C. Yeo, T.-J. King, and C. Hu. Metal-dielectric band alignment and its implications for metal gate complementary metal-oxide-semiconductor technology. *Journal of Applied Physics*, 92(12):7266–7271, 2002.

[30] J. K. Schaeffer, S. B. Samavedam, D. C. Gilmer, V. Dhandapani, P. J. Tobin, J. Mogab, B.-Y. Nguyen, B. E. White, S. Dakshina-Murthy, R. S. Rai, Z.-X. Jiang, R. Martin, M. V. Raymond, M. Zavala, L. B. La, J. A. Smith, R. Garcia, D. Roan, M. Kottke, and R. B. Gregory. Physical and electrical properties of metal gate electrodes on HfO_2 gate dielectrics. *Journal of Vacuum Science & Technology B*, 21(1):11–17, 2003.

[31] H. Y. Yu, M.-F. Li, and D.-L. Kwong. Thermally robust HfN metal as a promising gate electrode for advanced MOS device applications. *Electron Devices, IEEE Transactions on*, 51(4):609–615, April 2004.

[32] T.-H. Cha, D.-G. Park, T.-K. Kim, S.-A. Jang, I.-S. Yeo, J.-S. Roh, and J. W. Park. Work function and thermal stability of $Ti_{1-x}Al_xN_y$ for dual metal gate electrodes. *Applied Physics Letters*, 81(22):4192–4194, 2002.

[33] R. J. Hillard, J. M. Heddleson, D. A. Zier, P. Rai-Choudhury, and D. K. Schroder. *Diagnostic Techniques For Semiconductor Materials and Devices*. Electrochemical Society, Pennington, NJ, p. 261–274. 1992.

[34] E. H. Nicollian and J. R. Brews. *MOS (metal oxide semiconductor) physics and technology*. Wiley, Hoboken, NY, Wiley classics library ed. edition, p. 9, 477–489. 2003.

[35] O. Engström. *The MOS System*. Cambridge University Press, p. 11–12, 241–256, 308–330. 2014.

[36] E.H. Nicollian and A. Goetzberger. The Si-SiO_2 interface-electrical properties as determined by the metal-insulator-silicon conductance technique. *The Bell System Technical Journal*, 46(6):1055–1033, July 1967.

[37] W. Shockley and W. T. Read. Statistics of the Recombinations of Holes and Electrons. *Physical Review*, 87:835–842, Sep 1952.

[38] K. Tomida, K. Kita, and A. Toriumi. Higher-κ Scalability and Leakage Current Reduction of SiO_2-Doped HfO_2 in Direct Tunneling Regime. *Japanese Journal of Applied Physics*, 50(11R):111502, 2011.

[39] L. Tarnawska, A. Giussani, P. Zaumseil, M. A. Schubert, R. Paszkiewicz, O. Brandt, P. Storck, and T. Schroeder. Single crystalline Sc_2O_3/Y_2O_3 heterostructures as novel engineered buffer approach for GaN integration on Si (111). *Journal of Applied Physics*, 108(6):063502, 2010.

[40] W. Kern and Da. Puotinen. Cleaning solutions based on hydrogen peroxide for use in silicon semiconductor technology. *RCA Review*, 31(2):187, 1970.

[41] M. L. Green, M.-Y. Ho, B. Busch, G. D. Wilk, T. Sorsch, T. Conard, B. Brijs, W. Vandervorst, P. I. Räisänen, D. Muller, M. Bude, and J. Grazul. Nucleation and growth of atomic layer deposited HfO_2 gate dielectric layers on chemical oxide (Si-O-H) and thermal oxide (SiO_2 or Si-O-N) underlayers. *Journal of Applied Physics*, 92(12):7168–7174, 2002.

[42] A. C. Jones and M. L. Hitchman. Chapter 1 Overview of Chemical Vapour Deposition. In *Chemical Vapour Deposition: Precursors, Processes and Applications*, pages 1–36. The Royal Society of Chemistry, 2009.

[43] G. B. Stringfellow. *Organometallic vapor phase epitaxy : theory and practice.* Academic Press, INC., Boston, p. 26–34. 1989.

[44] H. Hardtdegen, N. Kaluza, R. Steins, P. Javorka, K. Wirtz, A. Alam, T. Schmitt, and R. Beccard. Uniform III-nitride growth in single wafer horizontal MOVPE reactors. *Physica Status Solidi A - Applications and Materials Science*, 202(5):744–748, April 2005.

[45] M. Ritala and J. Niinisto. Chapter 4 Atomic Layer Deposition. In *Chemical Vapour Deposition: Precursors, Processes and Applications*, pages 158–206. The Royal Society of Chemistry, 2009.

[46] R. L. Puurunen. Surface chemistry of atomic layer deposition: A case study for the trimethylaluminum/water process. *Journal of Applied Physics*, 97(12):121301, 2005.

[47] U. Weber, M. Schumacher, J. Lindner, O. Boissié, P. Lehnen, S. Miedl, P.K. Baumann, G. Barbar, C. Lohe, and T. McEntee. AVD® technology for deposition of next generation devices. *Microelectronics and Reliability*, 45(5-6):945 – 948, 2005. 13th Workshop on Dielectrics in Microelectronics.

[48] M. Siegert. *Wachstumsuntersuchungen an Bariumtitanat-Dünnschichten, hergestellt mit gepulster Laserdeposition.* PhD thesis, Universität Köln, 2001.

[49] D. M. Mattox. Chapter 6 - Vacuum Evaporation and Vacuum Deposition. In D. M. Mattox, editor, *Handbook of Physical Vapor Deposition (PVD) Processing (Second Edition)*, pages 206–208. William Andrew Publishing, Boston, 2010.

[50] T. L. Alford, L. C. Feldman, and J. W. Mayer. Fundamentals of nanoscale film analysis [E-Book], 2007.

[51] http://www.genplot.com/rump/index.htm.

[52] M. Sardela. Practical Materials Characterization edited by Mauro Sardela. [E-Book] , 2014.

[53] G. Binnig, C. F. Quate, and Ch. Gerber. Atomic Force Microscope. *Phys. Rev. Lett.*, 56:930–933, Mar 1986.

[54] J. B. Nelson and D. P. Riley. An experimental investigation of extrapolation methods in the derivation of accurate unit-cell dimensions of crystals. *Proceedings of the Physical Society*, 57(3):160, 1945.

[55] P. Scherrer. Bestimmung der Grosse und der Inneren Struktur von Kolloidteilchen Mittels Rontgenstrahlen. *Nachr. Kgl. Gesell. Wiss. Gottingen Math.-Phys Kl*, pages 98–100, 1918.

[56] XRDC - X-Ray Data Collector; see www.theeg.de.

[57] http://www.bam.de/de/service/publikationen/powder_cell.htm.

[58] https://sourceforge.net/projects/plotpy/.

[59] F. Wendt. Investigations of the Structural Properties of Ternary Rare-Earth Based Oxides By Transmission Electron Microscopy. Master's thesis, RWTH Aachen University, 2014.

[60] S. Miyazaki. Characterization of high-k gate dielectric/silicon interfaces. *Applied Surface Science*, 190:66 – 74, 2002.

[61] G. E. Jellison Jr. Data Analysis for Spectroscopic Ellipsometry. In E. A. Irene and H. G. Tompkins, editors, *Handbook of Ellipsometry*, page 264. William Andrew Publishing, Norwich, NY, 2005.

[62] http://www.jawoollam.com/wvase.html.

[63] C. Hu. Modern Semiconductor Devices for Integrated Circuits, Chapter 5 MOS Capacitor, http://www.eecs.berkeley.edu/ hu/, 2010.

[64] L. Bergman and J. L. McHale. Handbook of luminescent semiconductor materials [E-Book], 2012.

[65] P. K. Park and S.-W. Kang. Enhancement of dielectric constant in HfO_2 thin films by the addition of Al_2O_3. *Applied Physics Letters*, 89(19):192905, 2006.

[66] K. Tomida, K. Kita, and A. Toriumi. Dielectric constant enhancement due to Si incorporation into HfO_2. *Applied Physics Letters*, 89(14):142902, 2006.

[67] E. Rauwel, C. Dubourdieu, B. Holländer, N. Rochat, F. Ducroquet, M. D. Rossell, G. Van Tendeloo, and B. Pelissier. Stabilization of the cubic phase of HfO_2 by Y addition in films grown by metal organic chemical vapor deposition. *Applied Physics Letters*, 89(1):012902, 2006.

[68] C. Adelmann, V. Sriramkumar, S. Van Elshocht, P. Lehnen, T. Conard, and S. De Gendt. Dielectric properties of dysprosium- and scandium-doped hafnium dioxide thin films. *Applied Physics Letters*, 91(16):162902, 2007.

[69] T. S. Böscke, S. Govindarajan, P. D. Kirsch, P. Y. Hung, C. Krug, B. H. Lee, J. Heitmann, U. Schröder, G. Pant, B. E. Gnade, and W. H. Krautschneider. Stabilization of higher-κ tetragonal HfO_2 by SiO_2 admixture enabling thermally stable metal-insulator-metal capacitors. *Applied Physics Letters*, 91(7):072902, 2007.

[70] K. Kita, K. Kyuno, and A. Toriumi. Permittivity increase of yttrium-doped HfO_2 through structural phase transformation. *Applied Physics Letters*, 86(10):102906, 2005.

[71] C. Wiemer, L. Lamagna, S. Baldovino, M. Perego, S. Schamm-Chardon, P. E. Coulon, O. Salicio, G. Congedo, S. Spiga, and M. Fanciulli. Dielectric properties of Er-doped HfO_2 (Er15%) grown by atomic layer deposition for high-κ gate stacks. *Applied Physics Letters*, 96(18):182901, 2010.

[72] C.-K. Lee, E. Cho, H.-S. Lee, C. S. Hwang, and S. Han. First-principles study on doping and phase stability of HfO_2. *Physical Review B*, 78:012102, Jul 2008.

[73] D. Fischer and A. Kersch. The effect of dopants on the dielectric constant of HfO_2 and ZrO_2 from first principles. *Applied Physics Letters*, 92(1):012908, 2008.

[74] D. Fischer and A. Kersch. Stabilization of the high-κ tetragonal phase in HfO_2: The influence of dopants and temperature from ab initio simulations. *Journal of Applied Physics*, 104(8):084104, 2008.

[75] L. Passerini. Isoformismo tra ossidi di metalli tetravalenti. I sistemi: Ce O2 - Th O2; Ce O2 - Zr O2; Ce O2 - Hf O2. *Gazzetta Chimica Italiana*, 60:762–776, 1930.

[76] J. E. Jaffe, R. A. Bachorz, and M. Gutowski. Low-temperature polymorphs of ZrO_2 and HfO_2: A density-functional theory study. *Physical Review B*, 72:144107, Oct 2005.

[77] R. Ruh and P. W. R. Corfield. Crystal Structure of Monoclinic Hafnia and Comparison with Monoclinic Zirconia. *Journal of the American Ceramic Society*, 53(3):126–129, 1970.

[78] R. Suyama, H. Horiuchi, and S. Kume. Structural Refinements of ZrO_2 and HfO_2 Treated at 600°C · 6GPa. *Journal of the Ceramic Association, Japan*, 95(1102):567–568, 1987.

[79] J. Wang, H.P. Li, and R. Stevens. Hafnia and hafnia-toughened ceramics. *Journal of Materials Science*, 27(20):5397–5430, 1992.

[80] X. Zhao and D. Vanderbilt. First-principles study of structural, vibrational, and lattice dielectric properties of hafnium oxide. *Physical Review B*, 65:233106, Jun 2002.

[81] P. S. Lysaght, J. C. Woicik, M. A. Sahiner, B.-H. Lee, and R. Jammy. Characterizing crystalline polymorph transitions in HfO_2 by extended x-ray absorption fine-structure spectroscopy. *Applied Physics Letters*, 91(12):122910, 2007.

[82] C. Adelmann, H. Tielens, D. Dewulf, A. Hardy, D. Pierreux, J. Swerts, E. Rosseel, X. Shi, M. K. Van Bael, J. A. Kittl, and S. Van Elshocht. Atomic Layer Deposition of Gd-Doped HfO_2 Thin Films. *Journal of The Electrochemical Society*, 157(4):G105–G110, 2010.

[83] J. M. Leger, P. E. Tomaszewski, A. Atouf, and A. S. Pereira. Pressure-induced structural phase transitions in zirconia under high pressure. *Physical Review B*, 47:14075–14083, Jun 1993.

[84] G.-M. Rignanese, X. Gonze, G. Jun, K. Cho, and A. Pasquarello. First-principles investigation of high-κ dielectrics: Comparison between the silicates and oxides of hafnium and zirconium. *Physical Review B*, 69:184301, May 2004.

[85] A. Navrotsky. Thermochemical insights into refractory ceramic materials based on oxides with large tetravalent cations. *Journal of Materials Chemistry*, 15:1883–1890, 2005.

[86] K. Momma and F. Izumi. *VESTA3* for three-dimensional visualization of crystal, volumetric and morphology data. *Journal of Applied Crystallography*, 44(6):1272–1276, Dec 2011.

[87] G. Dutta. A first-principles study of enhanced dielectric responses in Ti and Ce doped HfO_2. *Applied Physics Letters*, 94(1):012907–2, 2009.

[88] V. Fiorentini and G. Gulleri. Theoretical Evaluation of Zirconia and Hafnia as Gate Oxides for Si Microelectronics. *Physical Review Letters*, 89:266101, 2002.

[89] D. Fischer and A. Kersch. Ab initio study of high permittivity phase stabilization in HfSiO. *Microelectronic Engineering*, 84(9-10):2039 – 2042, 2007.

[90] M.S. Kim, Y.D. Ko, M.S. Yun, J.H. Hong, M.C. Jeong, J.M. Myoung, and I.G. Yun. Characterization and process effects of HfO_2 thin films grown by metal-organic molecular beam epitaxy. *Materials Science and Engineering B - Solid State Materials for Advances Technology*, 123(1):20–30, Nov 15 2005.

[91] N. Wu, Q. Zhang, C. Zhu, C. C. Yeo, S. J. Whang, D. S. H. Chan, M. F. Li, B.J. Cho, A. Chin, D.-L. Kwong, A. Y. Du, C. H. Tung, and N. Balasubramanian. Effect of surface NH_3 anneal on the physical and electrical properties of HfO_2 films on Ge substrate. *Applied Physics Letters*, 84(19):3741–3743, 2004.

[92] K. Kukli, M. Ritala, T. Sajavaara, J. Keinonen, and M. Leskela. Atomic layer deposition of hafnium dioxide films from hafnium tetrakis(ethylmethylamide) and water. *Chemical Vapor Deposition*, 8(5):199–204, Sep 2002.

[93] K. Kukli, M. Ritala, J. Sundqvist, J. Aarik, J. Lu, T. Sajavaara, M. Leskela, and A. Harsta. Properties of hafnium oxide films grown by atomic layer deposition from hafnium tetraiodide and oxygen. *Journal of Applied Physics*, 92(10):5698–5703, Nov 15 2002.

[94] M. Balog, M. Schieber, M. Michman, and S. Patai. Chemical vapor deposition and characterization of HfO2 films from organo-hafnium compounds . *Thin Solid Films*, 41(3):247 – 259, 1977.

[95] D. Ceresoli and D. Vanderbilt. Structural and dielectric properties of amorphous ZrO_2 and HfO_2. *Physical Review B*, 74:125108, Sep 2006.

[96] S. Govindarajan, T. S. Böscke, P. Sivasubramani, P. D. Kirsch, B. H. Lee, H.-H. Tseng, R. Jammy, U. Schröder, S. Ramanathan, and B. E. Gnade. Higher permittivity rare earth doped HfO_2 for sub-45-nm metal-insulator-semiconductor devices. *Applied Physics Letters*, 91(6):062906, 2007.

[97] C. Wiemer, L. Lamagna, and M. Fanciulli. Atomic layer deposition of rare-earth-based binary and ternary oxides for microelectronic applications. *Semiconductor Science and Technology*, 27(7):074013, 2012.

[98] A. Lamperti, L. Lamagna, G. Congedo, and S. Spiga. Cubic/Tetragonal Phase Stabilization in High-κ ZrO_2 Thin Films Grown Using O_3-Based Atomic Layer Deposition. *Journal of The Electrochemical Society*, 158(10):G221–G226, 2011.

[99] S. Van Elshocht, C. Adelmann, M. Popovici, J. Swerts, A. Delabie, L. Nyns, X. Shi, H. Tielens, G. Pourtois, N. Menou, L. Breuil, D. Pierreux, J. W. Maes, A. Hardy, M. K. Van Bael, M. Jurczak, and J. A. Kittl. On the process and material sensitivities for high-κ based dielectrics. *China Semiconductor Technology International Conference 2010*, 27(1):693–698, 2010.

[100] Atomic weights of the elements. *Pure and Applied Chemistry*, 21:91, 1969.

[101] H. Ono and T. Katsumata. Interfacial reactions between thin rare-earth-metal oxide films and Si substrates. *Applied Physics Letters*, 78(13):1832–1834, 2001.

[102] E. D. Palik, editor. *Handbook of optical constants of solids*. Academic Press, NY, San Diego, Calif., 1998.

[103] D. A. G. Bruggeman. Berechnung verschiedener physikalischer Konstanten von heterogenen Substanzen. I. Dielektrizitaetskonstanten und Leitfaehigkeiten der Mischkoerper aus isotropen Substanzen. *Annalen der Physik*, 416(7):636–664, 1935.

[104] G. E. Jellison and F. A. Modine. Parameterization of the optical functions of amorphous materials in the interband region. *Applied Physics Letters*, 69(3):371–373, 1996.

[105] J. I. Pankove. *Optical processes in semiconductors*. New York: Dover Publications [etc.]; London: Constable, 1976. Semiconductors. Optical properties (BNB/PRECIS).

[106] E. Durğun Özben. *Carrier mobility in advanced channel materials using alternative gate dielectrics*. PhD thesis, RWTH Aachen, Jülich, 2014.

[107] H. M. Otte. Lattice Parameter Determinations with an X-Ray Spectrogoniometer by the Debye Scherrer Method and the Effect of Specimen Condition. *Journal of Applied Physics*, 32(8):1536–1546, 1961.

[108] M. Birkholz and P. F. Fewster. *Thin film analysis by x-ray scattering*. Wiley-VCH, Weinheim, p. 70. 2006.

[109] S. Ramanathan, A. Karthikeyan, S. A. Govindarajan, and P. D. Kirsch. Synthesis of nitrogen passivated rare-earth doped hafnia thin films and high temperature electrochemical conduction studies. *Journal of Vacuum Science & Technology B*, 26(4):L33–L35, 2008.

[110] T. Ando, M.M. Frank, K. Choi, C. Choi, J. Bruley, M. Hopstaken, M. Copel, E. Cartier, A Kerber, A Callegari, D. Lacey, S. Brown, Q. Yang, and V. Narayanan. Understanding mobility mechanisms in extremely scaled HfO_2 (EOT 0.42 nm) using remote interfacial layer scavenging technique and Vt-tuning dipoles with gate-first process. In *Electron Devices Meeting (IEDM), 2009 IEEE International*, pages 1–4, Dec 2009.

[111] A. Nichau, A. Schäfer, L. Knoll, S. Wirths, T. Schram, L.-A. Ragnarsson, J. Schubert, P. Bernardy, M. Luysberg, A. Besmehn, U. Breuer, D. Buca, and S. Mantl. Reduction of silicon dioxide interfacial layer to 4.6 A EOT by Al remote scavenging in high-κ metal gate stacks on Si. *Microelectronic Engineering*, 109:109 – 112, 2013.

[112] X. Y. Zhao and D. Vanderbilt. First-principles study of electronic and dielectric properties of ZrO_2 and HfO_2. In Ginley, D. and Guha, S. and Carter, S. and Chambers, S.A. and Droopad, R. and Hosono, H. and Paine, D.C. and Schlom, D.G. and Tate, J., editor, *Crystalline Oxide-Silicon Heterostructures and Oxide Optoelectronics*, volume 747 of *Materials Research Society Symposium Proceedings*, pages 93–98, 2003.

[113] L. Wu, H. Y. Yu, K. L. Pey, J. S. Pan, M. Tuominen, Eva Tois, D. Y. Lee, K. Y. Hsu, K. T. Huang, H. J. Tao, and Y. J. Mii. Electrical and Physical Properties of Er-Doped HfO_2 High-κ Dielectrics Prepared by Atomic Layer Deposition. *Electrochemical and Solid State Letters*, 13(2):G21–G23, 2010.

[114] A. Toriumi, K. Kita, K. Tomida, and Y. Yamamoto. Doped HfO_2 for Higher-κ Dielectrics. *ECS Transactions*, 1(5):185–197, July 2006.

[115] Michael Shandalov and Paul C. McIntyre. Size-dependent polymorphism in HfO_2 nanotubes and nanoscale thin films. *Journal of Applied Physics*, 106(8):–, 2009.

[116] S. Fabris, A. T. Paxton, and M. W. Finnis. A stabilization mechanism of zirconia based on oxygen vacancies only. *Acta Materialia*, 50(20):5171–5178, 2002.

[117] D.-Y. Cho, H. S. Jung, I.-H. Yu, J. H. Yoon, H. K. Kim, S. Y. Lee, S. H. Jeon, S. Han, J. H. Kim, T. J. Park, B.-G. Park, and C. S. Hwang. Stabilization of Tetragonal HfO_2 under Low Active Oxygen Source Environment in Atomic Layer Deposition. *Chemistry of Materials*, 24(18):3534–3543, 2012.

[118] H. Kim, A. Marshall, P. C. McIntyre, and K. C. Saraswat. Crystallization kinetics and microstructure-dependent leakage current behavior of ultrathin HfO_2 dielectrics: In situ annealing studies. *Applied Physics Letters*, 84(12):2064–2066, 2004.

[119] O. Ambacher. Growth and applications of Group III-nitrides. *Journal of Physics D: Applied Physics*, 31(20):2653, 1998.

[120] S. Strite, M.E. Lin, and H. Morkoç. Progress and prospects for GaN and the Si and III-V nitride semiconductors. *Thin Solid Films*, 231(1-2):197 – 210, 1993.

[121] S. N. Mohammad, A. A. Salvador, and H. Morkoc. Emerging gallium nitride based devices. *Proceedings of the IEEE*, 83(10):1306–1355, Oct 1995.

[122] S. J. Pearton and C. Kuo. GaN and Related Materials for Device Applications. *MRS Bulletin*, 22:17–21, 2 1997.

[123] Y. Yue, Y. Hao, J. Zhang, J. Ni, W. Mao, Q. Feng, and L. Liu. GaN MOS-HEMT with HfO_2 dielectric and Al_2O_3 interfacial passivation layer grown by atomic layer deposition. *IEEE Electron Device Letters*, 29(8):838–840, Aug 2008.

[124] D. Gregušová, R. Stoklas, Ch. Mizue, Y. Hori, J. Novák, T. Hashizume, and P. Kordoš. Trap states in AlGaN/GaN metal-oxide-semiconductor structures with Al_2O_3 prepared by atomic layer deposition. *Journal of Applied Physics*, 107(10):106104, 2010.

[125] T. Hashizume. Characterization and control of insulated gates for GaN power switching transistors. *ASDAM 2012 - Conference Proceedings: The 9th International Conference on Advanced Semiconductor Devices and Microsystems*, pages 31–36, 2012.

[126] K. Čičo, K. Hušeková, M. Ťapajna, D. Gregušová, R. Stoklas, J. Kuzmík, J.-F. Carlin, N. Grandjean, D. Pogany, and K. Fröhlich. Electrical properties of InAlN/GaN high electron mobility transistor with Al_2O_3, ZrO_2, and $GdScO_3$ gate dielectrics. *Journal of Vacuum Science & Technology B*, 29(1):01A808–4, 2011.

[127] D. Gregušová, K. Hušeková, R. Stoklas, M. Blaho, M. Jurkovič, J.-F. Carlin, N. Grandjean, and P. Kordoš. ZrO_2/InAlN/GaN Metal-Oxide-Semiconductor Heterostructure Field-Effect Transistors with InAlN Barrier of Different Compositions. *Japanese Journal of Applied Physics*, 52:08JN07, 2013.

[128] G. Heidelberger, M. Roeckerath, R. Steins, M. Stefaniak, A. Fox, J. Schubert, N. Kaluza, M. Marso, H. Lueth, and P. Kordos. Technology related issues regarding fabrication of AlGaN/GaN-based MOSHFETs with $GdScO_3$ as dielectric. In Breza, J. and Donoval, D. and Vavrinsky, E., editor, *ASDAM '06: Sixth International Conference on Advanced Semiconductor Devices and Microsystems, Conference Proceedings*, pages 241–244. IEEE, 2006.

[129] S. Yang, S. Huang, H. Chen, C. Zhou, Q. Zhou, M. Schnee, Q.-T. Zhao, J. Schubert, and K. J. Chen. AlGaN/GaN MISHEMTs With High-κ $LaLuO_3$ Gate Dielectric. *IEEE Electron Device Letters*, 33(7):979–981, July 2012.

[130] B. P. Gila, J. W. Johnson, R. Mehandru, B. Luo, A. H. Onstine, K. K. Allums, V. Krishnamoorthy, S. Bates, C. R. Abernathy, F. Ren, and S. J. Pearton. Gadolinium oxide and scandium oxide: Gate dielectrics for GaN MOSFETs. *Physica Status Solidi A-Applied Research*, 188(1):239–242, 2001.

[131] W. H. Chang, C. H. Lee, P. Chang, Y. C. Chang, Y. J. Lee, J. Kwo, C. C. Tsai, J. M. Hong, C. H. Hsu, and M. Hong. High κ dielectric single-crystal monoclinic Gd_2O_3 on GaN with excellent thermal, structural, and electrical properties. *Journal of Crystal Growth*, 311(7):2183–2186, March 15 2009.

[132] Y. Liu, M. Xu, J. Heo, P. D. Ye, and R. G. Gordon. Heteroepitaxy of single-crystal $LaLuO_3$ on GaAs(111)A by atomic layer deposition. *Applied Physics Letters*, 97(16):162910, 2010.

[133] X. Wang, L. Dong, J. Zhang, Y. Liu, P. D. Ye, and R. G. Gordon. Heteroepitaxy of La_2O_3 and $La_{2-x}Y_xO_3$ on GaAs (111)A by Atomic Layer Deposition: Achieving Low Interface Trap Density. *Nano Letters*, 13(2):594–599, February 2013.

[134] A. Krost and A. Dadgar. GaN-based optoelectronics on silicon substrates. *Materials Science and Engineering: B*, 93(1-3):77 – 84, 2002.

[135] http://www.crystalimpact.com/diamond/.

[136] C.-H. Liu, P.-C. Juan, C.-P. Cheng, G.-T. Lai, H. Lee, Y.-K. Chen, Y.-W. Liu, and C.-W. Hsu. Structural properties of ultra-thin Y_2O_3 gate dielectrics studied by X-Ray diffraction (XRD) and X-Ray photoelectron spectroscopy (XPS). In *Nanoelectronics Conference (INEC), 2010 3rd International*, pages 1256–1257, Jan 2010.

[137] M. Wagner, T. Heeg, J. Schubert, St. Lenk, S. Mantl, C. Zhao, M. Caymax, and S. De Gendt. Gadolinium scandate thin films as an alternative gate dielectric prepared by electron beam evaporation. *Applied Physics Letters*, 88(17):172901–3, 2006.

[138] K. H. Kim, D. B. Farmer, J.-S. M. Lehn, P. Venkateswara Rao, and R. G. Gordon. Atomic layer deposition of gadolinium scandate films with high dielectric constant and low leakage current. *Applied Physics Letters*, 89(13):–, 2006.

[139] P. Myllymäki, M. Roeckerath, M. Putkonen, S. Lenk, J. Schubert, L. Niinistö, and S. Mantl. Characterization and electrical properties of high-κ $GdScO_3$ thin films grown by atomic layer deposition. *Applied Physics A*, 88(4):633–637, 2007.

[140] M. Roeckerath, J.M.J. Lopes, E. Durğun Özben, C. Sandow, S. Lenk, T. Heeg, J. Schubert, and S. Mantl. Gadolinium scandate as an alternative gate dielectric in field effect transistors on conventional and strained silicon. *Applied Physics A*, 94(3):521–524, 2009.

[141] V.M. Goldschmidt. Die Gesetze der Krystallochemie. *Naturwissenschaften*, 14(21):477–485, 1926.

[142] M. R. Levy. *Crystal structure and defect property predictions in ceramic materials*. PhD thesis, University of London, London, 2005.

[143] R. P. Liferovich and R. H. Mitchell. A structural study of ternary lanthanide orthoscandate perovskites. *Journal of Solid State Chemistry*, 177(6):2188 – 2197, 2004.

[144] R. Uecker, H. Wilke, D.G. Schlom, B. Velickov, P. Reiche, A. Polity, M. Bernhagen, and M. Rossberg. Spiral formation during Czochralski growth of rare-earth scandates. *Journal of Crystal Growth*, 295(1):84 – 91, 2006.

[145] B. Veličkov, V. Kahlenberg, R. Bertram, and M. Bernhagen. Crystal chemistry of $GdScO_3$, $DyScO_3$, $SmScO_3$ and $NdScO_3$. *Zeitschrift Für Kristallographie*, 222(9):466–473, 2007.

[146] T. Heeg, M. Wagner, J. Schubert, C. Buchal, M. Boese, M. Luysberg, E. Cicerrella, and J. L. Freeouf. Rare-earth scandate single- and multi-layer thin films as alternative gate oxides for microelectronic applications. *Microelectronic Engineering*, 80:150–153, 2005.

[147] T. Heeg, J. Schubert, C. Buchal, E. Cicerrella, J.L. Freeouf, W. Tian, Y. Jia, and D.G. Schlom. Growth and properties of epitaxial rare-earth scandate thin films. *Applied Physics A*, 83(1):103–106, 2006.

[148] H. M. Christen, G. E. Jellison, I. Ohkubo, S. Huang, M. E. Reeves, E. Cicerrella, J. L. Freeouf, Y. Jia, and D. G. Schlom. Dielectric and optical properties of epitaxial rare-earth scandate films and their crystallization behavior. *Applied Physics Letters*, 88(26):–, 2006.

[149] A. Schäfer, A. Besmehn, M. Luysberg, A. Winden, T. Stoica, M. Schnee, W. Zander, G. Niu, T. Schroeder, S. Mantl, H. Hardtdegen, M. Mikulics, and J. Schubert. Hexagonal $GdScO_3$: an epitaxial high-κ dielectric for GaN. *Semiconductor Science and Technology*, 29(7):075005, 2014.

[150] A. Schäfer, K. Rahmanizadeh, G. Bihlmayer, M. Luysberg, F. Wendt, A. Besmehn, A. Fox, M. Schnee, G. Niu, T. Schroeder, S. Mantl, H. Hardtdegen, M. Mikulics,

and J. Schubert. Polymorphous $GdScO_3$ as high permittivity dielectric. *Journal of Alloys and Compounds*, 651:514 – 520, 2015.

[151] J. M. J. Lopes, E. Durgun Oezben, M. Roeckerath, U. Littmark, R. Luptak, St Lenk, M. Luysberg, A. Besmehn, U. Breuer, J. Schubert, and S. Mantl. Amorphous ternary rare-earth gate oxides for future integration in MOSFETs. *Microelectronic Engineering*, 86(7-9):1646–1649, 2009.

[152] T. Watahiki, F. Grosse, W. Braun, V. M. Kaganer, A. Proessdorf, A. Trampert, and H. Riechert. Epitaxial growth and structure of $(La_{1-x}Lu_x)_2O_3$ alloys on Si(111). *Applied Physics Letters*, 97(3):031911, 2010.

[153] V. V. Afanas'ev, M. Badylevich, A. Stesmans, A. Laha, H. J. Osten, A. Fissel, W. Tian, L. F. Edge, and D. G. Schlom. Band offsets between Si and epitaxial rare earth sesquioxides (RE2O3, RE=La,Nd,Gd,Lu): Effect of 4f-shell occupancy. *Applied Physics Letters*, 93(19):192105, 2008.

[154] E. Durğun Özben, J. M. J. Lopes, A. Nichau, M. Schnee, S. Lenk, A. Besmehn, K. K. Bourdelle, Q. T. Zhao, J. Schubert, and S. Mantl. Integration of $LaLuO_3$ (κ similar to 30) as High-κ Dielectric on Strained and Unstrained SOI MOSFETs With a Replacement Gate Process. *IEEE Electron Device Letters*, 32(1):15–17, January 2011.

[155] C. Volk, J. Schubert, M. Schnee, K. Weis, M. Akabori, K. Sladek, H. Hardtdegen, and Th. Schäpers. $LaLuO_3$ as a high-κ gate dielectric for InAs nanowire structures. *Semiconductor Science and Technology*, 25(8):085001, 2010.

[156] K. L. Ovanesyan, A. G. Petrosyan, G.O. Shirinyan, C. Pedrini, and L. Zhang. Single crystal growth and characterization of $LaLuO_3$. *Optical Materials*, 10(4):291 – 295, 1998.

[157] K. Ito, K. Tezuka, and Y. Hinatsu. Preparation, magnetic susceptibility, and specific heat on interlanthanide perovskites ABO_3 (A = La-Nd, B = Dy-Lu). *Journal of Solid State Chemistry*, 157(1):173–179, Feb 15 2001.

[158] T. Watahiki, F. Grosse, V. M. Kaganer, A. Proessdorf, and W. Braun. Growth and structural characterization of epitaxial $(La_{1-x}Lu_x)_2O_3$ layers grown on Si(111). *Journal of Vacuum Science & Technology B*, 28(3):C3A5–C3A8, 2010.

[159] M. Niehle and A. Trampert. Atomic interface structure of bixbyite rare-earth sesquioxides grown epitaxially on Si(111). *Journal of Physics D: Applied Physics*, 45(29):295302, 2012.

[160] Y. S. Cho, H. Hardtdegen, N. Kaluza, R. Steins, G. Heidelberger, and H. Lüth. The growth mechanism of GaN with different H_2/N_2 carrier gas ratios. *Journal of Crystal Growth*, 307(1):6 – 13, 2007.

[161] A. Schäfer, F. Wendt, S. Mantl, H. Hardtdegen, M. Mikulics, J. Schubert, M. Luysberg, A. Besmehn, G. Niu, and T. Schroeder. Hexagonal $LaLuO_3$ as high-κ dielectric. *Journal of Vacuum Science & Technology B*, 33(1):01A104, 2015.

[162] Y. Zhao, M. Toyama, K. Kita, K. Kyuno, and A. Toriumi. Moisture-absorption-induced permittivity deterioration and surface roughness enhancement of lanthanum oxide films on silicon. *Applied Physics Letters*, 88(7):132903, 2006.

[163] F. X. Zhang, M. Lang, J. W. Wang, U. Becker, and R. C. Ewing. Structural phase transitions of cubic Gd_2O_3 at high pressures. *Physical Review B*, 78:064114, Aug 2008.

[164] M. Zinkevich. Thermodynamics of rare earth sesquioxides. *Progress in Materials Science*, 52(4):597 – 647, 2007.

[165] Z. K. Heiba, Y. Akin, W. Sigmund, and Y. S. Hascicek. X-ray structure and microstructure determination of the mixed sesquioxides $(Eu_{1-x}Yb_x)_2O_3$ prepared by a sol-gel process. *Journal of Applied Crystallography*, 36(6):1411–1416, Dec 2003.

[166] Z. K. Heiba and L. Arda. X-ray diffraction analysis of powder and thin film of $(Gd_{1-x}Y_x)_2O_3$ prepared by sol-gel process. *Crystal Research and Technology*, 43(3):282–288, 2008.

[167] P. Aldebert and J. P. Traverse. Etude par diffraction neutronique des structures de haute temperature de La_2O_3 et Nd_2O_3. *Materials Research Bulletin*, 14(3):303–323, March 1979.

[168] M. G. Paton and E. N. Maslen. A refinement of the crystal structure of yttria. *Acta Crystallographica*, 19(3):307–310, Sep 1965.

[169] Hk. Müller-Buschbaum and H. G. V. Schnering. Zur Struktur der A-Form der Sesquioxide der Seltenen Erden. Strukturuntersuchungen an La_2O_3. *Zeitschrift für anorganische und allgemeine Chemie*, 340(5-6):232–245, 1965.

[170] J.M. Zuo and J.C. Mabon, Web-based Electron Microscopy Application Software: Web-EMAPS, Microsc Microanal 10 (Suppl 2), 2004; URL: http://emaps.mrl.uiuc.edu/.

[171] M. Mikulics, H. Hardtdegen, D. Gregušová, Z. Sofer, P. Šimek, St. Trellenkamp, D. Grützmacher, H. Lüth, P. Kordoš, and M. Marso. Non-uniform distribution of induced strain in a gate-recessed AlGaN/GaN structure evaluated by micro-PL measurements. *Semiconductor Science and Technology*, 27(10):105008, 2012.

[172] J.-L. Farvacque, Z. Bougrioua, and I. Moerman. Free-carrier mobility in GaN in the presence of dislocation walls. *Physical Review B*, 63:115202, Feb 2001.

[173] E. Bonera, G. Scarel, M. Fanciulli, P. Delugas, and V. Fiorentini. Dielectric Properties of High-κ Oxides: Theory and Experiment for Lu_2O_3. *Physical Review Letters*, 94:027602, Jan 2005.

[174] W. Koch and M. C. Holthausen. *A Chemist's Guide to Density Functional Theory.* Wiley-VCH Verlag GmbH, p. 1–64. 2001.

[175] R. M. Martin. *Electronic structure basic theory and practical methods [E-Book].* Cambridge University Press„ New York, Chapter 16. 2004.

[176] D. Sholl and J. A. Steckel. *Density functional theory: a practical introduction.* John Wiley & Sons, p. 11–12, 15. 2011.

[177] D. J. Singh and L. Nordstrom. Planewaves, pseudopotentials and the LAPW method. [E-Book], 2006.

[178] S. Blügel and G. Bihlmayer. Full-potential Linearized Augmented Planewave Method. published in Computational Nanoscience: Do it yourself! edited by J. Grotendorst, S. Blügel and D. Marx, NIC Series Vol. 31, p. 85-130 (John von Neumann Institute for Computing, Jülich), 2006.

[179] E. Wimmer, H. Krakauer, M. Weinert, and A. J. Freeman. Full-potential self-consistent linearized-augmented-plane-wave method for calculating the electronic structure of molecules and surfaces: O_2 molecule. *Physical Review B*, 24:864–875, Jul 1981.

[180] see www.flapw.de.

[181] J. Perdew and M. Levy. Physical Content of the Exact Kohn-Sham Orbital Energies: Band Gaps and Derivative Discontinuities. *Physical Review Letters*, 51:1884–1887, Nov 1983.

List of Publications

Journal Papers

- A. Schäfer, K. Rahmanizadeh, G. Bihlmayer, M. Luysberg, F. Wendt, A. Besmehn, A. Fox, M. Schnee, G. Niu, T. Schroeder, S. Mantl, H. Hardtdegen, M. Mikulics, and J. Schubert. Polymorphous $GdScO_3$ as high permittivity dielectric. *Journal of Alloys and Compounds, accepted for publication.*
- A. Schäfer, F. Wendt, S. Mantl, H. Hardtdegen, M. Mikulics, J. Schubert, M. Luysberg, A. Besmehn, G. Niu and T. Schroeder. Hexagonal $LaLuO_3$ as high-κ dielectric. *Journal of Vacuum Science & Technology B*, 33(1), 2015.
- A. Schäfer, A. Besmehn, M. Luysberg, A. Winden, T. Stoica, M. Schnee, W. Zander, G. Niu, T. Schroeder, S. Mantl, H. Hardtdegen, M. Mikulics and J. Schubert. Hexagonal $GdScO_3$: an epitaxial high-κ dielectric for GaN. *Semiconductor Science and Technology* 29 (7), 075005, 2014.
- L. Knoll, S. Richter, A. Nichau, S. Trellenkamp, A. Schäfer, K. K. Bourdelle, J. M. Hartmann, Q. T. Zhao and S. Mantl. Strained Si and SiGe tunnel-FETs and complementary tunnel-FET inverters with minimum gate lengths of 50 nm. *Solid-State Electronics* 97, 76-81, 2014.
- L. Knoll, S. Richter, A. Nichau, S. Trellenkamp, A. Schäfer, S. Wirths, S. Blaeser, D. Buca, K. K. Bourdelle, Q. T. Zhao and S. Mantl. Strained silicon based complementary tunnel-FETs: Steep slope switches for energy efficient electronics. *Solid-State Electronics* 98 (0), 32-37, 2014.
- S. Richter, S. Trellenkamp, A. Schäfer, J. M. Hartmann, K. K. Bourdelle, Q. T. Zhao, and S. Mantl. Improved Tunnel-FET Inverter Performance with SiGe/Si Heterostructure Nanowire TFETs by Reduction of Ambipolarity. *Solid-State Electronics* (accepted for publication), 2014.
- S. Richter, S. Blaeser, L. Knoll, S. Trellenkamp, A. Fox, A. Schäfer, J. M. Hartmann, Q. T. Zhao and S. Mantl. Silicon–germanium nanowire tunnel-FETs with homo- and heterostructure tunnel junctions. *Solid-State Electronics* 98 (0), 75-80, 2014.
- M. Schmidt, R. A. Minamisawa, S. Richter, A. Schäfer, D. M. Buca, J. M. Hartmann, Q.-T. Zhao and S. Mantl. Unipolar behavior of asymmetrically doped strained Si 0.5Ge 0.5 tunneling field-effect transistors. *Applied Physics Letters* 101 (12), 123501, 2012.

- L. Knoll, M. Schmidt, Q. T. Zhao, S. Trellenkamp, A. Schäfer, K. K. Bourdelle and S. Mantl .Si tunneling transistors with high on-currents and slopes of 50 mV/dec using segregation doped $NiSi_2$ tunnel junctions. *Solid-State Electronics* 84, 211-215, 2013.

- L. Knoll, Q. T. Zhao, A. Nichau, S. Trellenkamp, S. Richter, A. Schäfer, D. Esseni, L. Selmi, K. K. Bourdelle and S. Mantl. Inverters With Strained Si Nanowire Complementary Tunnel Field-Effect Transistors. *IEEE Electron Device Letters* 34 (6), 813-815, 2013.

- J. Lehmann, R. Hübner, J. V. Borany, W. Skorupa, T. Mikolajick, A. Schäfer, J. Schubert and S. Mantl. Millisecond flash lamp annealing for $LaLuO_3$ and $LaScO_3$ high-k dielectrics. *Microelectronic Engineering* 109, 381 - 384, 2013. DOI: 10.1016/j.mee.2013.04.021.

- A. Nichau, A. Schäfer, L. Knoll, S. Wirths, T. Schram, L. Å. Ragnarsson, J. Schubert, P. Bernardy, M. Luysberg, A. Besmehn, U. Breuer, D. Buca and S. Mantl. Reduction of silicon dioxide interfacial layer to 4.6 Å EOT by Al remote scavenging in high-κ/metal gate stacks on Si. *Microelectronic Engineering* 109, 109-112 (2013).

- M. Schmidt, R. A. Minamisawa, S. Richter, A. Schäfer, D. M. Buca, J. M. Hartmann, Q.-T. Zhao and S. Mantl. Unipolar behavior of asymmetrically doped strained Si 0.5Ge 0.5 tunneling field-effect transistors. *Applied Physics Letters* 101 1(2), 123501 2012.

Conference Contributions

- A. Schäfer, M. L., F. Wendt, G. Niu, T. Schroeder, S. Mantl, H. Hardtdegen, M. Mikulics, J. Schubert. (2014). Hexagonal $LaLuO_3$ as high-k dielectric. Talk at the *18th Workshop on Dielectrics in Microelectronics (WoDiM)* 2014, Cork, Ireland.

- A. Schäfer, A. Winden, H. Hardtdegen, M. Luysberg, T. Schroeder, J. Schubert. Structural and Electrical Characterization of hexagonal $GdScO_3$. Poster presentation at the *Semiconductor Interface Specialists Conference (SISC)* 2013, Arlington (USA).

- A. Nichau, A. Schäfer, L. Knoll, S. Wirths, T. Schram, L. A. Ragnarsson, J. Schubert, P. Bernardy, M. Luysberg, A. Besmehn, U. Breuer, D. M. Buca and S. Mantl (2013). Reduction of silicon dioxide interfacial layer to 4.6 Å EOT by Al remote scavenging in high-κ/metal gate stacks on Si. Talk at the *18th Conference on Insulating Films on Semiconductors (Infos)* 2013, Krakau (Poland).

- A. Schäfer, A. Winden, W. Zander, T. Schroeder, H. Hardtdegen and J. Schubert. Structural properties of epitaxial rare-earth based oxides on GaN and Y_2O_3. Poster

presentation at the *Materials Research Society Spring (MRS) Meeting and Exhibit* 2013, San Francisco (USA).

- A. Schäfer, A. Winden, W. Zander, G. Mussler, M. von der Ahe, H. Hardtdegen and J. Schubert. Structural and electrical properties of epitaxially grown $GdScO_3$ and $LaLuO_3$ on GaN. Poster presentation at the *Semiconductor Interface Specialists Conference (SISC)* 2012, San Diego (USA).

- A. Schäfer, A. Tiedemann, A. Nichau, R. Lupták, V. Mußmann, J. Schubert and S. Mantl, Using ALD and AVD-techniques for scaled gate stacks. Poster presentation at the *International Wilhelm & Else Heraeus Phyics School on "Microelectronics for Society - More Moore expands More then Moore"* 2012, Bad Honnef.

Acknowledgment

This work would not have been possible without the support from numerous people always willing to help. I would like to thank each one of them (even though I might have forgotten them in the following list).

I want to particularly thank Prof. Mantl for giving me the opportunity to be part of his research group, for his advices and fair discussions. I also thank Prof. Klemradt for evaluating my thesis as second promoter.

A huge thanks belongs to my supervisor Jürgen Schubert, a walking oxide library who passes by daily curious on the newest results and whose door is always open for assistance and discussion no matter what problem may appear.

I kindly thank Hilde Hardtdegen and Martin Mikulics for sharing their knowledge with me and supporting my work on GaN.

Also a big thanks goes do Dan Buca, Qing-Tai Zhao and Bernd Holländer for fruitful discussions and to the 'Waldschlösschen-Crew' Andreas Tiedemann, Patric Bernardy and Karl-Heinz Deussen for processing numerous samples with me and for me.

There is a long list of students (in no particular order) I would like to thank for introducing me to new machines, sharing their knowledge with me and just making my days more fun: Roman Luptak, Michael Schnee, Alexander Nichau, Volker Mussmann, Peter Romanczyk, Fabian Wendt, Xinli Chen, Thomas Tromm, Marián Pampillon, Markus Hagedorn, Lars Knoll, Simon Richter, Mathias Schmidt, Renato Minamisawa, Vinh Gia Luong, Stephan Wirths, Sebastian Bläser, Linjie Liu, Nils von den Driesch, Daniela Stange, Christian Schulte-Braucks, Qingua Han and Andreas Winden.

Thanks to all the staff around in the Forschungszentrum supporting my research such as Steffi Lenk, Willi Zander, Andre Dahmen, Christian Scholtysik, Katja Palmen, Martina von der Ahe, Gregor Mussler, Martina Luysberg, Alfred Fox, Brigitte Modolo, Silke Piper, Mirjam Seller, Toma Stoica, Mihai Stoica, Gustav Bihlmayer, Kourosh Rahmanizadeh, Astrid Besmehn, Uwe Breuer and the HNF clean room team.

I also appreciate the successful cooperation with Thomas Schroeder and Gang Niu at the IHP Frankfurt(Oder).

Last but not least I want to thank Gregor and my family for supporting me, encouraging me and trusting in me at any time.

Band / Volume 32
Electrical characterization of manganite and titanate heterostructures
A. Herpers (2014), ix, 165 pp
ISBN: 978-3-89336-948-5

Band / Volume 33
Oxygen transport in thin oxide films at high field strength
D. Weber (2014), XII, 115 pp
ISBN: 978-3-89336-950-8

Band / Volume 34
Structure, electronic properties, and interactions of defects in epitaxial GaN layers
P. H. Weidlich (2014), 139 pp
ISBN: 978-3-89336-951-5

Band / Volume 35
Defect Engineering of $SrTiO_3$ thin films for resistive switching applications
S. Wicklein (2014), xi, 144 pp
ISBN: 978-3-89336-963-8

Band / Volume 36
Integration and Characterization of Atomic Layer Deposited TiO_2 Thin Films for Resistive Switching Applications
M. Reiners (2014), xiv, 166 pp
ISBN: 978-3-89336-970-6

Band / Volume 37
Resistive switching in ZrO_2 based metal-oxide-metal structures
I. Kärkkänen (2014), xviii, 125 pp
ISBN: 978-3-89336-971-3

Band / Volume 38
Resistive switching phenomena of extended defects in Nb-doped $SrTiO_3$ under influence of external gradients
C. Rodenbücher (2014), xiii, 200 pp
ISBN: 978-3-89336-980-5

Band / Volume 39
Micro-spectroscopic investigation of valence change processes in resistive switching $SrTiO_3$ thin films
A. Köhl (2014), viii, 166 pp
ISBN: 978-3-89336-988-1

Schriften des Forschungszentrums Jülich
Reihe Information

Band / Volume 40
Strained Silicon and Silicon-Germanium Nanowire Tunnel FETs and Inverters
S. Richter (2014), iii, 117 pp
ISBN: 978-3-95806-002-9

Band / Volume 41
Integration of Redox-Based Resistive Switching Memory Devices
F. Lentz (2014), i, 166 pp
ISBN: 978-3-95806-019-7

Band / Volume 42
Ladungstransportuntersuchungen an nanofunktionalen Bauelementen mit Diodencharakteristik basierend auf funktionalisierten Nanopartikeln
N. Babajani (2015), iv, 138, XLVII
ISBN: 978-3-95806-026-5

Band / Volume 43
Transport and Noise Properties of Nanostructure Transistors for Biosensor Applications
J. Li (2015), vii, 175 pp
ISBN: 978-3-95806-034-0

Band / Volume 44
Quantitative scanning tunneling spectroscopy of non-polar III-V compound semiconductor surfaces
M. Schnedler (2015), 122 pp
ISBN: 978-3-95806-075-3

Band / Volume 45
Model-based Algorithm Development with Focus on Biosignal Processing
Y. Yao (2015), x, 169 pp
ISBN: 978-3-95806-080-7

Band / Volume 46
Growth and characterization of crystalline rare-earth based thin oxide films for the application as gate dielectric in nanotechnology
A. B. Schäfer (2015), xiii, 157 pp
ISBN: 978-3-95806-111-8

Weitere ***Schriften des Verlags im Forschungszentrum Jülich*** unter
http://wwwzb1.fz-juelich.de/verlagextern1/index.asp

Information

46

Growth and characterization of crystalline thin oxide fims

Anna Barbara Schäfer

Member of the Helmholtz Association

Information
Band / Volume 46
ISBN 978-3-95806-111-8

JÜLICH
FORSCHUNGSZENTRUM

Growth and characterization of crystalline rare-earth based thin oxide films for the application as gate dielectric in nanotechnology

Anna Barbara Schäfer

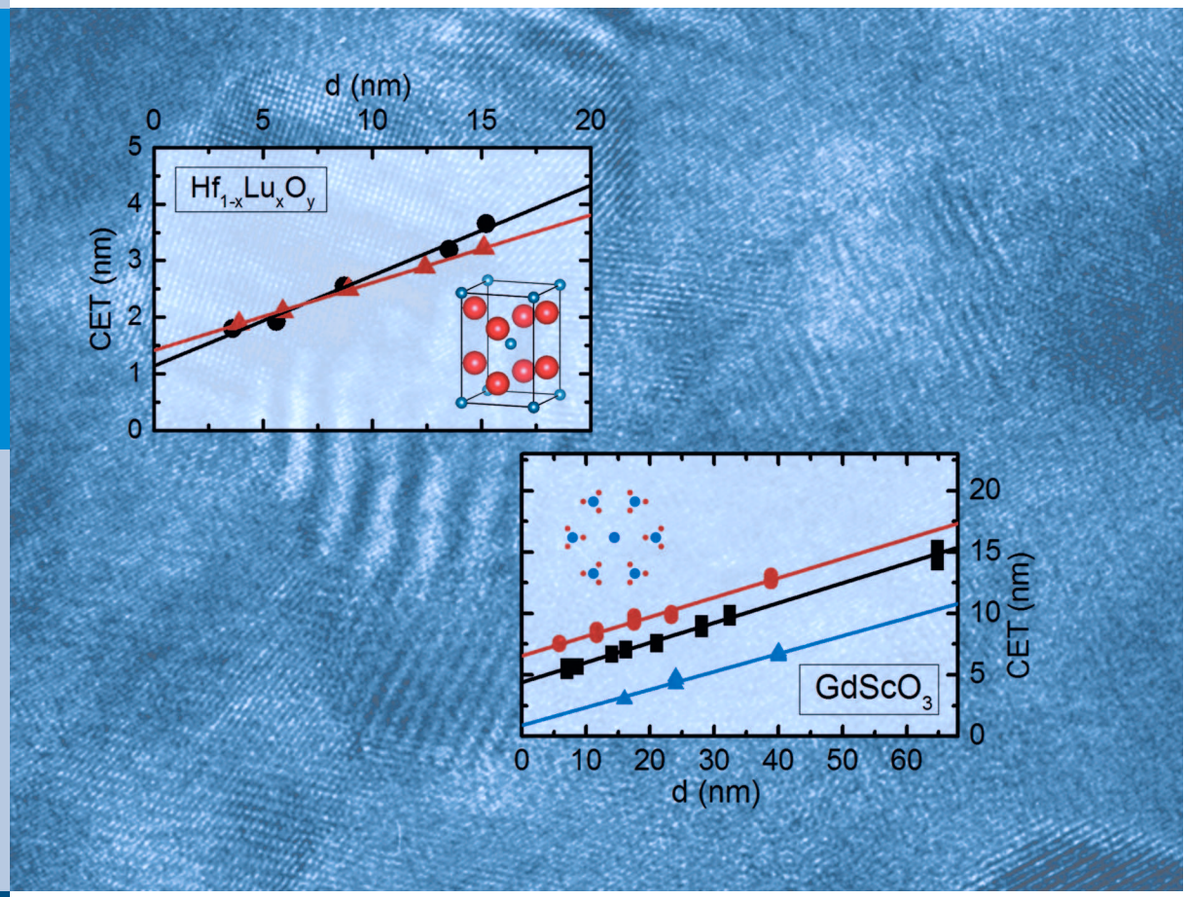

Information
Band / Volume 46
ISBN 978-3-95806-111-8

JÜLICH
FORSCHUNGSZENTRUM